Does Human Transthyretin Aggregate in Blood Plasma or in Cardiac Tissue? A Mathematical Modeling Study

Andrey V. Kuznetsov

Department of Mechanical and Aerospace Engineering, North Carolina State University,

Raleigh, NC 27695-7910, USA; e-mail: avkuznet@ncsu.edu

Abstract

Transthyretin (TTR) amyloidosis is a progressive disease characterized by the destabilization of TTR tetramers, leading to monomer dissociation, oligomer formation, and fibril deposition in cardiac tissue. This study presents a mathematical model that captures the kinetics of TTR aggregation and deposition, integrating clinically relevant parameters to distinguish between scenarios of TTR aggregation in blood plasma and cardiac tissue. The governing equations are derived by applying conservation principles to the number of TTR tetramers, monomers, and oligomers within defined control volumes, such as the blood plasma or heart. The model predicts that the scenario with fibril accumulation within cardiac tissue better reflects the clinical progression of wild-type TTR amyloidosis, aligning with observed patient survival times and measured tetramer concentrations. The simulations reproduce known physiological values, including a tetramer concentration of ~4.5 μM, consistent with published physiological data. Sensitivity analyses reveal that the rate of tetramer dissociation and the half-deposition time of TTR oligomers are key regulators of disease progression. Lower tetramer dissociation rates, mimicking the stabilizing effect of tafamidis, reduce fibril accumulation and biological aging. Conversely, faster oligomer deposition into fibrils leads to reduced oligomer concentrations but accelerated tissue fibril accumulation. The model predicts that, after five years of disease progression, the fraction of heart volume occupied by TTR fibrils may reach 58% in the tissue aggregation scenario, compared to 10% when aggregation occurs in plasma. These predictions are consistent with clinical observations that link higher amyloid burden to increased mortality. Overall, the findings support a pathogenic mechanism in which TTR aggregation predominantly occurs in cardiac tissue, highlighting potential therapeutic targets to modulate disease progression. A correlation is proposed for estimating biological age in humans, which incorporates both calendar age and the fraction of heart volume occupied by TTR amyloid fibrils.

Keywords: biomarker of aging; Finke−Watzky model; cardiac biomarkers; biological aging

Abbreviations

ATTR transthyretin amyloidosis

F-W Finke-Watzky

IDP intrinsically disordered protein

TTR transthyretin

1. Introduction

Transthyretin (TTR) is a transport protein primarily produced in the liver that carries the hormone thyroxine and vitamin A (retinol) in the bloodstream, both of which are otherwise insoluble under normal conditions (Kittleson et al., 2020), (Gao et al., 2022). However, TTR is also an amyloidogenic protein capable of forming insoluble deposits in various tissues—most notably in the heart—leading to the formation of amyloid fibrils. The pathological accumulation of transthyretin amyloid within the cardiac muscle increases myocardial stiffness, which progressively impairs the heart's ability to pump effectively and ultimately results in congestive heart failure (Ruberg et al., 2019), (Smiley et al., 2022). These deposits contribute to progressive diastolic and systolic dysfunction, ultimately resulting in congestive heart failure and, if left untreated, death. This condition is known as cardiac amyloidosis (Ruberg and Berk, 2012).

(Criddle et al., 2024) proposed two competing hypotheses for how insoluble amyloid fibrils composed of TTR appear in tissue. In the first, TTR monomers misfold and aggregate into protofibrils in the bloodstream, which then circulate and deposit in specific tissues; in the second, TTR monomers circulate until they bind directly to tissue sites, where they form amyloid deposits *in situ*.

One of the objectives of this paper is to investigate how the accumulation of TTR fibrils in the heart relates to biological age. Aging is characterized by the gradual accumulation of harmful changes at molecular, cellular, tissue, and organ levels, collectively referred to as "damage." While the body has repair mechanisms that counteract some of these changes, their effectiveness declines over time. It is important to note, however, that not all age-related alterations are detrimental—some may be adaptive, and others may have a neutral impact on health and function (Gladyshev et al., 2021).

Because aging involves a complex interplay of many interrelated biological processes, calendar age does not always accurately reflect an individual's physiological condition. To capture this complexity, researchers have developed various computational tools known as aging clocks, which estimate biological age based on biomarkers that reflect different aspects of the aging process (Min et al., 2024). The diversity of these clocks emphasizes the multifaceted nature of aging, as no single biomarker can capture it fully. Existing models target different biological mechanisms, including epigenetic clocks that track DNA methylation changes, telomere-based clocks that monitor telomere shortening, and epitranscriptomic clocks that measure alterations in RNA methylation (Wang et al., 2023), (Han, 2024), (Crimmins et al., 2024). Each provides a distinct perspective on the biological underpinnings of aging.

Recently, (Dormann and Lemke, 2024) introduced the concept of an aging clock centered on the aggregation of intrinsically disordered proteins (IDPs)—such as amyloid beta (Aβ), tau, α-synuclein, and TDP-43. Unlike structured proteins, IDPs lack a stable folded conformation, making them prone to aggregate, as their aggregated forms are thermodynamically more favorable than their native disordered states (Vetri and Foderà, 2015). The appeal of an IDP-based aging clock stems from the fact that protein aggregation is intimately linked to aging and serves as a hallmark of neurodegenerative diseases like Alzheimer's and Parkinson's, for which advanced age remains the greatest risk factor. Building on this idea, (Kuznetsov, 2025a) proposed tracking the cumulative neurotoxicity of Aβ oligomers as a potential biomarker for the biological age of neural cells.

The accumulation of misfolded, aggregation-prone proteins is a systemic phenomenon, not confined to the brain. For example, although TTR is not an inherently disordered protein, it can aggregate when its native structure becomes destabilized. This paper introduces a new biomarker defined as the fraction of the heart's volume occupied by TTR amyloid fibrils, $\frac{V_{fibrils}}{V_{heart}}$. This biomarker captures the time-dependent progression of TTR fibril deposition in cardiac tissue and its effect on biological age.

2. Materials and models

2.1. Governing equations

2.1.1. Conservation of TTR tetramers in the blood plasma

TTR tetramers are stable and are not prone to aggregation. It is well established that the dissociation of TTR tetramers into monomers is the initial step in TTR fibril formation (Almeida et al., 2024). Furthermore, due to the high stability of TTR tetramers (Sanguinetti et al., 2022), their dissociation into monomers represents the rate-limiting step in amyloid fibril formation (Esperante et al., 2021), (Rinauro et al., 2024). Tetramer dissociation appears to be irreversible, as reported in (Quintas et al., 1999).

The mathematical framework is based on mass balance equations that govern the dynamics of tetramers, monomers, free oligomers, and oligomers incorporated into TTR amyloid fibrils. The model uses the lumped capacitance approach, assuming a uniform spatial distribution of all TTR species in both blood plasma and cardiac tissue, with time (t) as the only independent variable. In this framework, time is interchangeable with calendar age. Table 1 defines the dependent variables, while Table 2 provides a summary of the model parameters.

The dissociation of TTR occurs in blood plasma and is described by the following equation:

$$T \xrightarrow{k_M} 4M \tag{1}$$

Expressing the conservation of TTR tetramers in blood plasma and dividing both sides of the equation by V_{plasma} yields the following equation:

$$\frac{d[T]}{dt} = \frac{q_T m_{liver}}{MW_{tet} V_{plasma}} b_{21} - k_M [T] - [T] \frac{\ln(2)}{T_{1/2,T}} \tag{2}$$

where q_T denotes the rate of TTR tetramer production per unit mass of liver tissue. In Eq. (2), the first term on the right-hand side represents tetramer production in the liver; the second term accounts for the reduction in tetramer concentration due to their conversion into monomers; and the third term reflects the decline in tetramer concentration resulting from their limited half-life.

Eq. (2) must be solved with the following boundary condition:

$$\text{At } t = 0: \qquad [T] = [T]_0 \tag{3}$$

As noted in footnote "o" of Table 2, the effect of the initial condition becomes negligible when the duration of TTR aggregation is sufficiently long, allowing $[T]_0$ to be set to zero.

Under steady-state conditions, the solution of Eq. (2) is:

$$[T]_{plasma} = \frac{q_T m_{liver} b_{21}}{MW_{tet} V_{plasma} \left(k_M + \frac{\ln(2)}{T_{1/2,T}} \right)} \tag{4}$$

Eq. (4) can be used to estimate the value of q_T if $[T]_{plasma}$ is known:

$$q_T = \frac{[T]_{plasma} MW_{tet} V_{plasma} \left(k_M + \frac{\ln(2)}{T_{1/2,T}} \right)}{m_{liver} b_{21}} \tag{5}$$

Other equations in the model rely on assumptions about where TTR monomer aggregation takes place. Two scenarios are considered: (1) TTR monomers aggregate in the blood plasma, and the resulting protofibrils then deposit in cardiac tissue, where they are uniformly distributed by diffusion; (2) TTR monomers first deposit in cardiac tissue, where aggregation subsequently occurs. These scenarios are consistent with those explored in (Criddle et al., 2024), who employed a different model that did not

include autocatalysis. Similarly, (Criddle et al., 2020) also did not incorporate autocatalysis in their simulations.

Other equations in the model depend on the assumption regarding where TTR monomers aggregate. Two scenarios are considered: (1) TTR monomers aggregate in the blood plasma, and the resulting protofibrils deposit in cardiac tissue, where they are uniformly distributed by diffusion (Fig. 1a); (2) TTR monomers first deposit in cardiac tissue, where they subsequently aggregate (Fig. 1b).

2.1.2. Conservation equations for the scenario when amyloid fibrils form in blood plasma

In many protein misfolding diseases, the aggregation of misfolded proteins is described by two key mechanisms: primary nucleation and secondary nucleation. Secondary nucleation is an autocatalytic process in which new aggregates form when monomers bind to and nucleate on the surface of existing fibrils (Rinauro et al., 2024).

After TTR tetramers dissociate into monomers—which are prone to aggregation—the monomers assemble into oligomers and subsequently form amyloid fibrils (Gao et al., 2022), (Criddle et al., 2020). Aggregation of TTR monomers into oligomers is simulated using the Finke-Watzky (F-W) model. The F-W model is a minimal two-step model that describes parallel nucleation and autocatalytic growth (Morris et al., 2008), (Iashchishyn et al., 2017), (Finke et al., 2020). It has been effectively used to model the aggregation of various neurological proteins (Morris et al., 2008). When the two-step model is applied to simulate the formation of amyloid aggregates (Rinauro et al., 2024), the first pseudoelementary step describes the nucleation process of TTR oligomers:

$$M \xrightarrow{k_1} B \tag{6}$$

It is worth noting that, as a minimal model, the F-W model does not differentiate between the size (and mass) of a monomer and an oligomer. An oligomer is simply regarded as an activated monomer that is capable of autocatalysis. Once TTR oligomers (phase *B*) are formed, they are assumed to autocatalyze their own production from monomers in a prion-like manner—an autocatalytic process similar to that observed in several other amyloid disorders (Criddle et al., 2020). The potential involvement of a seed-dependent mechanism in TTR cardiac amyloidosis has been reviewed in (Morfino et al., 2022). Accordingly, and in line with the F-W model, the second pseudo-elementary step represents the autocatalytic conversion of monomers into TTR oligomers and is described as follows:

$$M + B \xrightarrow{k_2} 2B \tag{7}$$

By formulating the conservation of TTR monomers in the blood plasma and normalizing the equation by V_{plasma}, the following equation is obtained:

$$\frac{d[M]_{plasma}}{dt} = 4k_M [T]_{plasma} - k_1 [M]_{plasma} - k_2 [M]_{plasma} [B]_{plasma} - [M]_{plasma} \frac{\ln(2)}{T_{1/2,M,plasma}} \quad (8)$$

where $[T]_{plasma}$ is a constant value given by Eq. (4). The first term on the right-hand side represents the production of TTR monomers through the dissociation of tetramers. The second and third terms account for the reduction in monomer concentration due to their conversion into oligomers via nucleation and autocatalytic processes, respectively. The fourth term captures the decline in monomer concentration due to their limited half-life. Accordingly, the model assumes that TTR monomers are cleared from the plasma either by aggregation into oligomers or through proteolytic degradation, consistent with (Criddle et al., 2020).

The conversion of free TTR oligomers into protofibrils is modeled analogously to coagulation processes occurring in colloidal suspensions (Boltachev and Ivanov, 2020). In this approach, free TTR oligomers (B) are characterized by a half-deposition time $\theta_{1/2,B}$, reflecting the time required for half of the oligomer population to incorporate into protofibrils. By expressing the concentration of free TTR oligomers in the plasma and dividing it by V_{plasma}, the following equation is obtained:

$$\frac{d[B]_{plasma}}{dt} = k_1 [M]_{plasma} + k_2 [M]_{plasma} [B]_{plasma} - [B]_{plasma} \frac{\ln(2)}{T_{1/2,B}} - [B]_{plasma} \frac{\ln(2)}{\theta_{1/2,B}} \quad (9)$$

where the first and second terms on the right-hand side represent the formation of free TTR oligomers from monomers via nucleation and autocatalytic processes, respectively. The third term accounts for the decrease in free oligomer concentration due to their limited half-life, while the fourth term reflects their loss through deposition into protofibrils.

The conservation of TTR oligomers deposited into protofibrils circulating in the bloodstream, when normalized by V_{plasma}, yields the following equation:

$$\frac{d[I]_{plasma}}{dt} = [B]_{plasma} \frac{\ln(2)}{\theta_{1/2,B}} - [I]_{plasma} \frac{\ln(2)}{T_{1/2,I}} - [I]_{plasma} \frac{\ln(2)}{\theta_{1/2,I}} \quad (10)$$

where the first term on the right-hand side represents the increase in the concentration of oligomers deposited into protofibrils as free oligomers incorporated into these protofibrils. The second term

accounts for the reduction in protofibril concentration in the bloodstream due to their limited half-life, while the third term represents the decrease in their concentration due to capture by cardiac tissue.

In the proposed scenario, protofibrils originate in the bloodstream, travel through circulation, and deposit in specific tissues with compatible binding sites. To enable this process, circulating protofibrils must strike a balance: they must be sufficiently small to move freely within the vasculature, yet large enough to expose a recognizable pattern of amino acid side chains that facilitate selective tissue adhesion. TTR protofibrils composed of approximately 10 to 50 monomer units appear to fulfill both of these criteria (Criddle et al., 2024).

In this scenario, the total concentration of TTR present in the blood plasma (a quantity more easily accessible to experiments than concentrations of particular TTR species) can be expressed as:

$$[TTR]_{total} = [T]_{plasma} + [M]_{plasma} + [B]_{plasma} + [I]_{plasma} \tag{11}$$

Stating the conservation of TTR oligomers deposited into fibrils that infiltrated the cardiac tissue, upon normalization by V_{heart}, leads to the following equation:

$$\frac{d[I]_{tissue}}{dt} = [I]_{plasma} \frac{\ln(2)}{\theta_{1/2,I}} - [I]_{tissue} \frac{\ln(2)}{T_{1/2,I}} \tag{12}$$

where the first term on the right-hand side models the increase in the concentration of TTR fibrils in cardiac tissue due to the capture of circulating protofibrils and their infiltration into the cardiac tissue. The second term accounts for a potential decrease in concentration of deposited fibrils resulting from their degradation. It is important to note that this degradation term reflects the anticipated effects of future therapeutic interventions—such as monoclonal antibody treatments—since current therapies are unable to remove pre-existing amyloid deposits from the heart (Emdin et al., 2023).

Eqs. (2), (8)–(10), and (12) are solved using initial condition (3) along with the following additional initial conditions:

$$\text{At } t = 0: \qquad [M]_{plasma} = 0, \quad [B]_{plasma} = 0, \quad [I]_{plasma} = 0, \quad [I]_{tissue} = 0 \tag{13a,b,c,d}$$

The numerical solution methodology is detailed in Section S1 of Supplementary Materials.

2.1.3. Approximate analytical solution for the scenario in which amyloid fibrils form in blood plasma

Approximate solutions are derived for the case in which all half-lives are assumed to be infinitely long, while half-deposition times remain finite.

Assuming that $T_{1/2,M,plasma} \to \infty$ and considering the steady-state conditions, Eq. (8) can be rewritten as:

$$0 = 4k_M [T]_{plasma} - k_1 [M]_{plasma} - k_2 [M]_{plasma} [B]_{plasma} \tag{14}$$

Assuming that $T_{1/2,B} \to \infty$, Eq. (9) can be rewritten as:

$$\frac{d[B]_{plasma}}{dt} = k_1 [M]_{plasma} + k_2 [M]_{plasma} [B]_{plasma} - [B]_{plasma} \frac{\ln(2)}{\theta_{1/2,B}} \tag{15}$$

By adding Eqs. (14) and (15), the following is obtained:

$$\frac{d[B]_{plasma}}{dt} = 4k_M [T]_{plasma} - [B]_{plasma} \frac{\ln(2)}{\theta_{1/2,B}} \tag{16}$$

Solving Eq. (16) subject to boundary condition (13b) yields:

$$[B]_{plasma} = 4k_M [T]_{plasma} \frac{\theta_{1/2,B}}{\ln(2)} \left(1 - \exp\left(-\frac{\ln(2)}{\theta_{1/2,B}} t \right) \right) \tag{17}$$

By substituting Eq. (17) into Eq. (14) and assuming steady-state conditions ($t \to \infty$), the following approximate solution for $[M]_{plasma}$ is obtained:

$$[M]_{plasma} = \frac{4k_M [T]_{plasma}}{k_1 - 4k_2 k_M [T]_{plasma} \frac{\theta_{1/2,B}}{\ln(2)}} \tag{18}$$

Assuming that $T_{1/2,I} \to \infty$, Eq. (10) can be rewritten as:

$$\frac{d[I]_{plasma}}{dt} = [B]_{plasma} \frac{\ln(2)}{\theta_{1/2,B}} - [I]_{plasma} \frac{\ln(2)}{\theta_{1/2,I}} \tag{19}$$

By substituting Eq. (17) for $[B]_{plasma}(t)$ and solving Eq. (18) with initial condition (13c), the following is obtained:

$$[I]_{plasma} = \frac{4k_M [T]_{blood} \theta_{1/2,I}}{\ln(2)} \frac{1}{(\theta_{1/2,I} - \theta_{1/2,B})} \left[-\left(1 - \exp\left(-\frac{\ln(2)}{\theta_{1/2,B}} t \right) \right) \theta_{1/2,B} + \left(1 - \exp\left(-\frac{\ln(2)}{\theta_{1/2,I}} t \right) \right) \theta_{1/2,I} \right]$$

(20)

Note that

$$\lim_{\theta_{1/2,I}\to\theta_{1/2,B}}\left\{\frac{1}{\left(\theta_{1/2,I}-\theta_{1/2,B}\right)}\left[-\left(1-\exp\left(-\frac{\ln(2)}{\theta_{1/2,B}}t\right)\right)\theta_{1/2,B}+\left(1-\exp\left(-\frac{\ln(2)}{\theta_{1/2,I}}t\right)\right)\theta_{1/2,I}\right]\right\}$$
$$=1-\exp\left(-\frac{\ln(2)}{\theta_{1/2,B}}t\right)\left(1+\frac{\ln(2)}{\theta_{1/2,B}}t\right) \tag{21}$$

This implies that for $\theta_{1/2,I}\to\theta_{1/2,B}$, Eq. (20) simplifies to:

$$[I]_{plasma}=\frac{4k_M[T]_{plasma}\theta_{1/2,B}}{\ln(2)}\left[1-\exp\left(-\frac{\ln(2)}{\theta_{1/2,B}}t\right)\left(1+\frac{\ln(2)}{\theta_{1/2,B}}t\right)\right] \tag{22}$$

For $T_{1/2,I}\to\infty$ Eq. (12) simplifies to the following form:

$$\frac{d[I]_{tissue}}{dt}=[I]_{plasma}\frac{\ln(2)}{\theta_{1/2,I}} \tag{23}$$

Substituting Eq. (22) for $[I]_{plasma}(t)$ into Eq. (23) and solving it with the initial condition (13d) yields the following result:

$$[I]_{tissue}=\frac{4k_M[T]_{blood}}{\left(\theta_{1/2,B}-\theta_{1/2,I}\right)\ln(2)}$$
$$\times\left(-\left(1-\exp\left(-\frac{\ln(2)}{\theta_{1/2,B}}t\right)\right)\left(\theta_{1/2,B}\right)^2+t\theta_{1/2,B}\ln(2)+\theta_{1/2,I}\left[\theta_{1/2,I}-\exp\left(-\frac{\ln(2)}{\theta_{1/2,I}}t\right)\theta_{1/2,I}-t\ln(2)\right]\right) \tag{24}$$

It is worth noting that:

$$\lim_{\theta_{1/2,I}\to\theta_{1/2,B}}\frac{1}{\theta_{1/2,B}-\theta_{1/2,I}}\left(-\left(1-\exp\left(-\frac{\ln(2)}{\theta_{1/2,B}}t\right)\right)\left(\theta_{1/2,B}\right)^2+t\theta_{1/2,B}\ln(2)+\theta_{1/2,I}\left[\theta_{1/2,I}-\exp\left(-\frac{\ln(2)}{\theta_{1/2,I}}t\right)\theta_{1/2,I}-t\ln(2)\right]\right)$$
$$=-2\theta_{1/2,B}+t\ln(2)+\exp\left(-\frac{\ln(2)}{\theta_{1/2,B}}t\right)\left(2\theta_{1/2,B}+t\ln(2)\right) \tag{25}$$

Thus for $\theta_{1/2,I}\to\theta_{1/2,B}$, Eq. (24) reduces to the following simplified form:

$$[I]_{tissue} = \frac{4k_M [T]_{plasma}}{\ln(2)} \left[-2\theta_{1/2,B} + t\ln(2) + \exp\left(-\frac{\ln(2)}{\theta_{1/2,B}} t \right) \left(2\theta_{1/2,B} + t\ln(2) \right) \right] \tag{26}$$

For large values of t

$$1 - \exp\left(-\frac{\ln(2)}{\theta_{1/2,B}} t \right) \to 0 \text{ and } 1 - \exp\left(-\frac{\ln(2)}{\theta_{1/2,I}} t \right) \to 0 \tag{27a,b}$$

Thus, for large t, Eq. (24) approaches the following asymptotic form:

$$[I]_{tissue} \approx 4k_M [T]_{plasma} t \tag{28}$$

2.1.4. Conservation equations for the scenario when amyloid fibrils form in cardiac muscle tissue

The second scenario is supported by a review of (Williams et al., 2022), who stated that TTR monomers can be taken up by myocardial tissue, where they aggregate and form amyloid fibrils.

Stating the conservation of TTR monomer in the blood plasma and dividing both sides of the equation by V_{plasma}, yields the following equation:

$$\frac{d[M]_{plasma}}{dt} = 4k_M [T]_{plasma} - h_A \frac{S_{heart}}{V_{plasma}} \left([M]_{plasma} - [M]_{tissue} \right) - [M]_{plasma} \frac{\ln(2)}{T_{1/2,M,plasma}} \tag{29}$$

The total concentration of TTR in the blood plasma (a quantity more easily accessible to experiments) under this scenario is given by:

$$[TTR]_{total} = [T]_{plasma} + [M]_{plasma} \tag{30}$$

By applying the principle of conservation of TTR monomers in cardiac tissue and normalizing both sides of the equation by V_{heart}, the resulting equation is

$$\frac{d[M]_{tissue}}{dt} = h_M \frac{S_{heart}}{V_{heart}} \left([M]_{plasma} - [M]_{tissue} \right) - k_1 [M]_{tissue} - k_2 [M]_{tissue} [B]_{tissue} - [M]_{tissue} \frac{\ln(2)}{T_{1/2,M,tissue}} \tag{31}$$

The first term on the right-hand side represents the volumetric rate of TTR monomer deposition into cardiac tissue, where $h_M S_{heart} \left([M]_{plasma} - [M]_{tissue} \right)$ characterizes the total rate of monomer deposition into the entire heart. The second and third terms represent the loss of monomers as they are transformed

into oligomers through nucleation and autocatalytic mechanisms, respectively. The fourth term reflects monomer clearance resulting from their finite half-life.

Applying the conservation principle for TTR oligomers in cardiac tissue and scaling the equation by V_{heart} yields the following equation:

$$\frac{d[B]_{tissue}}{dt} = k_1[M]_{tissue} + k_2[M]_{tissue}[B]_{tissue} - [B]_{tissue}\frac{\ln(2)}{T_{1/2,B}} - [B]_{tissue}\frac{\ln(2)}{\theta_{1/2,B}} \tag{32}$$

where the first and second terms on the right-hand side describe the generation of free TTR oligomers from monomers through nucleation and autocatalytic pathways, respectively. The third term represents the clearance of oligomers due to their finite lifespan, and the fourth captures their removal through incorporation into TTR fibrils.

Applying the conservation principle to TTR oligomers incorporated into fibrils and normalizing by V_{heart} yields the following equation:

$$\frac{d[I]_{tissue}}{dt} = [B]_{tissue}\frac{\ln(2)}{\theta_{1/2,B}} - [I]_{tissue}\frac{\ln(2)}{T_{1/2,I}} \tag{33}$$

It should be noted that TTR fibrils are highly stable once deposited in cardiac tissue, and currently, heart transplantation is the only available treatment for patients with extensive fibril infiltration (Concetta Di Nora et al., 2022). Accordingly, the last term on the right-hand side of Eq. (33) is included solely to represent the potential impact of future therapies that may enable the clearance of TTR fibrils from the affected heart.

The system of Eqs. (29), (31)–(33) is solved subject to the initial conditions specified below:

At $t = 0$: $\quad [M]_{plasma} = 0, \quad [M]_{tissue} = 0, \quad [B]_{tissue} = 0, \quad [I]_{tissue} = 0$ (34a,b,c,d)

Table 1. Summary of dependent variables in the model.

Symbol	Definition	Unit
$[B]_{plasma}$	Molar concentration of free TTR oligomers in the blood plasma	μM

$[B]_{tissue}$	Molar concentration of free TTR oligomers in the cardiac tissue	μM
$[I]_{plasma}$	Molar concentration of TTR oligomers deposited into amyloid protofibrils circulating in the blood plasma	μM
$[I]_{tissue}$	Molar concentration of TTR oligomers deposited into amyloid fibrils that infiltrated the cardiac tissue	μM
$[M]_{plasma}$	Molar concentration of TTR monomers in the blood plasma	μM
$[M]_{tissue}$	Molar concentration of TTR monomers in the cardiac tissue	μM
$[T]$	Molar concentration of TTR tetramers, representing the native form of TTR, in the blood plasma	μM
$[TTR]_{total}$	Total concentration of TTR (in any state) in the blood plasma	μM

Table 2. Summary of model parameters along with their estimated values.

Symbol	Definition	Unit	Value or range	Reference or estimation method	Value(s) used in computations
a_{21}	Factor that converts from $\frac{\text{mol}}{\mu\text{m}^3}$ to μM	$\frac{\mu\text{M}\ \mu\text{m}^3}{\text{mol}}$	10^{21}		10^{21}
b_{21}	Conversion factor from $\frac{\text{mg}}{\text{min}}\frac{\text{mol}}{\text{g m}^3}$ to $\frac{\mu\text{M}}{\text{s}}$	$\frac{\mu\text{M}}{\text{s}}\frac{\text{min}}{\text{mg}}\frac{\text{g m}^3}{\text{mol}}$	0.0167		0.0167

h_M	Mass transfer coefficient characterizing the rate of deposition of TTR monomers into the endocardium	m s^{-1}			10^{-5} , 10^{-6} , 10^{-7} [a]
k_1	Kinetic rate constant characterizing the first pseudoelementary step in the F-W model that describes the nucleation of TTR oligomers	s^{-1}			10^{-4} , 10^{-6} , 10^{-8} [b]
k_2	Kinetic rate constant characterizing the second pseudoelementary step of the F-W model that describes the autocatalytic growth of TTR oligomers	μM^{-1} s^{-1}			10^{-4} , 10^{-6} , 10^{-8} [c]
k_M	Rate constant describing the dissociation of TTR tetramers into monomers	s^{-1}	4.14×10^{-6}	(Nelson et al., 2021)	4.14×10^{-6}
m_{liver}	Average mass of the human liver	kg	1.561 [d]	(Molina and DiMaio, 2012)	1.561

MW_{tet}	Molecular weight of TTR tetramer	g mol^{-1}	5.5×10^4 [e]	(Sanguinetti et al., 2022)	5.5×10^4
MW_{mon}	Molecular weight of TTR monomer	g mol^{-1}	1.4×10^4	(Quintas et al., 1999), (Sanguinetti et al., 2022)	1.4×10^4
N_A	Avogadro's number	mol^{-1}	6.022×10^{23}		6.022×10^{23}
q_T	Rate of TTR tetramers production per unit mass of the liver	$\frac{\text{mg}}{\text{min kg}}$	0.232	Estimated using Eq. (5)	0.232
S_{heart}	Surface area of blood vessels in a human heart	m^2			10 [f]
t_{CA}	Typical age of onset of transthyretin cardiac amyloidosis	s	1.89×10^9 [g]	(Brunjes et al., 2016)	1.89×10^9
$t_{TTR,f}$	Survival time among patients with wild-type TTR amyloidosis	s	1.10×10^8 - 1.97×10^8 [h]	(Ruberg and Berk, 2012)	1.58×10^8 [i]
$T_{1/2,B}$	Half-life of TTR oligomers	s			10^{20} (to simulate $T_{1/2,B}\to\infty$) [j]
$T_{1/2,T}$	Half-life of TTR tetramers in blood plasma	s	8.64×10^4 - 1.73×10^5 [k]	(Coelho et al., 2016)	1.73×10^5
$T_{1/2,I}$	Half-life of TTR oligomers once they have been deposited into TTR fibrils	s			10^{20} (to simulate $T_{1/2,I}\to\infty$) [1]

$T_{1/2,M,plasma}$	Half-life of TTR monomers in the blood plasma	s			10^{20} (to simulate $T_{1/2,M,plasma} \to \infty$) [m]
$T_{1/2,M,tissue}$	Half-life of TTR monomers in the cardiac tissue	s			10^{20} (to simulate $T_{1/2,M,tissue} \to \infty$) [n]
$[T]_0$	Initial concentration of TTR tetramers in the blood plasma	μM			0 [o]
$[T]_{plasma}$	Transthyretin concentration in the blood plasma	μM	3-6	(Powers and Kelly, 2021), (Coelho et al., 2016)	4.5
V_{plasma}	Average plasma volume in the human body	m^3	0.003 [p]	(Sharma and Sharma, 2025)	0.003
V_{heart}	Volume of myocardium in a human heart	m^3	5.76×10^{-4} [q]	(Betts, 2013)	5.76×10^{-4}
$\theta_{1/2,B}$	Half-deposition time for free TTR oligomers to become incorporated into TTR fibrils	s			10^5, 10^7, 10^9 [r]
$\theta_{1/2,I}$	Half-deposition time for TTR-derived amyloid fibrils circulating in blood plasma to deposit into cardiac tissue	s			10^5, 10^7, 10^9 [s]

$\rho_{fibrils}$	Density of TTR fibrils	g/μm^3	1.35×10^{-12} [t]	(Cavicchi et al., 2018)	1.35×10^{-12}

[a] Using values of h_M outside this range results in either unrealistically low or excessively high values of $[M]_{plasma}$ (data not shown).

[b] Due to the absence of published kinetic parameters about TTR aggregation within the framework of the F-W model, three representative values—10^{-4}, 10^{-6}, 10^{-8} s^{-1}—were chosen for the nucleation rate constant, k_1. These values were informed by data reported in (Morris et al., 2008) for a range of protein systems, which are summarized in Table S1 of (Kuznetsov, 2025b).

[c] In the absence of experimentally determined kinetic rates for TTR monomer aggregation within the framework of the F-W model, three representative values—10^{-4}, 10^{-6}, 10^{-8} μM^{-1} s^{-1}—were chosen for the kinetic constant describing autocatalytic growth, k_2. These values were informed by data reported in (Morris et al., 2008) for a range of protein systems, which are summarized in Table S1 of (Kuznetsov, 2025b).

[d] Value for men.

[e] A mass of TTR tetramer is 55,000 daltons (Sanguinetti et al., 2022).

[f] In an adult human, the total surface area of all capillary networks is estimated to reach around 6,000 square meters (Li and Jain, 2009). The surface area of the alveoli in the human lungs is estimated to be approximately 100 square meters (Ananda Rao and Johncy, 2022). As the surface area of blood vessels in the human heart is likely smaller than that of the alveoli in the lungs, it is estimated to be approximately 10 square meters.

[g] 60 years (Brunjes et al., 2016).

[h] Survival in individuals with wild-type TTR amyloidosis typically ranges from 43 to 75 months (Ruberg and Berk, 2012).

[i] 5 years.

[j] In the absence of published data, TTR oligomers were assumed to have an infinite half-life.

[k] 24–48 h (Coelho et al., 2016).

[l] Current therapies are unable to remove pre-existing amyloid deposits from the heart (Emdin et al., 2023). Therefore, it is assumed that TTR oligomers do not degrade after their deposition into TTR fibril deposits.

[m] In the absence of published data, TTR monomers in blood plasma were assumed to have an infinite half-life.

[n] In the absence of published data, TTR monomers in cardiac tissue were assumed to have an infinite half-life.

[o] Because the model assumes continuous production of TTR tetramers, the influence of their initial concentration diminishes over time, becoming negligible in long-term simulations.

[p] Given that the average blood volume in the human body is 5 L, and plasma constitutes approximately 60% of this volume (Sharma and Sharma, 2025), the total plasma volume is estimated to be 3 L.

[q] The human heart is commonly compared in size to a clenched fist, with approximate dimensions of 12 cm in length, 8 cm in width, and 6 cm in thickness (Betts, 2013).

[r] Assumed range.

[s] Assumed range.

[t] A widely accepted average density for proteins, regardless of their specific type, is 1.35 g/cm³ (Cavicchi et al., 2018).

2.1.5. Approximate analytical solution for the scenario in which amyloid fibrils form in cardiac muscle tissue

Similar to Section 2.1.3, approximate solutions are obtained under the assumption that all half-lives are infinitely long, while half-deposition times remain finite.

Assuming that $T_{1/2,M,plasma} \to \infty$ and considering the steady-state conditions, Eq. (29) can be simplified as:

$$4k_M [T]_{plasma} V_{plasma} - h_A S_{heart} \left([M]_{plasma} - [M]_{tissue} \right) = 0 \tag{35}$$

Assuming $T_{1/2,M,tissue} \to \infty$ and applying steady-state conditions, Eq. (31) may be rewritten as:

$$h_M S_{heart} \left([M]_{plasma} - [M]_{tissue} \right) - k_1 [M]_{tissue} V_{heart} - k_2 [M]_{tissue} [B]_{tissue} V_{heart} = 0 \tag{36}$$

Combining Eqs. (35) and (36) yields the following equation:

$$4k_M\left[T\right]_{plasma}V_{plasma}-k_1\left[M\right]_{tissue}V_{heart}-k_2\left[M\right]_{tissue}\left[B\right]_{tissue}V_{heart}=0 \tag{37}$$

Dividing both sides of Eq. (37) by V_{heart}, the equation can be rewritten as:

$$4k_M\left[T\right]_{plasma}\frac{V_{plasma}}{V_{heart}}-k_1\left[M\right]_{tissue}-k_2\left[M\right]_{tissue}\left[B\right]_{tissue}=0 \tag{38}$$

Assuming $T_{1/2,B}\to\infty$, Eq. (32) can be rewritten as:

$$\frac{d\left[B\right]_{tissue}}{dt}=k_1\left[M\right]_{tissue}+k_2\left[M\right]_{tissue}\left[B\right]_{tissue}-\left[B\right]_{tissue}\frac{\ln\left(2\right)}{\theta_{1/2,B}} \tag{39}$$

Adding Eqs. (38) and (39) yields the following result:

$$\frac{d\left[B\right]_{tissue}}{dt}=4k_M\left[T\right]_{plasma}\frac{V_{plasma}}{V_{heart}}-\left[B\right]_{tissue}\frac{\ln\left(2\right)}{\theta_{1/2,B}} \tag{40}$$

Solving Eq. (40) subject to boundary condition (34c) yields:

$$\left[B\right]_{tissue}=4k_M\left[T\right]_{blood}\frac{V_{plasma}}{V_{heart}}\frac{\theta_{1/2,B}}{\ln\left(2\right)}\left(1-\exp\left(-\frac{\ln\left(2\right)}{\theta_{1/2,B}}t\right)\right) \tag{41}$$

Solving Eq. (38) for $\left[M\right]_{tissue}$, the following is obtained:

$$\left[M\right]_{tissue}=4k_M\left[T\right]_{plasma}\frac{V_{plasma}}{V_{heart}}\frac{1}{k_1+k_2\left[B\right]_{tissue}} \tag{42}$$

Rearranging Eq. (35) to solve $\left[M\right]_{plasma}$ yields the following equation:

$$\left[M\right]_{plasma}=4k_M\left[T\right]_{plasma}V_{plasma}\frac{1}{h_AS_{heart}}+\left[M\right]_{tissue} \tag{43}$$

Assuming $T_{1/2,I}\to\infty$, Eq. (33) can be rewritten as:

$$\frac{d\left[I\right]_{tissue}}{dt}=\left[B\right]_{tissue}\frac{\ln\left(2\right)}{\theta_{1/2,B}} \tag{44}$$

Substituting Eq. (41) for $\left[B\right]_{tissue}$ into Eq. (44) and solving it with initial condition (34d) yields the following result:

$$[I]_{tissue} = 4k_M [T]_{plasma} \frac{V_{plasma}}{V_{heart}} \left(\left(-1 + \exp\left(-\frac{\ln(2)}{\theta_{1/2,B}} t \right) \right) \frac{\theta_{1/2,B}}{\ln(2)} + t \right) \tag{45}$$

For large values of t

$$1 - \exp\left(-\frac{\ln(2)}{\theta_{1/2,B}} t \right) \to 0 \tag{46}$$

At large values of t, Eq. (45) converges to the following asymptotic expression:

$$[I]_{tissue} \approx \frac{V_{plasma}}{V_{heart}} 4k_M [T]_{plasma} t \tag{47}$$

2.2. Calculating the volume occupied by TTR amyloid fibrils within the cardiac tissue

TTR amyloid fibrils are characterized by a twisted cross-β-helix structure (Miroy et al., 1996), (Steinebrei et al., 2023), (Dorbala Sharmila et al., 2020), (Schmidt et al., 2019).

The increase in the volume occupied by TTR amyloid fibril deposits in the cardiac tissue is determined by calculating the total number of TTR monomers incorporated into these fibril formations over a specified time t. In the F-W model, monomers are assumed to have the same molecular weight as oligomers (see Eq. (6)); this consideration enables the number of incorporated monomers to directly represent the volume of the deposits. Applying the approach adapted from (Watzky et al., 2008) yields the following expression:

$$N_{fibrils}(t) = \frac{[I]_{tissue}(t)}{a_{21}} V_{heart} N_A \tag{48}$$

Here, N_A denotes Avogadro's number.

Another way to calculate $N_{fibrils}(t)$ is by employing the following equation, as outlined in (Watzky et al., 2008):

$$N_{fibrils}(t) = \frac{V_{fibrils}(t) \rho_{fibrils}}{MW_{mon}} N_A \tag{49}$$

Here, MW_{mon} refers to the molecular weight of a TTR monomer, $V_{fibrils}(t)$ denotes the volume occupied by TTR amyloid fibril deposits in the heart at time *t*, and $\rho_{fibrils}$ specifies their density.

Equating the expressions on the right side of Eqs. (48) and (49) and solving for the fraction of heart volume occupied by TTR amyloid fibrils yields the following equation:

$$\frac{V_{fibrils}(t)}{V_{heart}} = \frac{[I]_{tissue}(t)}{a_{21}} \frac{MW_{mon}}{\rho_{fibrils}} \tag{50}$$

2.2.1. Volume occupied by TTR amyloid fibrils for the scenario when amyloid fibrils form in blood plasma

In the scenario where amyloid fibrils form in the blood plasma, $[I]_{tissue}$ is given by Eq. (24), which leads to:

$$\begin{aligned}\frac{V_{fibrils}(t)}{V_{heart}} &= \frac{MW_{mon}}{a_{21}\rho_{fibrils}} \frac{4k_M [T]_{blood}}{(\theta_{1/2,B} - \theta_{1/2,I})\ln(2)} \\ &\times \left(-\left(1 - \exp\left(-\frac{\ln(2)}{\theta_{1/2,B}} t\right)\right)(\theta_{1/2,B})^2 + t\theta_{1/2,B}\ln(2) + \theta_{1/2,I}\left[\theta_{1/2,I} - \exp\left(-\frac{\ln(2)}{\theta_{1/2,I}} t\right)\theta_{1/2,I} - t\ln(2)\right]\right)\end{aligned} \tag{51}$$

For the case where $\theta_{1/2,I} \to \theta_{1/2,B}$, Eq. (51) can be further simplified to:

$$\frac{V_{fibrils}(t)}{V_{heart}} = \frac{MW_{mon}}{a_{21}\rho_{fibrils}} \frac{4k_M [T]_{plasma}}{\ln(2)} \left[-2\theta_{1/2,B} + t\ln(2) + \exp\left(-\frac{\ln(2)}{\theta_{1/2,B}} t\right)(2\theta_{1/2,B} + t\ln(2)) \right] \tag{52}$$

For large *t*, the asymptotic limit of $[I]_{tissue}$ is given by Eq. (28), which leads to the following asymptotic form of Eq. (51):

$$\frac{V_{fibrils}(t)}{V_{heart}} = \frac{MW_{mon}}{a_{21}\rho_{fibrils}} 4k_M [T]_{blood}\, t \tag{53}$$

2.2.2. Volume occupied by TTR amyloid fibrils for the scenario when amyloid fibrils form in cardiac muscle tissue

In the scenario where amyloid fibrils form in cardiac muscle tissue, $[I]_{tissue}$ is given by Eq. (45), which leads to:

$$\frac{V_{fibrils}(t)}{V_{heart}} = \frac{MW_{mon}}{a_{21}\rho_{fibrils}} 4k_M [T]_{plasma} \frac{V_{plasma}}{V_{heart}} \left(\left(-1 + \exp\left(-\frac{\ln(2)}{\theta_{1/2,B}} t \right) \right) \frac{\theta_{1/2,B}}{\ln(2)} + t \right) \tag{54}$$

At large values of $[I]_{tissue}$, the asymptotic behavior of $[I]_{tissue}$ is described by Eq. (47), resulting in the following simplified form of Eq. (54):

$$\frac{V_{fibrils}(t)}{V_{heart}} = \frac{MW_{mon}}{a_{21}\rho_{fibrils}} \frac{V_{plasma}}{V_{heart}} 4k_M [T]_{plasma} t \tag{55}$$

It is important to note that the main distinction between Eqs. (53) and (55) is the inclusion of the factor $\frac{V_{plasma}}{V_{heart}}$ in Eq. (55). Using the parameter values listed in Table 2, this factor is estimated to be 5.21. This suggests that in scenario 2—where TTR monomers first deposit in the heart and aggregate locally within the cardiac tissue—the accumulation of TTR fibrils in the heart is approximately five times greater than in scenario 1, where amyloid fibrils form in the blood plasma and subsequently deposit into the cardiac tissue. This can be explained by the fact that in scenario 2, the concentration of TTR oligomers—which autocatalyze their formation from monomers—is higher than in scenario 1. This is due to the smaller volume of the heart compared to the volume of blood plasma, resulting in a higher local concentration of oligomers in scenario 2.

The biological age of the heart (referred to hereafter as biological age) is defined as follows:

$$\text{biological age} = \text{calendar age} + c\frac{V_{fibrils}(t_{CA})}{V_{heart}} = t_{CA} + t + c\frac{V_{fibrils}(t_{CA})}{V_{heart}} \tag{56}$$

Simulations for the scenario in which amyloid fibril formation occurs in cardiac muscle tissue, using the following parameter values: $h_M = 10^{-10}$ m s^{-1}, $k_1 = 10^{-6}$ s^{-1}, $k_2 = 10^{-6}$ μM^{-1} s^{-1}, $k_M = 4.14 \times 10^{-6}$ s^{-1}, $T_{1/2,T} = 1.73 \times 10^5$ s, $[T]_{blood} = 4.5$ μM, $\theta_{1/2,B} = 10^7$ s, $t_{TTR,f} = 1.58 \times 10^8$ s (5 years), along with values of other parameters given in Table 2, show that $\frac{V_{fibrils}(t)}{V_{heart}} = 0.577$. This result falls within the range reported by (Mehta et al., 2019), who classified patients into two groups based on their cardiac amyloidosis burden: moderate (0%–49%) and high (≥50%).

Assuming that TTR amyloidosis begins at age 60, progresses over 5 years, and that the patient's biological age reaches 100 by age 65, the following estimate for parameter c in Eq. (56) is obtained:

$$c = \frac{(100-60)-5}{0.577} \tag{57}$$

In the scenario where amyloid fibrils form in the blood plasma, the fraction of heart volume occupied by TTR fibrils at large t is given by Eq. (53), and the biological age approaches the following asymptotic expression:

$$\text{biological age} = t_{CA} + t + c\frac{MW_{mon}}{a_{21}\rho_{fibrils}} 4k_M [T]_{blood}\, t \tag{58}$$

In the scenario where amyloid fibrils develop within the cardiac muscle tissue, Eq. (55) describes the fraction of heart volume occupied by TTR fibrils as t becomes large, and the biological age tends toward the following asymptotic form:

$$\text{biological age} = t_{CA} + t + c\frac{V_{plasma}}{V_{heart}}\frac{MW_{mon}}{a_{21}\rho_{fibrils}} 4k_M [T]_{blood}\, t \tag{59}$$

2.3. Sensitivity of the heart volume fraction occupied by TTR amyloid fibrils to various parameters

The sensitivity of the heart volume fraction occupied by TTR amyloid fibrils with respect to key model parameters was analyzed by calculating local sensitivity coefficients. These coefficients represent the first-order partial derivatives of the output variable—the fraction of the heart volume occupied by TTR fibrils—with respect to various parameters, such as the dissociation rate constant of TTR tetramers into monomers, k_M. The methodology used follows established approaches described in (Beck and Arnold, 1977), (Zadeh and Montas, 2010), (Zi, 2011), (Kuznetsov and Kuznetsov, 2019). For instance, the sensitivity coefficient of the volume fraction with respect to k_M was computed using the following expression:

$$\frac{\partial\left(V_{fibrils}/V_{heart}\right)}{\partial k_M} \approx \left.\frac{V_{fibrils}\left(k_M+\Delta k_M\right)/V_{heart} - V_{fibrils}\left(k_M\right)/V_{heart}}{\Delta k_M}\right|_{\text{other parmeters kept constant}} \tag{60}$$

In this analysis, $\Delta k_M = 10^{-3} k_M$ represents the step size used for numerical differentiation. Multiple step sizes were tested to ensure that the computed sensitivity coefficients remained consistent and were not significantly affected by the choice of step size.

To facilitate comparison across parameters with different units and scales, dimensionless relative sensitivity coefficients were computed, following the approaches described in (Zadeh and Montas, 2010), (Kuznetsov and Kuznetsov, 2019). For example:

$$S_{k_M}^{V_{fibrils}/V_{heart}} = \frac{V_{fibrils} / V_{heart}}{k_M} \frac{\partial k_M}{\partial \left(V_{fibrils} / V_{heart} \right)} \tag{61}$$

3. Results

The numerically and analytically computed dependencies of various TTR concentrations, the fraction of the heart occupied by TTR fibrils, and the predicted biological age are analyzed for both TTR aggregation scenarios—occurring in blood plasma and cardiac tissue—to determine which scenario yields more physiologically plausible predictions.

It is important to note that in all figures—except those illustrating sensitivity coefficients—the approximate analytical solutions show excellent agreement with the numerical results. Sensitivity coefficients, which represent partial derivatives of the solution with respect to model parameters, are highly sensitive to the accuracy of the underlying solution. As a result, some discrepancies between the analytically and numerically calculated sensitivity coefficients are observed at early time points.

The molar concentration of TTR tetramers, $[T]$, increases rapidly until it reaches a steady-state value. This initial rapid increase occurs due to the assumed zero concentration of $[T]$ at t=0. The steady-state concentration of TTR tetramers is governed by the rate constant for tetramer dissociation into monomers, k_M. The value of q_T is calibrated by setting k_M in Eq. (5) to 4.14 × 10^{-6} s^{-1}, a value reported in (Nelson et al., 2021). At this value, the model yields a tetramer concentration of 4.5 μM, which lies at the midpoint of the physiological range reported in (Coelho et al., 2016). An order-of-magnitude increase in k_M (to 4.14 × 10^{-5} s^{-1}) leads to a fivefold decrease in the steady-state concentration of TTR tetramers, whereas an order-of-magnitude decrease in k_M (to 4.14 × 10^{-7} s^{-1}) results in a twofold increase in tetramer concentration (Fig. S1). Tetramer concentrations are identical in the scenarios of TTR

accumulation in blood plasma and cardiac tissue (see Figs. S1a and S1b), as both are governed by the same Eq. (2) and initial condition (3).

Tafamidis is used in the treatment of TTR amyloidosis. Its effectiveness is attributed to its ability to bind to the native tetrameric form of TTR, thereby stabilizing the tetramer and preventing its dissociation into monomers, which are prone to aggregation (Maurer Mathew S. et al., 2018). The stabilizing effect of tafamidis on TTR tetramers is modeled by reducing the rate constant governing tetramer dissociation into monomers, k_M. A lower k_M leads to an increased concentration of tetramers (Fig. S1). This rise in native TTR (tetramer) concentration with decreasing k_M is consistent with findings reported by (Monteiro et al., 2023).

The concentration of TTR monomers in blood plasma shows a sharp initial decline, caused by the assumed initial condition, and subsequently stabilizes at a low steady-state level (Fig. S2). This aligns with the observations of (Corino et al., 2025), who noted that TTR monomers are highly unstable *in vivo* and generally exist at very low plasma concentrations, $[M]_{pasma}$. For TTR aggregation in cardiac tissue the steady-state values of $[M]_{pasma}$ depend on the value of k_M, with a larger value of k_M corresponding to a larger value of steady-state concentration of $[M]_{pasma}$ (Fig. S2b).

In the scenario where TTR aggregates in the cardiac tissue, the concentration of TTR monomers in the tissue quickly reaches a low steady-state value after a brief transient period. This steady-state concentration is independent of the value of k_M (Fig. S3).

The concentration of TTR oligomers, $[B]_{plasma}$ for scenario 1 and $[B]_{tissue}$ for scenario 2, increases over time until it reaches a steady-state level, which is higher for larger values of the tetramer dissociation constant, k_M (Fig. S4). This can be explained by the fact that higher values of k_M lead to increased production of monomers, which subsequently undergo conversion into oligomers.

Similarly, when TTR aggregates in plasma, the concentration of TTR oligomers incorporated into circulating amyloid protofibrils increases over time and eventually reaches a steady-state level, which is higher for larger values of k_M (Fig. S5).

In the scenario where TTR monomers aggregate in plasma, the total concentration of TTR in blood plasma rises over time and eventually reaches very high levels. For $k_M = 4.14 \times 10^{-6}$ s^{-1}, the steady-state concentration of $[TTR]_{total}$ is approximately 2000 μM (Fig. 2a), suggesting that this scenario is likely

unrealistic. In this scenario, increasing k_M results in a higher steady-state concentration of $[TTR]_{total}$. This is because in this scenario the main components contributing to $[TTR]_{total}$ are TTR oligomers and fibrils circulating in the blood plasma. The concentrations of both components increase with increasing k_M (see Figs. S4a and S5), as TTR monomers are progressively converted into oligomers, which then aggregate into fibrils.

In contrast, when TTR aggregates in cardiac tissue, the total TTR concentration exhibits an initial jump due to the imposed initial condition and then rapidly declines to a steady-state value. For $k_M = 4.14 \times 10^{-6}$ s^{-1}, the steady-state concentration of $[TTR]_{total}$ is approximately 4.5 μM, which is physiologically reasonable (Fig. 2b). In this scenario, increasing k_M leads to a decrease in the steady-state concentration of $[TTR]_{total}$. This is because in this scenario the TTR tetramer concentration constitutes the main component of the total TTR in blood plasma (see Figs. S1b and 2b).

The concentration of TTR oligomers incorporated into amyloid fibrils within cardiac tissue initially rises slowly, then transitions to a linear increase over time (Fig. 3). The rate of this increase, characterized by the slope of the curve, becomes greater with higher values of k_M. Similarly, the fraction of heart volume occupied by TTR amyloid fibrils increases linearly following an initial period, suggesting that fibril accumulation in the heart is primarily governed by the rate at which TTR monomers are supplied through tetramer dissociation (Fig. 4).

It is important to note that, as shown by the black curve in Fig. 4b (marked by empty circles), the predicted volume of TTR fibrils can, in some cases, exceed the total volume of the heart. This occurs because the fibril volume, calculated using Eq. (50), is not constrained by the actual heart volume—an inherent limitation of the proposed model. However, in cases of TTR amyloidosis, cardiac tissue volume may increase due to thickening of the heart walls. Clinically, when the volume occupied by TTR fibrils approaches that of the heart, patients typically succumb to heart failure caused by excessive stiffening of the cardiac muscle.

Biological age increases more rapidly in the scenario where TTR fibrils aggregate within cardiac tissue compared to when fibrils aggregate in the blood plasma (compare Figs. 5b and 5a). In both scenarios, the rate of biological aging also rises with increasing the value of k_M (Fig. 5).

A decrease of k_M thus leads to a reduction in the molar concentration of TTR oligomers deposited into amyloid fibrils within the cardiac tissue, $[I]_{tissue}$ (Fig. 3), the volume fraction of TTR fibrils in the heart, $V_{fibrils} / V_{heart}$ (Fig. 4), and the biological age (Fig. 5).

The molar concentration of TTR tetramers is independent of the half-deposition time of free TTR oligomers into fibrils. As in Fig. S1, the tetramer concentrations shown in Fig. S6 are identical for the scenarios of TTR aggregation in plasma (Fig. S6a) and cardiac tissue (Fig. S6b).

In both scenarios, the molar concentration of TTR monomers in blood plasma reaches a steady-state value that depends on the half-deposition time of free TTR oligomers into fibrils, $\theta_{1/2,B}$ (Fig. S7). A smaller value of $\theta_{1/2,B}$ corresponds to a higher steady-state concentration of monomers, a relationship that warrants a more detailed explanation.

In the scenario where TTR monomers aggregate into free oligomers in the bloodstream, this relationship arises because monomers convert into oligomers via two pathways: primary nucleation, which is slow, and secondary nucleation, which is faster and autocatalyzed by existing free oligomers. A decrease in $\theta_{1/2,B}$ lowers the concentration of free oligomers (Fig. S9a), slowing the autocatalytic conversion of monomers and thereby increasing their steady-state concentration.

In the alternative scenario—where TTR monomers form oligomers within the cardiac tissue—the effect is explained by a compensatory mechanism. At steady state, plasma monomers are deposited into cardiac tissue to replenish the local monomer pool, which is being depleted through conversion into oligomers. A smaller value of $\theta_{1/2,B}$ implies fewer oligomers in the tissue, leading to a lower conversion rate of monomers. Consequently, fewer monomers are drawn from the plasma into the tissue, resulting in a higher plasma monomer concentration.

In the scenario of TTR accumulation in cardiac tissue, the molar concentration of TTR monomers is also higher when the half-deposition time of free TTR oligomers into fibrils, $\theta_{1/2,B}$, is shorter (Fig. S8). A smaller $\theta_{1/2,B}$ results in fewer oligomers accumulating in the tissue (Fig. S9b), as they are more rapidly deposited into fibrils. This reduces the rate of autocatalytic conversion of monomers into oligomers, thereby leading to a higher concentration of monomers in the tissue.

The molar concentrations of TTR oligomers deposited into amyloid protofibrils circulating in the blood plasma reach the same steady-state value for different values of $\theta_{1/2,B}$ (compare the curves for $\theta_{1/2,B} = 10^5$

s and $\theta_{1/2,B} = 10^7$ s in Fig. S10). However, a smaller value of $\theta_{1/2,B}$ leads to a faster approach to steady state, as it corresponds to more rapid deposition of free oligomers into fibrils.

When TTR aggregation is assumed to occur in plasma, the total TTR concentration rises continuously and eventually reaches unrealistically elevated levels. For example, at $\theta_{1/2,B} = 10^7$ s, the model predicts a steady-state concentration of $[TTR]_{total}$ to be approximately 2000 μM (Fig. 6a), which far exceeds values observed *in vivo*, suggesting that this scenario is unlikely to reflect physiological reality.

The rise of steady-state total TTR concentration with increasing $\theta_{1/2,B}$ is primarily driven by the accumulation of TTR oligomers, which make up the dominant fraction of total TTR in the blood plasma in this scenario (see Figs. 6a, S9a, and S10a). As $\theta_{1/2,B}$ increases, oligomer concentrations also rise (Fig. S9a), since the slower deposition of oligomers into fibrils allows them to persist longer in the plasma.

In the scenario where TTR aggregates in cardiac tissue, the total TTR concentration, $[TTR]_{total}$, shows an initial spike due to the imposed initial condition and then quickly declines to a steady-state level. For $\theta_{1/2,B} = 10^7$ s, the steady-state concentration is approximately 4.5 μM, which falls within a physiologically reasonable range (Fig. 6b). In this scenario, increasing $\theta_{1/2,B}$ leads to a decrease in the steady-state concentration of total TTR. This is because in this scenario total TTR consists of the concentrations of circulating TTR tetramers and monomers (see Figs. S6b and S7b). While the tetramer concentration remains unaffected by changes in $\theta_{1/2,B}$ (Fig. S6b), the monomer concentration decreases as $\theta_{1/2,B}$ increases (Fig. S7b). This occurs because monomer-to-oligomer conversion is autocatalyzed by oligomers; thus, increasing the oligomer half-life raises their steady-state levels, enhancing the catalytic conversion of monomers (Fig. S9b).

The molar concentration of TTR oligomers deposited into amyloid fibrils that have infiltrated the cardiac tissue, $[I]_{tissue}$, is approximately five times higher in the scenario where TTR aggregation occurs within the cardiac tissue compared to when aggregation takes place in the plasma (Fig. 7). A smaller value of $\theta_{1/2,B}$ leads to a higher $[I]_{tissue}$ because in this case the deposition of free oligomers into fibrils occurs faster.

The fraction of the heart's volume occupied by TTR amyloid fibrils follows a similar trend (Fig. 8). Notably, for $\theta_{1/2,B} = 10^7$ s, after five years of disease progression, the volume fraction of TTR fibrils in the heart reaches 58% in the tissue aggregation scenario, whereas it reaches only 10% when aggregation

occurs in the plasma. This difference arises because the plasma volume is significantly larger than the volume of the heart. As a result, the local concentration of free oligomers—the drivers of autocatalysis—is much higher in the heart in the scenario when aggregation takes place there, compared to when aggregation occurs in the plasma.

Biological age is calculated using Eq. (56) (Fig. 9). Prior to the onset of TTR amyloidosis—assumed to begin at age 60—biological and calendar ages are identical. However, following the disease onset, biological age advances more rapidly than calendar age due to the accelerated aging effect caused by amyloid fibril deposition in the heart.

In the scenario where TTR aggregation occurs within cardiac tissue, and for $\theta_{1/2,B} = 10^7$ s, the biological age reaches 100 years after five years of disease progression—a value approaching the maximum human lifespan (Fig. 9b). In contrast, when TTR aggregates in the plasma, and for $\theta_{1/2,B} = 10^7$ s, biological age increases to only 71 years after the same disease duration (Fig. 9a). Given that the average survival time for patients with wild-type TTR amyloidosis is approximately five years, the model in which TTR monomers first deposit in cardiac tissue and subsequently aggregate into fibrils appears to more accurately reflect the clinical course of the disease.

The molar concentration of TTR monomers in blood plasma, $[M]_{plasma}$, remains within a reasonable range (not exceeding 0.3 μM at steady state) when $\theta_{1/2,I}$ is varied in the scenario where TTR aggregates in the plasma (Fig. S11a), as well as when h_M is varied in the scenario where TTR aggregation occurs in cardiac tissue (Fig. S11b). In both cases, $[M]_{plasma}$ gradually decreases over time and eventually stabilizes at low steady-state levels.

Assuming that TTR monomers aggregate in plasma leads to a gradual but continuous increase in total TTR concentration, ultimately reaching levels that are not observed under physiological conditions. At $\theta_{1/2,I} = 10^7$ s, the model predicts a steady-state concentration nearing 2000 μM (Fig. S12a), indicating that this aggregation pathway is unlikely to occur *in vivo*. The steady-state concentration of $[TTR]_{total}$ increases with larger values of $\theta_{1/2,I}$.

When TTR aggregation occurs in cardiac tissue, the total TTR concentration initially spikes—due to the prescribed initial condition—and then rapidly decreases to a steady-state value. For $h_M = 10^{-6}$ m·s^{-1}, this

steady-state concentration is approximately 4.6 μM (Fig. S12b), which is within a physiologically acceptable range. Increasing h_M leads to a reduction in the steady-state total TTR concentration.

The molar concentration of TTR oligomers deposited into amyloid fibrils that infiltrate the cardiac tissue, $[I]_{tissue}$, increases over time, consistent with the progressive accumulation of TTR fibrils in the heart as the disease advances (Fig. S13). In the scenario where TTR aggregates in the blood plasma $[I]_{tissue}$ increases as $\theta_{1/2,I}$ decreases (Fig. S13a). This is because lower deposition time promotes more rapid deposition of TTR fibrils into cardiac tissue. In contrast, when TTR aggregates directly within the cardiac tissue, $[I]_{tissue}$ is largely insensitive to changes in h_M (Fig. S13b).

A similar trend is observed for the fraction of heart volume occupied by TTR amyloid fibrils (Fig. S14). As in Fig. 8, after 5 years of the disease this fraction reaches approximately 10% when aggregation occurs in plasma for $\theta_{1/2,I} = 10^7$ s, and increases to 58% when aggregation takes place in cardiac tissue for $h_M = 10^{-6}$ m s^{-1}.

As in Fig. 9a, in the scenario where TTR aggregates in the plasma, the biological age reaches 71 years after 5 years of disease progression for $\theta_{1/2,I} = 10^7$ s (Fig. S15a). In contrast, when TTR aggregates in cardiac tissue, the biological age exceeds 100 years for $h_M = 10^{-6}$ m s^{-1} (see Fig. S15b, also compare with Fig. 9b).

The fraction of heart volume occupied by TTR amyloid fibrils after 5 years of the disease increases with higher dissociation rates of TTR tetramers into monomers, k_M, and with shorter half-deposition times for free TTR oligomers to be incorporated into fibrils, $\theta_{1/2,B}$ (Fig. 10). It is worth noting that for large values of k_M the predicted volume fraction of TTR fibrils can exceed one (Fig. 10b), similar to the behavior observed in Fig. 4b. Biological age after 5 years of the disease follows similar trends: it increases with an increase in k_M and also increases as $\theta_{1/2,B}$ decreases (Fig. 11).

The fraction of heart volume occupied by TTR amyloid fibrils after five years of disease progression decreases as the half-deposition time for free TTR oligomers to be incorporated into fibrils, $\theta_{1/2,B}$, increases (Fig. 12). A longer $\theta_{1/2,B}$ indicates a slower rate of oligomer incorporation into fibrils, resulting in reduced fibril accumulation. Likewise, an increase in the half-deposition time for TTR-derived fibrils circulating in the blood plasma to deposit into cardiac tissue, $\theta_{1/2,I}$, also leads to a lower fibril burden in the heart, as fewer circulating fibrils are deposited (Fig. 12a). In contrast, the mass transfer coefficient

governing the deposition rate of TTR monomers into the endocardium, h_M, shows no significant effect on fibril accumulation (Fig. 12b).

Similarly, biological age after five years of the disease decreases with increasing $\theta_{1/2,B}$ (Fig. 13 and also decreases with increasing fibril deposition half-time from plasma to cardiac tissue, $\theta_{1/2,I}$ (Fig. 13a). In contrast, variations in the mass transfer coefficient for monomer deposition, h_M, have no noticeable impact on biological age (Fig. 13b).

The fraction of heart volume occupied by TTR amyloid fibrils after 5 years of the disease decreases as the half-deposition time for TTR-derived fibrils circulating in the blood plasma to deposit into cardiac tissue $\theta_{1/2,I}$ increases (Fig. S16a), and remains unaffected by changes in the mass transfer coefficient characterizing the rate of TTR monomer deposition into the endocardium, h_M (Fig. S16b). Overall, an increase in $\theta_{1/2,B}$ leads to a reduction in the heart volume occupied by TTR amyloid fibrils (Fig. S16). This is consistent with the findings presented in Fig. 12.

Similarly, biological age after 5 years of the disease decreases as $\theta_{1/2,I}$ increases (Fig. S17a) and remains unaffected by changes in h_M (Fig. S17b). Overall, an increase in $\theta_{1/2,B}$ results in a reduction in biological age. These observations align with the trends shown in Fig. 13.

The sensitivity of the fraction of heart volume occupied by TTR amyloid fibrils with respect to the dissociation rate constant of TTR tetramers into monomers, k_M, is positive, indicating that a higher dissociation rate leads to increased fibril accumulation in the heart. This is consistent with the trend observed in Fig. 11. The sensitivity declines rapidly over time before stabilizing at a positive steady-state value (Fig. 14).

The sensitivity of the fraction of heart volume occupied by TTR amyloid fibrils to the half-deposition time required for free TTR oligomers to be incorporated into fibrils, $\theta_{1/2,B}$, is negative (Fig. 15). This indicates that as $\theta_{1/2,B}$ increases, the volume occupied by TTR fibrils decreases, consistent with the trend observed in Fig. 12. Additionally, increasing $\theta_{1/2,B}$ reduces the magnitude of the sensitivity (Fig. 15).

The sensitivity of the fraction of heart volume occupied by TTR amyloid fibrils to the half-deposition time for TTR-derived fibrils circulating in the blood plasma to deposit into cardiac tissue, $\theta_{1/2,I}$, is negative (Fig. S18a), indicating that an increase in $\theta_{1/2,I}$ leads to a decrease in fibril accumulation. This is consistent with the trend shown in Fig. S16a. In contrast, the volume occupied by TTR fibrils is largely

insensitive to h_M, except at early time points (Fig. S18b). The analytical solution does not depend on h_M (see Eqs. (54) and (55)). Therefore, its sensitivity to h_M is zero, as shown in Fig. S18b.

4. Discussion, limitations of the model, and future directions

This study presents a mathematical model of TTR aggregation dynamics, capturing key features of amyloid deposition in TTR amyloidosis. The obtained analytical solutions closely match numerical results for all quantities except sensitivity coefficients, which diverge at early times due to their strong dependence on solution accuracy; however, at later times, the analytically predicted sensitivity coefficients align very well with the numerical results.

The model simulates two aggregation scenarios, suggested in (Criddle et al., 2024): (1) TTR fibril formation in the bloodstream and (2) TTR aggregation within cardiac tissue. Results demonstrate that fibril accumulation in cardiac tissue leads to physiologically realistic TTR concentrations and disease progression consistent with clinical observations. In contrast, the scenario where fibril formation occurs in plasma predicts unrealistically high total TTR concentrations, which may exceed 2000 μM. Such high concentrations are not observed in patients.

The obtained results support the widely accepted view that tetramer dissociation is the rate-limiting step in amyloidogenesis (Esperante et al., 2021), (Bezerra et al., 2020), and further suggest that fibril growth within cardiac tissue better reflects the clinical course of wild-type transthyretin amyloidosis (ATTR) cardiomyopathy. For example, patients with high cardiac amyloid burden have been shown to exhibit significantly increased mortality (Mehta et al., 2019), a trend that aligns with the simulation results for the tissue aggregation pathway.

The model also captures the therapeutic mechanism of TTR stabilizers such as tafamidis. By reducing the tetramer dissociation rate, tafamidis effectively raises the concentration of native TTR tetramers while limiting the formation of non-native aggregation-prone species (Monteiro et al., 2023), (Nelson et al., 2021). Simulations reported in this paper agree with this experimental observation, showing that a decrease in the tetramer dissociation constant results in higher tetramer concentrations and reduced fibril burden. The model predicts that the molar concentration of TTR tetramers remains unaffected by changes in the fibril deposition kinetics of oligomers, reinforcing the idea that tetramer dissociation is upstream and largely independent of later aggregation stages. Moreover, the model highlights the role of autocatalytic oligomer formation: longer oligomer half-lives result in higher oligomer concentrations,

which in turn accelerates the conversion of monomers into oligomers, particularly when aggregation occurs in plasma.

Importantly, the predicted relationship between fibril deposition and biological age provides additional insights into disease progression. When TTR aggregation occurs within cardiac tissue, the accumulation of fibrils significantly accelerates biological aging, with simulated biological ages reaching 100 years after just five years of disease progression—a pattern consistent with the clinical endpoint of heart failure due to amyloid infiltration. In contrast, when aggregation is modeled in plasma, biological age increases more modestly, reaching only 71 years over the same period. The model further predicts that increased tetramer dissociation accelerates fibril accumulation and biological aging.

These findings are consistent with clinical data suggesting that amyloid fibril deposition contributes directly to tissue dysfunction and age-related decline (Almeida et al., 2024). The model's predictions may be valuable, as (Mehta et al., 2019) suggested that the extent of cardiac amyloidosis burden—measured by the percentage of TTR fibrils in the heart—has prognostic significance, with higher burden linked to increased mortality rates. Overall, the results underscore the importance of targeting early steps in the aggregation cascade—such as tetramer stabilization—as an effective therapeutic strategy for ATTR cardiomyopathy.

The proposed model is a minimal representation of TTR amyloidosis, built on conservation principles for different TTR assembly states, including monomers, oligomers, and fibrils. It simplifies several biophysical processes—for example, TTR aggregation is modeled using the F-W framework, which does not distinguish between different oligomer sizes—highlighting the need for comparison with experimental data for further model development.

Data accessibility. This article has no additional data.

Authors' contributions. AVK is the sole author of this paper.

Competing interests. The author declares no competing interests.

Funding statement. The author acknowledges the support provided by the National Science Foundation (grant CBET-2042834) and the Alexander von Humboldt Foundation through the Humboldt Research Award.

References

Almeida, Z.L., Vaz ,Daniela C., and Brito, R.M.M., 2024. Transthyretin mutagenesis: impact on amyloidogenesis and disease. Critical Reviews in Clinical Laboratory Sciences 61, 616–640. https://doi.org/10.1080/10408363.2024.2350379

Ananda Rao, A., Johncy, S., 2022. Tennis Courts in the Human Body: A Review of the Misleading Metaphor in Medical Literature. Cureus 14, e21474. https://doi.org/10.7759/cureus.21474

Beck, J.V., Arnold, K.J., 1977. Parameter Estimation in Science and Engineering. Wiley, New York.

Betts, J.G., 2013. Anatomy and Physiology, Open Textbook Library. OpenStax College, Rice University.

Bezerra, F., Saraiva, M.J., Almeida, M.R., 2020. Modulation of the Mechanisms Driving Transthyretin Amyloidosis. Frontiers in Molecular Neuroscience Volume 13-2020. https://doi.org/10.3389/fnmol.2020.592644

Boltachev, G.S., Ivanov, M.G., 2020. Effect of nanoparticle concentration on coagulation rate of colloidal suspensions. Heliyon 6, e03295. https://doi.org/10.1016/j.heliyon.2020.e03295

Brunjes, D.L., Castano, A., Clemons, A., Rubin, J., Maurer, M.S., 2016. Transthyretin Cardiac Amyloidosis in Older Americans. J Card Fail 22, 996–1003. https://doi.org/10.1016/j.cardfail.2016.10.008

Cavicchi, R.E., King, J., Ripple, D.C., 2018. Measurement of Average Aggregate Density by Sedimentation and Brownian Motion Analysis. Journal of pharmaceutical sciences 107, 1304–1312. https://doi.org/10.1016/j.xphs.2018.01.013

Coelho, T., Merlini, G., Bulawa, C.E., Fleming, J.A., Judge, D.P., Kelly, J.W., Maurer, M.S., Planté-Bordeneuve, V., Labaudinière, R., Mundayat, R., Riley, S., Lombardo, I., Huertas, P., 2016. Mechanism of Action and Clinical Application of Tafamidis in Hereditary Transthyretin Amyloidosis. Neurol Ther 5, 1–25. https://doi.org/10.1007/s40120-016-0040-x

Concetta Di Nora, Sandro Sponga, Chiara Nalli, Mauro Driussi, Igor Vendramin, Giovanni Benedetti, Giorgio Guzzi, Massimo Imazio, Ugolino Livi, 2022. Heart transplantation in cardiac amyloidosis. Vessel Plus 6, 46. https://doi.org/10.20517/2574-1209.2021.126

Corino, C., Aimo, A., Luigetti, M., Ciccone, L., Ferrari Chen, Y.F., Panichella, G., Musetti, V., Castiglione, V., Vergaro, G., Emdin, M., Franzini, M., 2025. Tetrameric Transthyretin as a Protective Factor Against Alzheimer's Disease. Molecular Neurobiology 62, 2945–2954. https://doi.org/10.1007/s12035-024-04442-8

Criddle, R.S., Hansen, L.D., Woodfield, B.F., Tolley, H.D., 2024. Modeling transthyretin (TTR) amyloid diseases, from monomer to amyloid fibrils. PLoS One 19, e0304891. https://doi.org/10.1371/journal.pone.0304891

Criddle, R.S., Lin, H.-J.L., James, I., Park, J.S., Hansen, L.D., Price, J.C., 2020. Proposing a minimal set of metrics and methods to predict probabilities of amyloidosis disease and onset age in individuals. Aging (Albany NY) 12, 22356–22369. https://doi.org/10.18632/aging.202208

Crimmins, E.M., Klopack, E.T., Kim, J.K., 2024. Generations of epigenetic clocks and their links to socioeconomic status in the Health and Retirement Study. Epigenomics 16, 1031–1042. https://doi.org/10.1080/17501911.2024.2373682

Dorbala Sharmila, Cuddy Sarah, Falk Rodney H., 2020. How to Image Cardiac Amyloidosis. JACC: Cardiovascular Imaging 13, 1368–1383. https://doi.org/10.1016/j.jcmg.2019.07.015

Dormann, D., Lemke, E.A., 2024. Adding intrinsically disordered proteins to biological ageing clocks. Nature Cell Biology 26, 851–858. https://doi.org/10.1038/s41556-024-01423-w

Emdin, M., Morfino, P., Crosta, L., Aimo, A., Vergaro, G., Castiglione, V., 2023. Monoclonal antibodies and amyloid removal as a therapeutic strategy for cardiac amyloidosis. European Heart Journal Supplements 25, B79–B84. https://doi.org/10.1093/eurheartjsupp/suad079

Esperante, S.A., Varejão, N., Pinheiro, F., Sant'Anna, R., Luque-Ortega, J.R., Alfonso, C., Sora, V., Papaleo, E., Rivas, G., Reverter, D., Ventura, S., 2021. Disease-associated mutations impacting

BC-loop flexibility trigger long-range transthyretin tetramer destabilization and aggregation. J Biol Chem 297, 101039. https://doi.org/10.1016/j.jbc.2021.101039
Finke, R.G., Watzky, M.A., Whitehead, C.B., 2020. Response to "Particle Size Is a Primary Determinant for Sigmoidal Kinetics of Nanoparticle Formation: A 'Disproof' of the Finke–Watzky (F-W) Nanoparticle Nucleation and Growth Mechanism." Chemistry of Materials 32, 3657–3672. https://doi.org/10.1021/acs.chemmater.0c00780
Gao, L., Xie, X., Liu, P., Jin, J., 2022. High-avidity binding drives nucleation of amyloidogenic transthyretin monomer. JCI Insight 7. https://doi.org/10.1172/jci.insight.150131
Gladyshev, V.N., Kritchevsky, S.B., Clarke, S.G., Cuervo, A.M., Fiehn, O., de Magalhães, J.P., Mau, T., Maes, M., Moritz, R.L., Niedernhofer, L.J., Van Schaftingen, E., Tranah, G.J., Walsh, K., Yura, Y., Zhang, B., Cummings, S.R., 2021. Molecular damage in aging. Nature Aging 1, 1096–1106. https://doi.org/10.1038/s43587-021-00150-3
Han, J.-D.J., 2024. The ticking of aging clocks. Trends in Endocrinology & Metabolism 35, 11–22. https://doi.org/10.1016/j.tem.2023.09.007
Iashchishyn, I.A., Sulskis, D., Ngoc, M.N., Smirnovas, V., Morozova-Roche, L.A., 2017. Finke-Watzky Two-Step Nucleation-Autocatalysis Model of S100A9 Amyloid Formation: Protein Misfolding as "Nucleation" Event. ACS chemical neuroscience 8, 2152–2158. https://doi.org/10.1021/acschemneuro.7b00251
Kittleson, M.M., Maurer, M.S., Ambardekar, A.V., Bullock-Palmer, R.P., Chang, P.P., Eisen, H.J., Nair, A.P., Nativi-Nicolau, J., Ruberg, F.L., On behalf of the American Heart Association Heart Failure and Transplantation Committee of the Council on Clinical Cardiology, 2020. Cardiac Amyloidosis: Evolving Diagnosis and Management: A Scientific Statement From the American Heart Association. Circulation 142, e7–e22. https://doi.org/10.1161/CIR.0000000000000792
Kuznetsov, A.V., 2025a. Predicting Biological Age Using an Accumulated Neurotoxicity Biomarker for Amyloid Beta Oligomers. bioRxiv 2025.02.28.640920. https://doi.org/10.1101/2025.02.28.640920
Kuznetsov, A.V., 2025b. Modeling the growth of cytosolic TDP-43 inclusion bodies and accumulated neurotoxicity of misfolded oligomers in neurons. bioRxiv 2023.11.28.569118. https://doi.org/10.1101/2023.11.28.569118
Kuznetsov, I.A., Kuznetsov, A.V., 2019. Investigating sensitivity coefficients characterizing the response of a model of tau protein transport in an axon to model parameters. Computer methods in biomechanics and biomedical engineering 22, 71–83. https://doi.org/10.1080/10255842.2018.1534233
Li, S.Z., Jain, A. (Eds.), 2009. Capillary Blood Vessel, in: Encyclopedia of Biometrics. Springer US, Boston, MA, pp. 178–178. https://doi.org/10.1007/978-0-387-73003-5_133
Maurer Mathew S., Schwartz Jeffrey H., Gundapaneni Balarama, Elliott Perry M., Merlini Giampaolo, Waddington-Cruz Marcia, Kristen Arnt V., Grogan Martha, Witteles Ronald, Damy Thibaud, Drachman Brian M., Shah Sanjiv J., Hanna Mazen, Judge Daniel P., Barsdorf Alexandra I., Huber Peter, Patterson Terrell A., Riley Steven, Schumacher Jennifer, Stewart Michelle, Sultan Marla B., Rapezzi Claudio, 2018. Tafamidis Treatment for Patients with Transthyretin Amyloid Cardiomyopathy. New England Journal of Medicine 379, 1007–1016. https://doi.org/10.1056/NEJMoa1805689
Mehta, P., Chapel, D.B., Goyal, N., Yu, D.B., Mor-Avi, V., Narang, A., Addetia, K., Sarswat, N., Lang, R.M., Husain, A.N., Patel, A.R., 2019. A histopathologic schema to quantify the burden of cardiac amyloidosis: Relationship with survival and echocardiographic parameters. Echocardiography 36, 285–291. https://doi.org/10.1111/echo.14245
Min, M., Egli, C., Dulai, A.S., Sivamani, R.K., 2024. Critical review of aging clocks and factors that may influence the pace of aging. Front Aging 5, 1487260. https://doi.org/10.3389/fragi.2024.1487260

Miroy, G.J., Lai, Z., Lashuel, H.A., Peterson, S.A., Strang, C., Kelly, J.W., 1996. Inhibiting transthyretin amyloid fibril formation via protein stabilization. Proceedings of the National Academy of Sciences 93, 15051–15056. https://doi.org/10.1073/pnas.93.26.15051

Molina, D.K., DiMaio, V.J.M., 2012. Normal organ weights in men: part II-the brain, lungs, liver, spleen, and kidneys. Am J Forensic Med Pathol 33, 368–372. https://doi.org/10.1097/PAF.0b013e31823d29ad

Monteiro, C., Mesgarzadeh ,Jaleh S., Anselmo ,João, Fernandes ,Joana, Novais ,Marta, Rodrigues ,Carla, Powers ,David L., Powers ,Evan T., Coelho ,Teresa, and Kelly, J.W., 2023. Tafamidis polyneuropathy amelioration requires modest increases in transthyretin stability even though increases in plasma native TTR and decreases in non-native TTR do not predict response. Amyloid 30, 81–95. https://doi.org/10.1080/13506129.2022.2126308

Morfino, P., Aimo, A., Panichella, G., Rapezzi, C., Emdin, M., 2022. Amyloid seeding as a disease mechanism and treatment target in transthyretin cardiac amyloidosis. Heart Failure Reviews 27, 2187–2200. https://doi.org/10.1007/s10741-022-10237-7

Morris, A.M., Watzky, M.A., Agar, J.N., Finke, R.G., 2008. Fitting neurological protein aggregation kinetic data via a 2-step, Minimal/"Ockham's Razor" model: The Finke-Watzky mechanism of nucleation followed by autocatalytic surface growth. Biochemistry 47, 2413–2427. https://doi.org/10.1021/bi701899y

Nelson, L.T., Paxman ,Ryan J., Xu ,Jin, Webb ,Bill, Powers ,Evan T., and Kelly, J.W., 2021. Blinded potency comparison of transthyretin kinetic stabilisers by subunit exchange in human plasma. Amyloid 28, 24–29. https://doi.org/10.1080/13506129.2020.1808783

Powers, E.T., Kelly, J.W., 2021. Chapter 4 - From uncovering the mechanism of transthyretin aggregation to the drug tafamidis for ameliorating neurodegeneration and cardiomyopathy, in: Smith, R.A., Kaspar, B.K., Svendsen, C.N. (Eds.), Neurotherapeutics in the Era of Translational Medicine. Academic Press, pp. 65–103. https://doi.org/10.1016/B978-0-12-816475-4.00004-5

Quintas, A., Saraiva, M., Brito, R., 1999. The tetrameric protein transthyretin dissociates to a non-native monomer in solution - A novel model for amyloidogenesis. JOURNAL OF BIOLOGICAL CHEMISTRY 274, 32943–32949. https://doi.org/10.1074/jbc.274.46.32943

Rinauro, D.J., Chiti, F., Vendruscolo, M., Limbocker, R., 2024. Misfolded protein oligomers: mechanisms of formation, cytotoxic effects, and pharmacological approaches against protein misfolding diseases. Molecular Neurodegeneration 19, 20. https://doi.org/10.1186/s13024-023-00651-2

Ruberg, F.L., Berk, J.L., 2012. Transthyretin (TTR) cardiac amyloidosis. Circulation 126, 1286–1300. https://doi.org/10.1161/CIRCULATIONAHA.111.078915

Ruberg, F.L., Grogan, M., Hanna, M., Kelly, J.W., Maurer, M.S., 2019. Transthyretin Amyloid Cardiomyopathy: JACC State-of-the-Art Review. J Am Coll Cardiol 73, 2872–2891. https://doi.org/10.1016/j.jacc.2019.04.003

Sanguinetti, C., Minniti, M., Susini, V., Caponi, L., Panichella, G., Castiglione, V., Aimo, A., Emdin, M., Vergaro, G., Franzini, M., 2022. The Journey of Human Transthyretin: Synthesis, Structure Stability, and Catabolism. Biomedicines 10. https://doi.org/10.3390/biomedicines10081906

Schmidt, M., Wiese, S., Adak, V., Engler, J., Agarwal, S., Fritz, G., Westermark, P., Zacharias, M., Fändrich, M., 2019. Cryo-EM structure of a transthyretin-derived amyloid fibril from a patient with hereditary ATTR amyloidosis. Nat Commun 10, 5008. https://doi.org/10.1038/s41467-019-13038-z

Sharma, R., Sharma, S., 2025. Physiology, Blood Volume., in: StatPearls. StatPearls Publishing, Treasure Island (FL).

Smiley, D.A., Rodriguez, C.M., Maurer, M.S., 2022. Transthyretin Cardiac Amyloidosis: An Evolution in Diagnosis and Management of an "Old" Disease. Cardiology Clinics 40, 541–558. https://doi.org/10.1016/j.ccl.2022.06.008

Steinebrei, M., Baur, J., Pradhan, A., Kupfer, N., Wiese, S., Hegenbart, U., Schönland, S.O., Schmidt, M., Fändrich, M., 2023. Common transthyretin-derived amyloid fibril structures in patients with hereditary ATTR amyloidosis. Nature Communications 14, 7623. https://doi.org/10.1038/s41467-023-43301-3

Vetri, V., Foderà, V., 2015. The route to protein aggregate superstructures: Particulates and amyloid-like spherulites. FEBS Letters 589, 2448–2463. https://doi.org/10.1016/j.febslet.2015.07.006

Wang, Qingyi, Hou, T., Wang, Qiwen, He, J., Wang, L., Si, J., Chen, S., 2023. An evaluation of aging measures: from biomarkers to clocks. Biogerontology 24, 303–328. https://doi.org/10.1007/s10522-022-09997-4

Watzky, M.A., Finney, E.E., Finke, R.G., 2008. Transition-Metal Nanocluster Size vs Formation Time and the Catalytically Effective Nucleus Number: A Mechanism-Based Treatment. Journal of the American Chemical Society 130, 11959–11969. https://doi.org/10.1021/ja8017412

Williams, M.A.C., Shankar, B., Vaishnav, J., Ranek, M.J., 2022. Current and potential therapeutic strategies for transthyretin cardiac amyloidosis. Frontiers in Drug Discovery Volume 2-2022. https://doi.org/10.3389/fddsv.2022.1015545

Zadeh, K.S., Montas, H.J., 2010. A class of exact solutions for biomacromolecule diffusion-reaction in live cells. Journal of theoretical biology 264, 914–933. https://doi.org/10.1016/j.jtbi.2010.03.028

Zi, Z., 2011. Sensitivity analysis approaches applied to systems biology models. Iet Systems Biology 5, 336–346. https://doi.org/10.1049/iet-syb.2011.0015

Figure captions

Fig. 1. Schematic diagram illustrating two possible scenarios by which TTR fibril deposits may form in the heart: (a) TTR monomers misfold and assemble into protofibrillar formations within the bloodstream before depositing in the heart. (b) TTR monomers remain in circulation until they directly attach to sites within the heart, where they form amyloid deposits *in situ*. *Figure generated with the aid of servier medical art, licensed under a creative commons attribution 3.0 generic license. http://Smart.servier.com.*

Fig. 2. Total concentration of TTR (in any state) in the blood plasma vs time for various values of the rate constant describing the dissociation of TTR tetramers into monomers. (a) Scenario when TTR monomers misfold and assemble into protofibrillar formations within the bloodstream before depositing in the heart. (b) Scenario when TTR monomers remain in circulation until they directly attach to sites within the heart, where they form amyloid deposits *in situ*.

Fig. 3. Molar concentration of TTR oligomers deposited into amyloid fibrils that infiltrated the cardiac tissue vs time for various values of the rate constant describing the dissociation of TTR tetramers into monomers. (a) Scenario when TTR monomers misfold and assemble into protofibrillar formations within the bloodstream before depositing in the heart. (b) Scenario when TTR monomers remain in circulation until they directly attach to sites within the heart, where they form amyloid deposits *in situ*.

Fig. 4. Fraction of heart volume occupied by TTR amyloid fibrils vs time for various values of the rate constant describing the dissociation of TTR tetramers into monomers. (a) Scenario when TTR monomers misfold and assemble into protofibrillar formations within the bloodstream before depositing in the heart. (b) Scenario when TTR monomers remain in circulation until they directly attach to sites within the heart, where they form amyloid deposits *in situ*.

Fig. 5. Biological age vs calendar age for various values of the rate constant describing the dissociation of TTR tetramers into monomers. (a) Scenario when TTR monomers misfold and assemble into protofibrillar formations within the bloodstream before depositing in the heart. (b) Scenario when TTR monomers remain in circulation until they directly attach to sites within the heart, where they form amyloid deposits *in situ*.

Fig. 6. Total concentration of TTR (in any state) in the blood plasma vs time for various values of the half-deposition time for free TTR oligomers to become incorporated into TTR fibrils. (a) Scenario when TTR monomers misfold and assemble into protofibrillar formations within the bloodstream before depositing in the heart. (b) Scenario when TTR monomers remain in circulation until they directly attach to sites within the heart, where they form amyloid deposits *in situ*.

Fig. 7. Molar concentration of TTR oligomers deposited into amyloid fibrils that infiltrated the cardiac tissue vs time for various values of the half-deposition time for free TTR oligomers to become incorporated into TTR fibrils. (a) Scenario when TTR monomers misfold and assemble into protofibrillar formations within the bloodstream before depositing in the heart. (b) Scenario when TTR monomers remain in circulation until they directly attach to sites within the heart, where they form amyloid deposits *in situ*.

Fig. 8. Fraction of heart volume occupied by TTR amyloid fibrils vs time for various values of the half-deposition time for free TTR oligomers to become incorporated into TTR fibrils. (a) Scenario when TTR monomers misfold and assemble into protofibrillar formations within the bloodstream before depositing in the heart. (b) Scenario when TTR monomers remain in circulation until they directly attach to sites within the heart, where they form amyloid deposits *in situ*.

Fig. 9. Biological age vs calendar age for various values of the half-deposition time for free TTR oligomers to become incorporated into TTR fibrils. (a) Scenario when TTR monomers misfold and assemble into protofibrillar formations within the bloodstream before depositing in the heart. (b) Scenario when TTR monomers remain in circulation until they directly attach to sites within the heart, where they form amyloid deposits *in situ*.

Fig. 10. Fraction of heart volume occupied by TTR amyloid fibrils as a function of the rate constant describing the dissociation of TTR tetramers into monomers, k_M. (a) Scenario in which TTR monomers misfold and assemble into protofibrils within the bloodstream before depositing in the heart, shown for various values of $\theta_{1/2,B}$. (b) Scenario in which TTR monomers circulate until they directly bind to sites in the heart and form amyloid deposits *in situ*, shown for various values of $\theta_{1/2,B}$.

Fig. 11. Biological age vs calendar age as a function of the rate constant describing the dissociation of TTR tetramers into monomers, k_M. (a) Scenario in which TTR monomers misfold and assemble into protofibrils within the bloodstream before depositing in the heart, shown for various values of $\theta_{1/2,B}$. (b) Scenario in which TTR monomers circulate until they directly bind to sites in the heart and form amyloid deposits *in situ*, shown for various values of $\theta_{1/2,B}$.

Fig. 12. Fraction of heart volume occupied by TTR amyloid fibrils as a function of the half-deposition time required for free TTR oligomers to become incorporated into fibrils, $\theta_{1/2,B}$. (a) Scenario in which TTR monomers misfold and assemble into protofibrils within the bloodstream before depositing in the

heart, shown for various values of $\theta_{1/2,I}$. (b) Scenario in which TTR monomers circulate until they directly bind to sites in the heart and form amyloid deposits *in situ*, shown for various values of h_M .

Fig. 13. Biological age vs calendar age as a function of the half-deposition time required for free TTR oligomers to become incorporated into fibrils, $\theta_{1/2,B}$. (a) Scenario in which TTR monomers misfold and assemble into protofibrils within the bloodstream before depositing in the heart, shown for various values of $\theta_{1/2,I}$. (b) Scenario in which TTR monomers circulate until they directly bind to sites in the heart and form amyloid deposits *in situ*, shown for various values of h_M .

Fig. 14. Dimensionless sensitivity of the fraction of heart volume occupied by TTR amyloid fibrils to the rate constant describing the dissociation of TTR tetramers into monomers, k_M , shown as a function of time. (a) Scenario in which TTR monomers misfold and assemble into protofibrillar structures within the bloodstream before depositing in the heart. (b) Scenario in which TTR monomers remain in circulation until they directly bind to sites within the heart, where they form amyloid deposits *in situ*.

Fig. 15. Dimensionless sensitivity of the fraction of heart volume occupied by TTR amyloid fibrils to the half-deposition time required for free TTR oligomers to be incorporated into fibrils, $\theta_{1/2,B}$, shown as a function of time. (a) Scenario in which TTR monomers misfold and assemble into protofibrillar structures within the bloodstream before depositing in the heart. (b) Scenario in which TTR monomers remain in circulation until they directly bind to sites within the heart, where they form amyloid deposits *in situ*.

(a)

$$T \xrightarrow{k_M} 4M$$

$$M \xrightarrow{k_1} B$$

$$M + B \xrightarrow{k_2} 2B$$

$$B \xrightarrow{\ln(2)/\theta_{1/2,B}} I_{plasma}$$

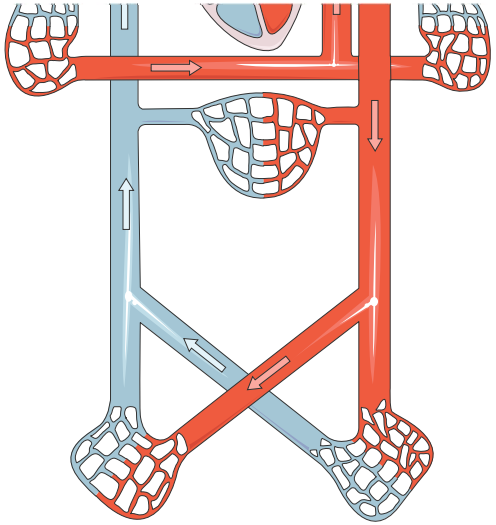

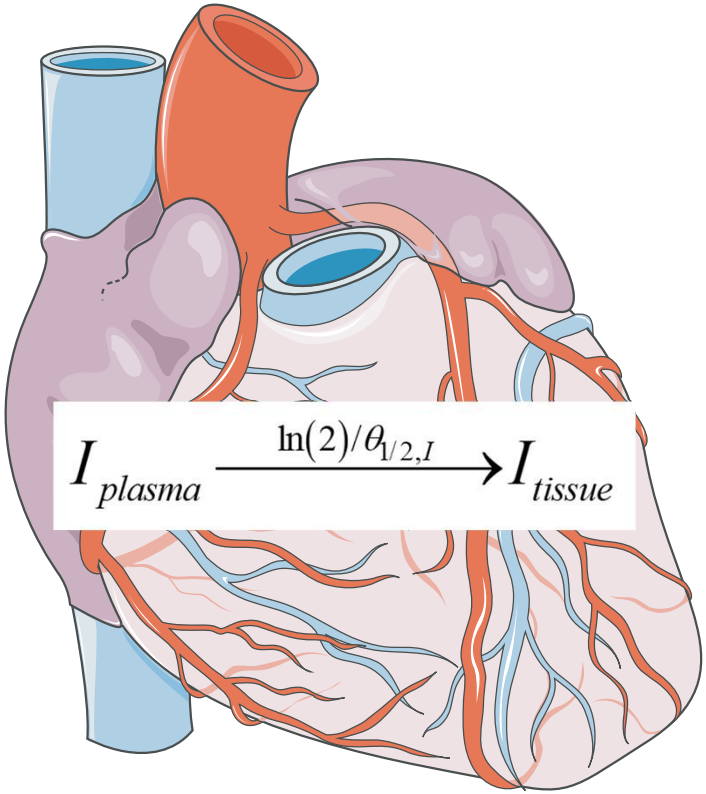

Fig. 1a

(b)

$$T \xrightarrow{k_M} 4M_{plasma}$$

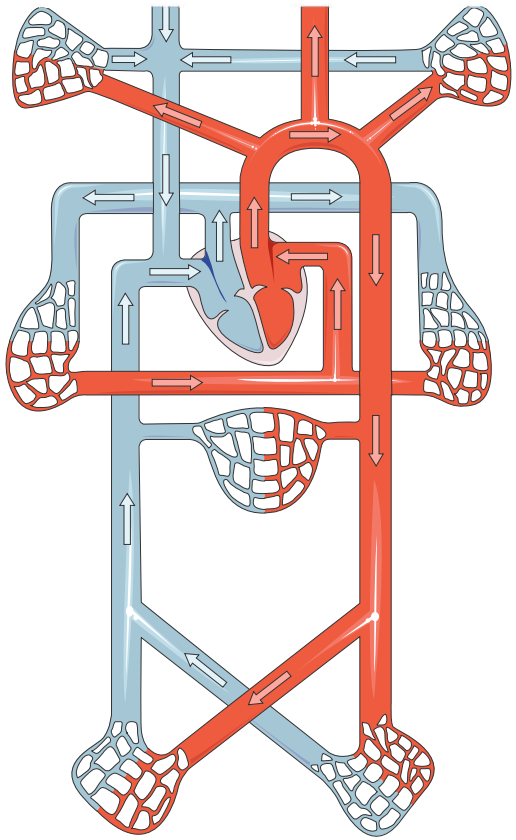

$$M_{plasma} \xrightarrow{h_M \frac{S_{heart}}{V_{heart}}\left([M]_{plasma} - [M]_{tissue}\right)/M_{plasma}} M_{tissue}$$

$$M_{tissue} \xrightarrow{k_1} B$$

$$M_{tissue} + B \xrightarrow{k_2} 2B$$

$$B \xrightarrow{\ln(2)/\theta_{1/2,B}} I_{tissue}$$

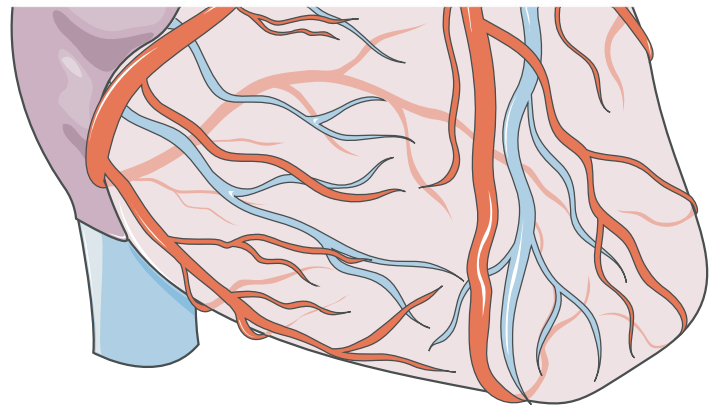

Fig. 1b

(a)

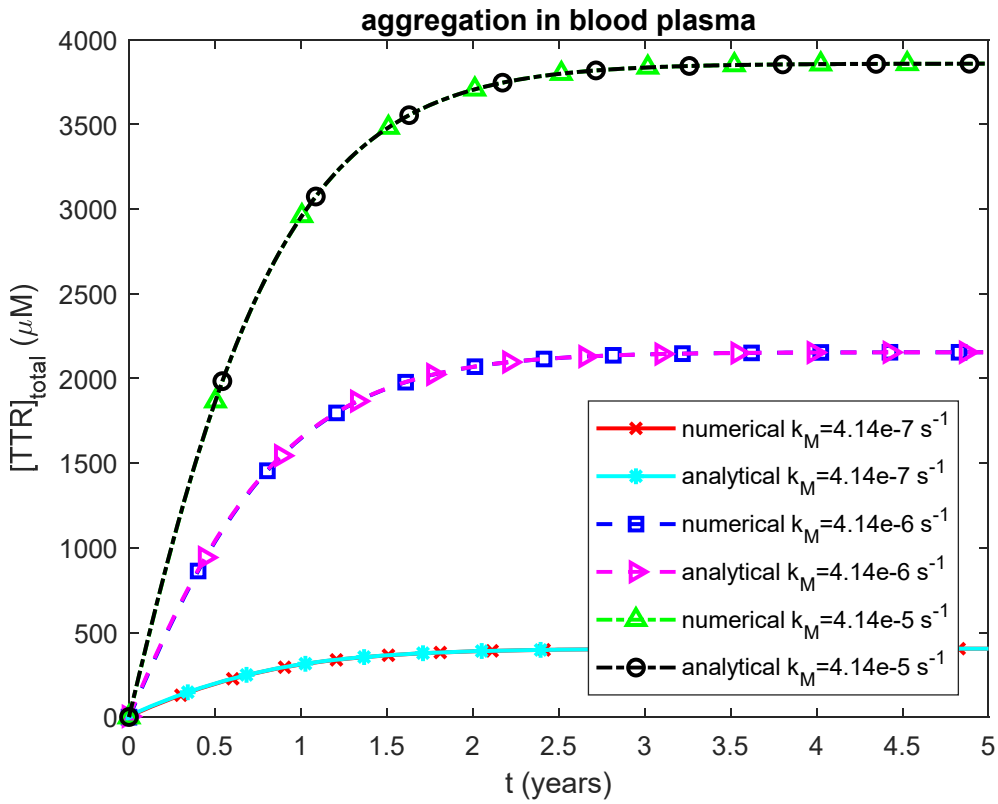
aggregation in blood plasma
[TTR]total (μM)
t (years)
numerical kM=4.14e-7 s-1
analytical kM=4.14e-7 s-1
numerical kM=4.14e-6 s-1
analytical kM=4.14e-6 s-1
numerical kM=4.14e-5 s-1
analytical kM=4.14e-5 s-1

(b)

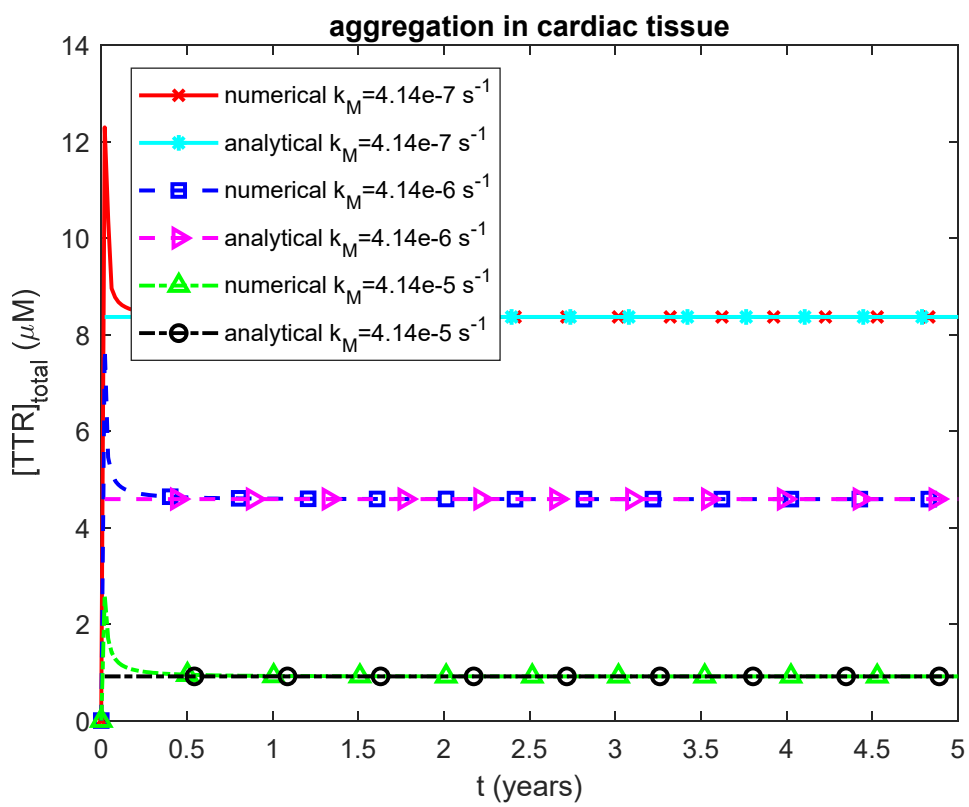
aggregation in cardiac tissue
[TTR]total (μM)
t (years)
numerical kM=4.14e-7 s-1
analytical kM=4.14e-7 s-1
numerical kM=4.14e-6 s-1
analytical kM=4.14e-6 s-1
numerical kM=4.14e-5 s-1
analytical kM=4.14e-5 s-1

Figure 2

(a)

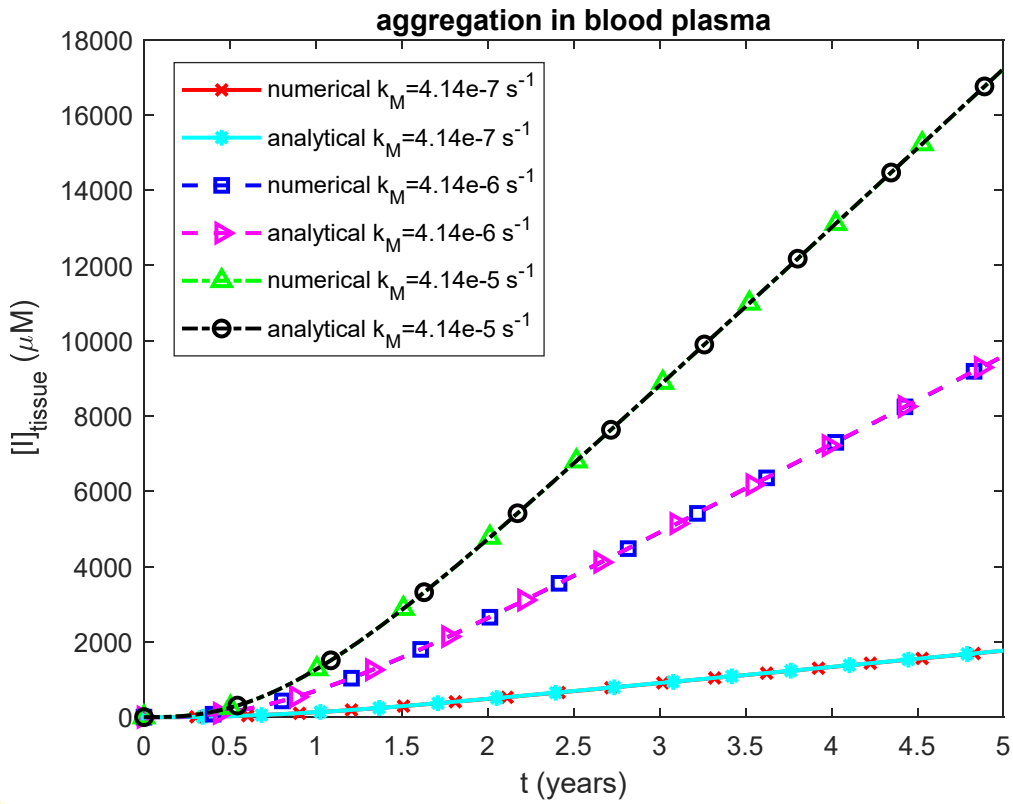
aggregation in blood plasma
numerical k_M=4.14e-7 s^{-1}
analytical k_M=4.14e-7 s^{-1}
numerical k_M=4.14e-6 s^{-1}
analytical k_M=4.14e-6 s^{-1}
numerical k_M=4.14e-5 s^{-1}
analytical k_M=4.14e-5 s^{-1}
$[I]_{tissue}$ (μM)
t (years)
0
2000
4000
6000
8000
10000
12000
14000
16000
18000
0.5
1
1.5
2
2.5
3
3.5
4
4.5
5

(b)

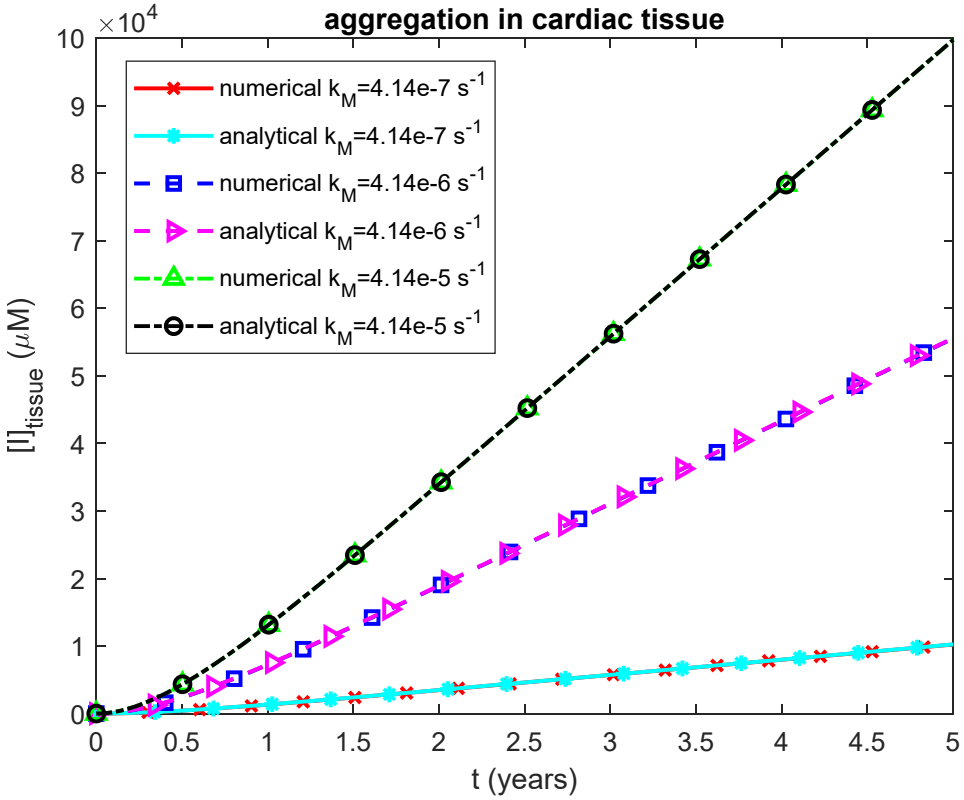
aggregation in cardiac tissue
$\times 10^4$
numerical k_M=4.14e-7 s^{-1}
analytical k_M=4.14e-7 s^{-1}
numerical k_M=4.14e-6 s^{-1}
analytical k_M=4.14e-6 s^{-1}
numerical k_M=4.14e-5 s^{-1}
analytical k_M=4.14e-5 s^{-1}
$[I]_{tissue}$ (μM)
t (years)
0
1
2
3
4
5
6
7
8
9
10
0.5
1
1.5
2
2.5
3
3.5
4
4.5
5

Figure 3

(a)

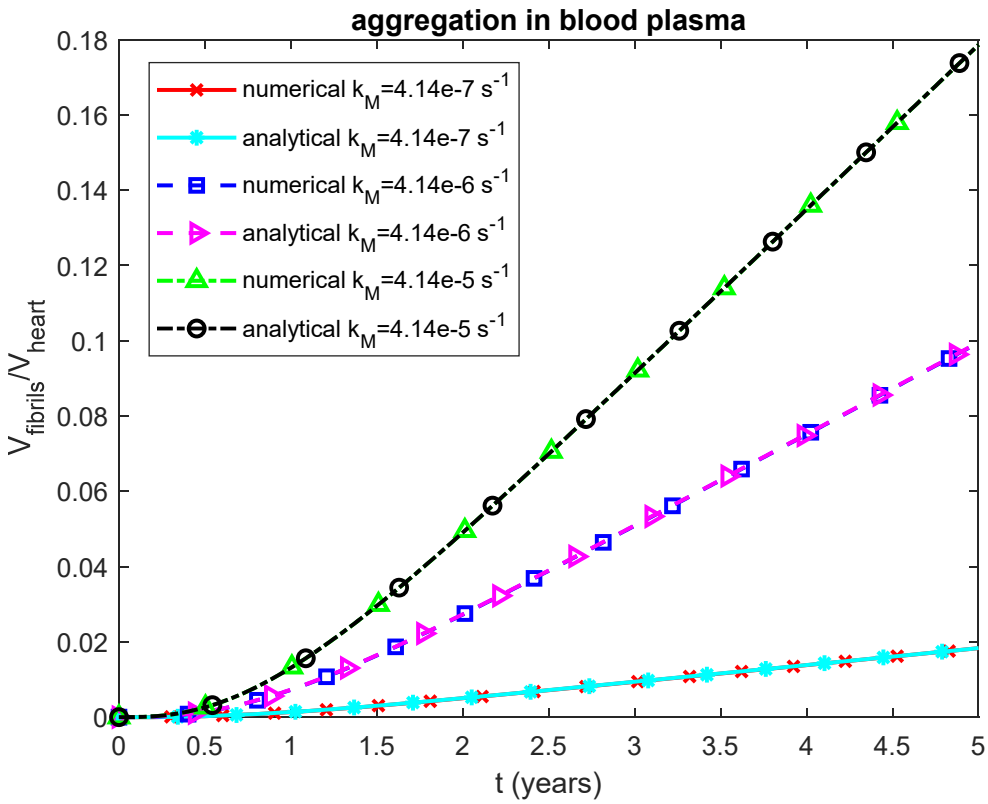
aggregation in blood plasma
numerical k_M=4.14e-7 s^{-1}
analytical k_M=4.14e-7 s^{-1}
numerical k_M=4.14e-6 s^{-1}
analytical k_M=4.14e-6 s^{-1}
numerical k_M=4.14e-5 s^{-1}
analytical k_M=4.14e-5 s^{-1}
$V_{fibrils}/V_{heart}$
t (years)
0
0.02
0.04
0.06
0.08
0.1
0.12
0.14
0.16
0.18
0.5
1
1.5
2
2.5
3
3.5
4
4.5
5

(b)

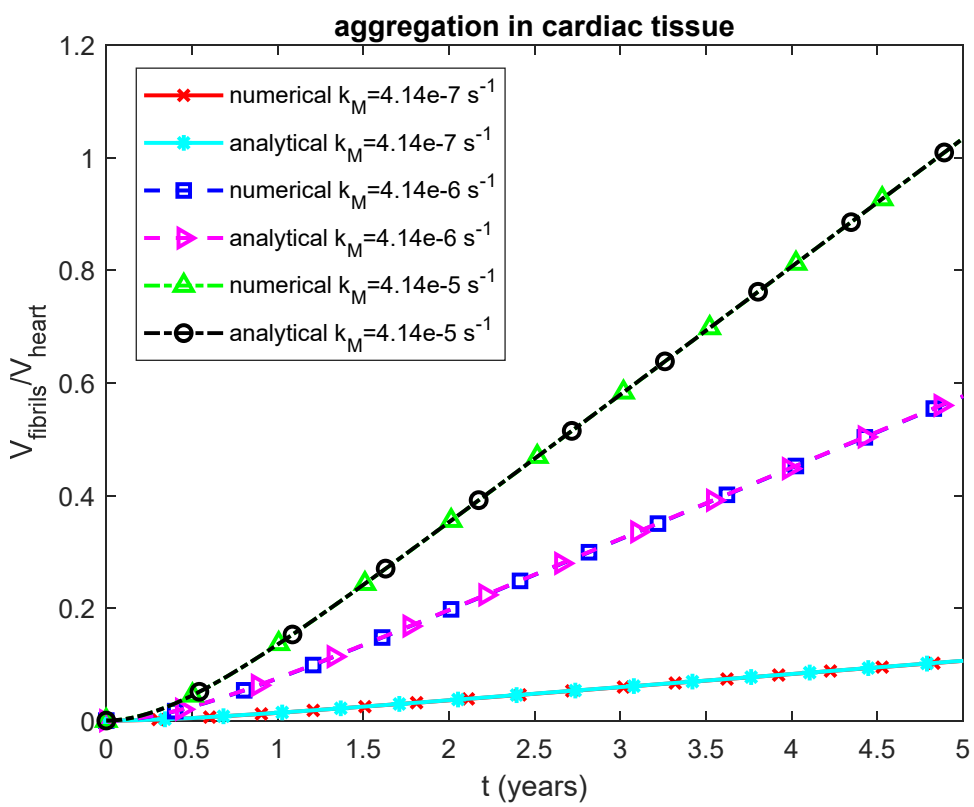
aggregation in cardiac tissue
numerical k_M=4.14e-7 s^{-1}
analytical k_M=4.14e-7 s^{-1}
numerical k_M=4.14e-6 s^{-1}
analytical k_M=4.14e-6 s^{-1}
numerical k_M=4.14e-5 s^{-1}
analytical k_M=4.14e-5 s^{-1}
$V_{fibrils}/V_{heart}$
t (years)
0
0.2
0.4
0.6
0.8
1
1.2
0.5
1
1.5
2
2.5
3
3.5
4
4.5
5

Figure 4

(a)

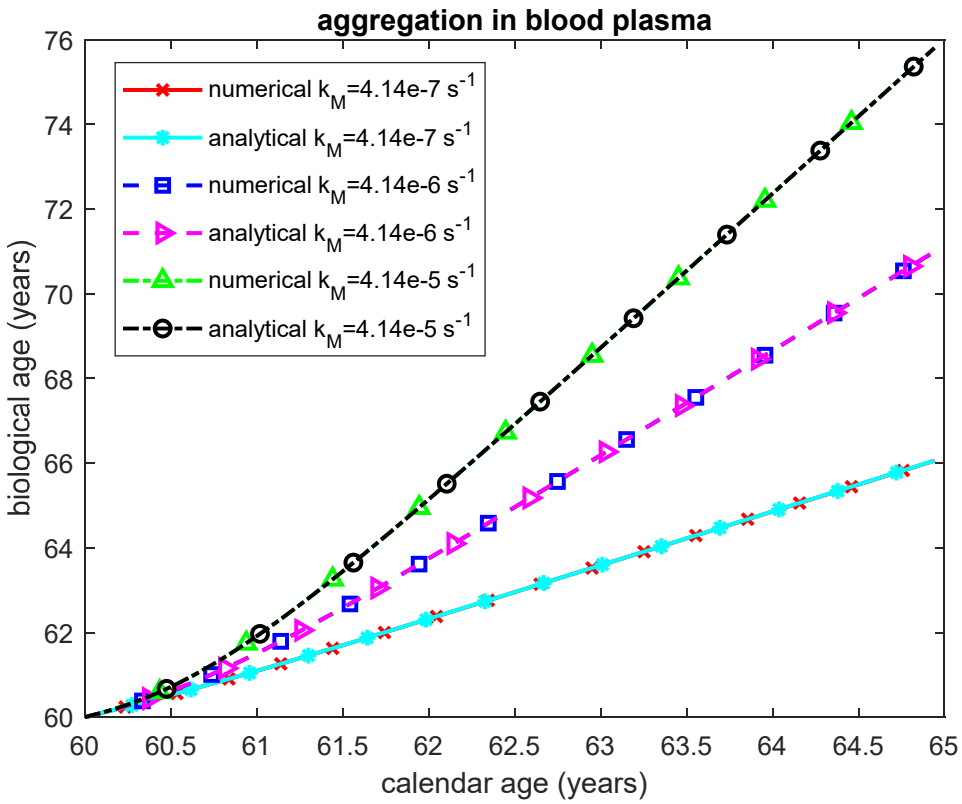
aggregation in blood plasma
numerical k_M=4.14e-7 s^{-1}
analytical k_M=4.14e-7 s^{-1}
numerical k_M=4.14e-6 s^{-1}
analytical k_M=4.14e-6 s^{-1}
numerical k_M=4.14e-5 s^{-1}
analytical k_M=4.14e-5 s^{-1}
biological age (years)
calendar age (years)
60
62
64
66
68
70
72
74
76
60
60.5
61
61.5
62
62.5
63
63.5
64
64.5
65

(b)

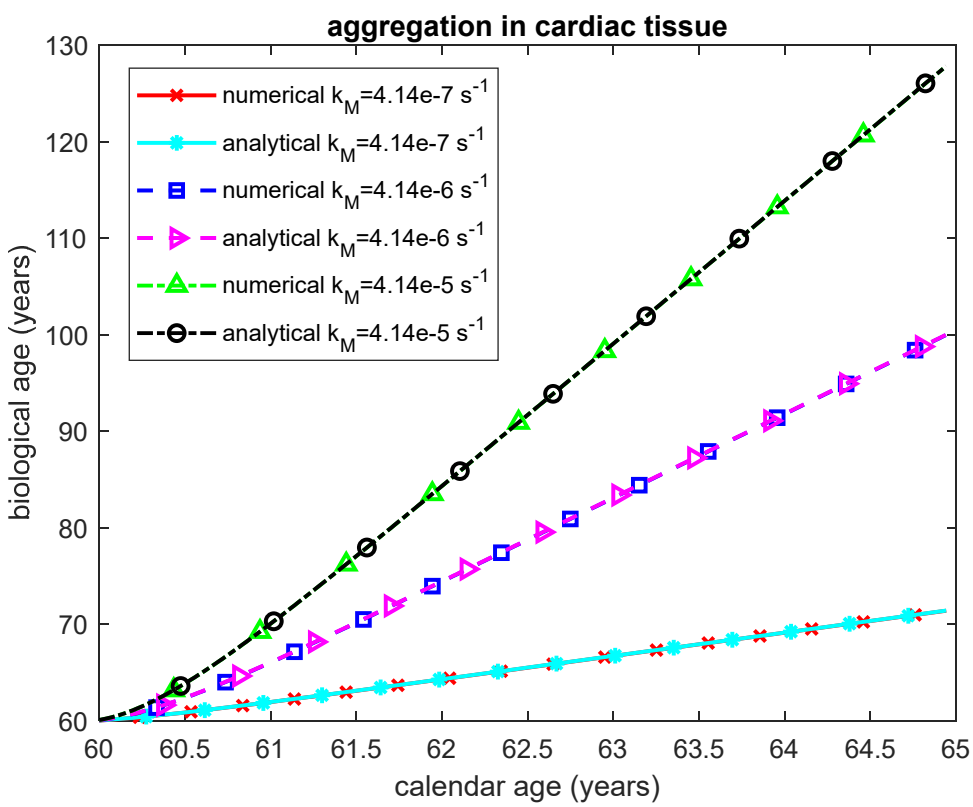
aggregation in cardiac tissue
numerical k_M=4.14e-7 s^{-1}
analytical k_M=4.14e-7 s^{-1}
numerical k_M=4.14e-6 s^{-1}
analytical k_M=4.14e-6 s^{-1}
numerical k_M=4.14e-5 s^{-1}
analytical k_M=4.14e-5 s^{-1}
biological age (years)
calendar age (years)
60
70
80
90
100
110
120
130
60
60.5
61
61.5
62
62.5
63
63.5
64
64.5
65

Figure 5

(a)

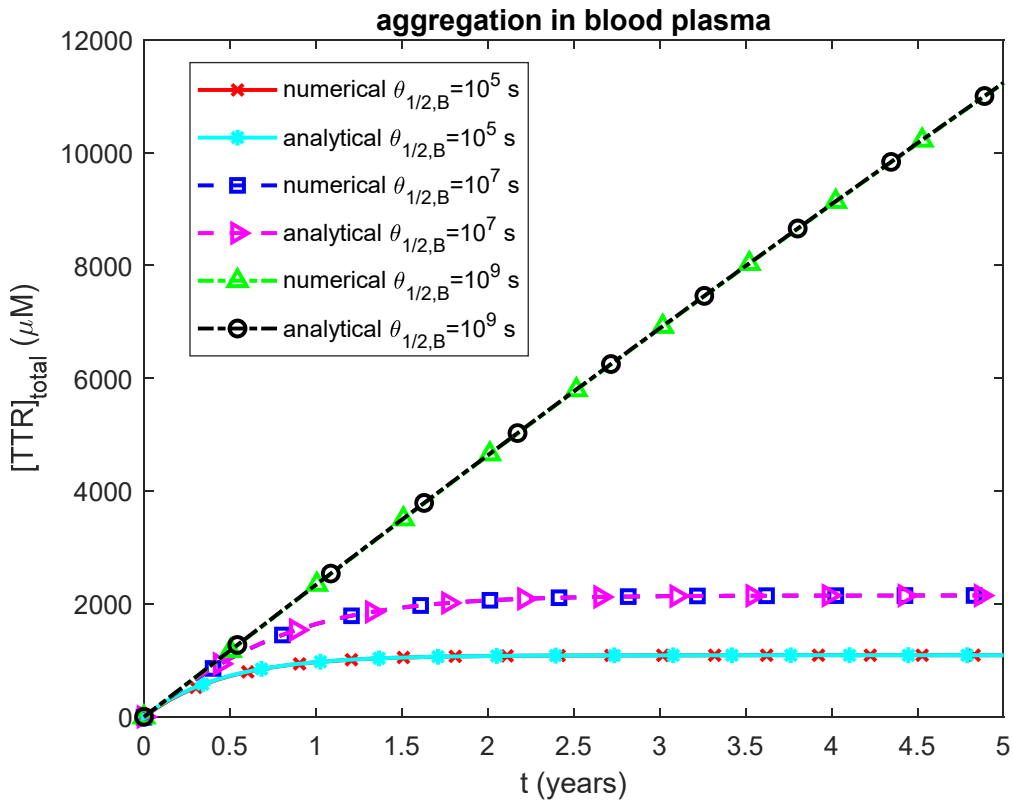
aggregation in blood plasma
numerical $\theta_{1/2,B}$=10^5 s
analytical $\theta_{1/2,B}$=10^5 s
numerical $\theta_{1/2,B}$=10^7 s
analytical $\theta_{1/2,B}$=10^7 s
numerical $\theta_{1/2,B}$=10^9 s
analytical $\theta_{1/2,B}$=10^9 s
$[TTR]_{total}$ (μM)
t (years)
0
2000
4000
6000
8000
10000
12000
0.5
1
1.5
2
2.5
3
3.5
4
4.5
5

(b)

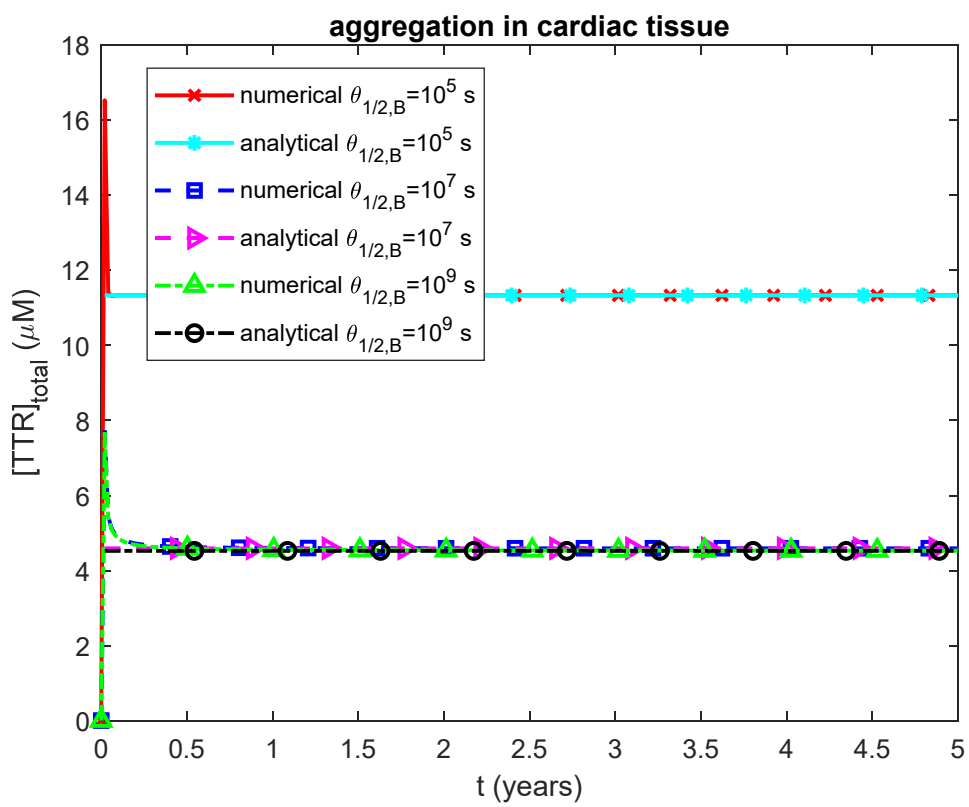
aggregation in cardiac tissue
numerical $\theta_{1/2,B}$=10^5 s
analytical $\theta_{1/2,B}$=10^5 s
numerical $\theta_{1/2,B}$=10^7 s
analytical $\theta_{1/2,B}$=10^7 s
numerical $\theta_{1/2,B}$=10^9 s
analytical $\theta_{1/2,B}$=10^9 s
$[TTR]_{total}$ (μM)
t (years)
0
2
4
6
8
10
12
14
16
18
0.5
1
1.5
2
2.5
3
3.5
4
4.5
5

Figure 6

(a)

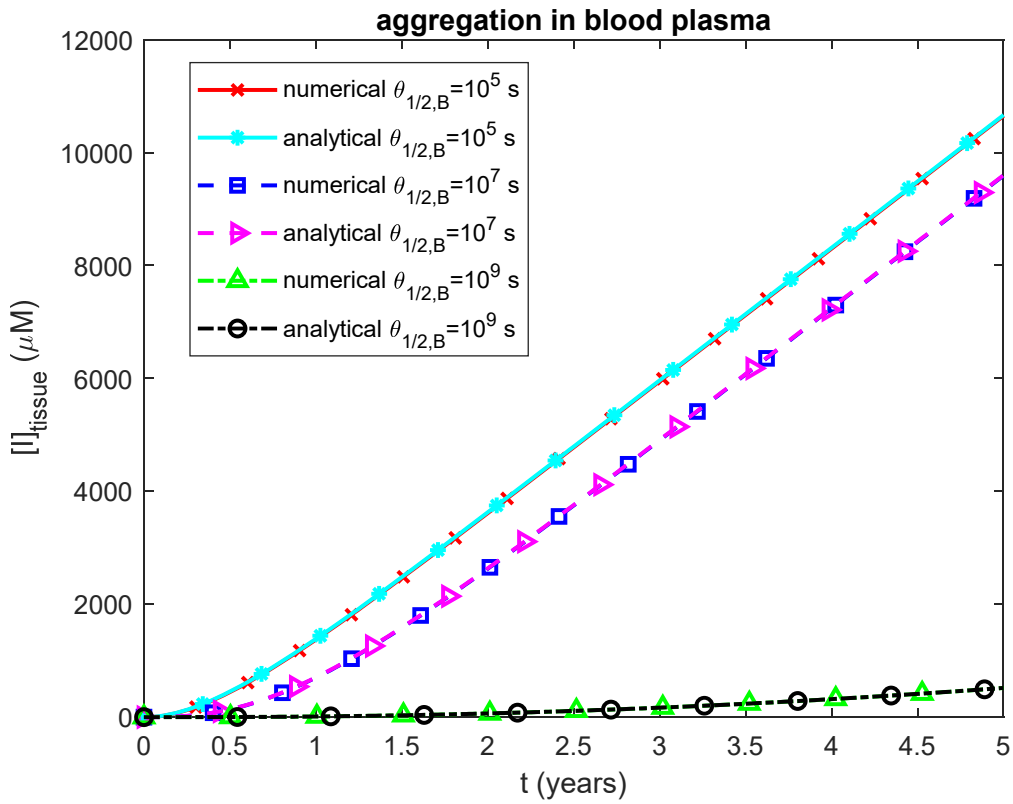
aggregation in blood plasma
numerical $\theta_{1/2,B}$=10^5 s
analytical $\theta_{1/2,B}$=10^5 s
numerical $\theta_{1/2,B}$=10^7 s
analytical $\theta_{1/2,B}$=10^7 s
numerical $\theta_{1/2,B}$=10^9 s
analytical $\theta_{1/2,B}$=10^9 s
$[I]_{tissue}$ (μM)
t (years)
0
2000
4000
6000
8000
10000
12000
0.5
1
1.5
2
2.5
3
3.5
4
4.5
5

(b)

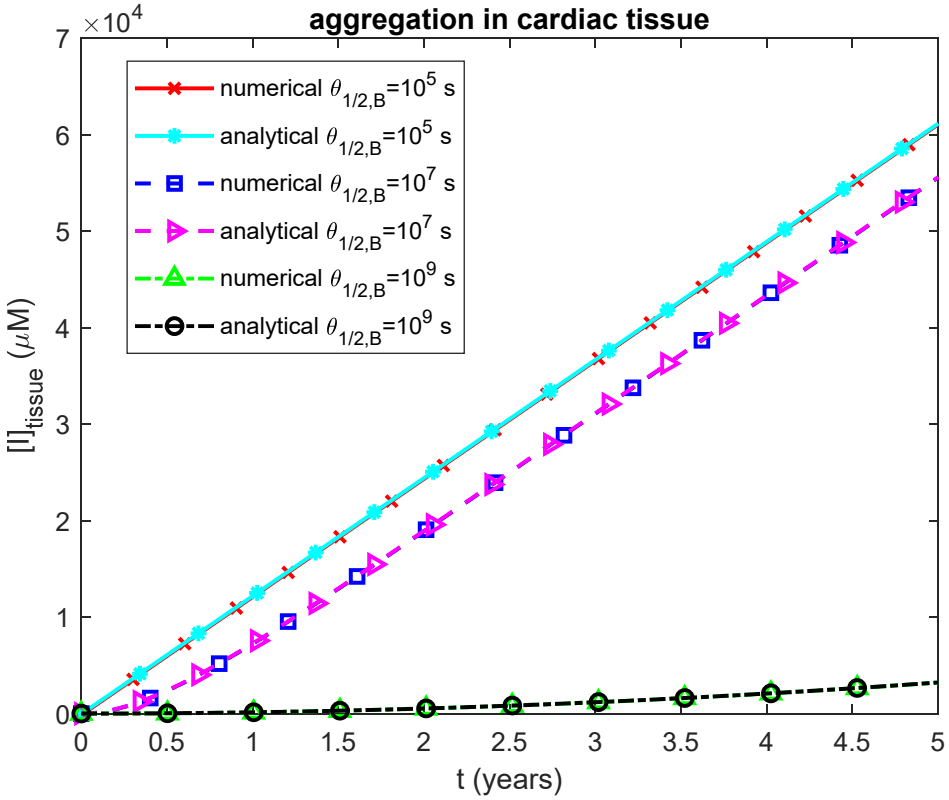
aggregation in cardiac tissue
$\times 10^4$
numerical $\theta_{1/2,B}$=10^5 s
analytical $\theta_{1/2,B}$=10^5 s
numerical $\theta_{1/2,B}$=10^7 s
analytical $\theta_{1/2,B}$=10^7 s
numerical $\theta_{1/2,B}$=10^9 s
analytical $\theta_{1/2,B}$=10^9 s
$[I]_{tissue}$ (μM)
t (years)
0
1
2
3
4
5
6
7
0.5
1
1.5
2
2.5
3
3.5
4
4.5
5

Figure 7

(a)

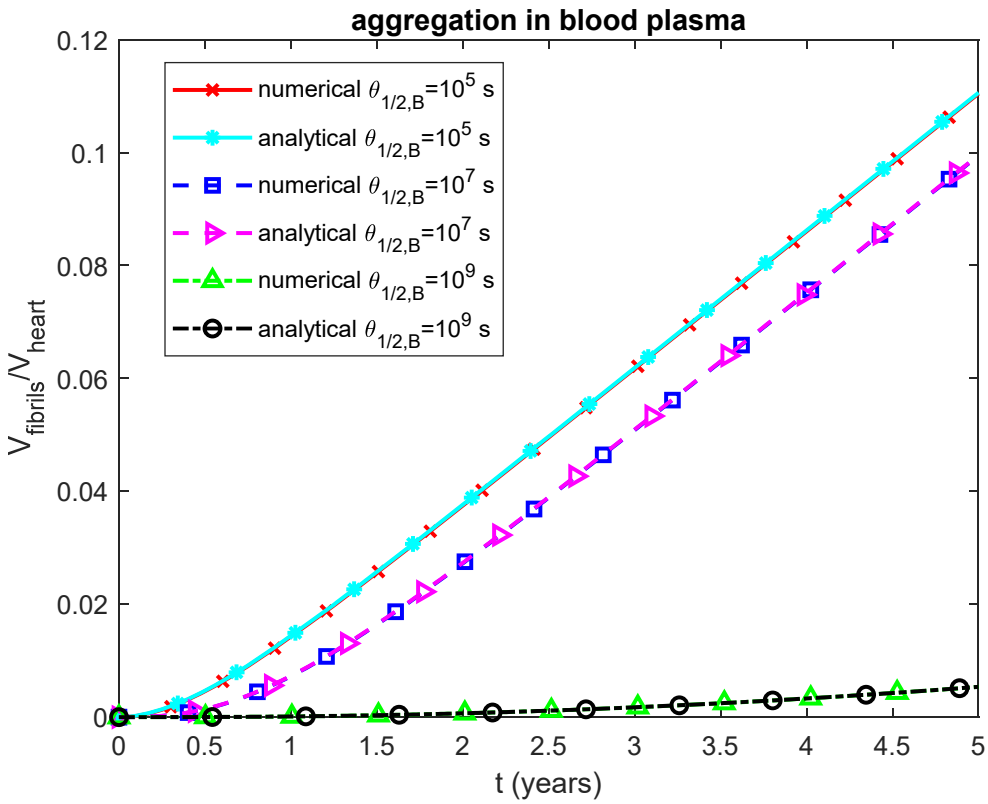
aggregation in blood plasma
numerical $\theta_{1/2,B}=10^5$ s
analytical $\theta_{1/2,B}=10^5$ s
numerical $\theta_{1/2,B}=10^7$ s
analytical $\theta_{1/2,B}=10^7$ s
numerical $\theta_{1/2,B}=10^9$ s
analytical $\theta_{1/2,B}=10^9$ s
$V_{fibrils}/V_{heart}$
t (years)
0
0.02
0.04
0.06
0.08
0.1
0.12
0.5
1
1.5
2
2.5
3
3.5
4
4.5
5

(b)

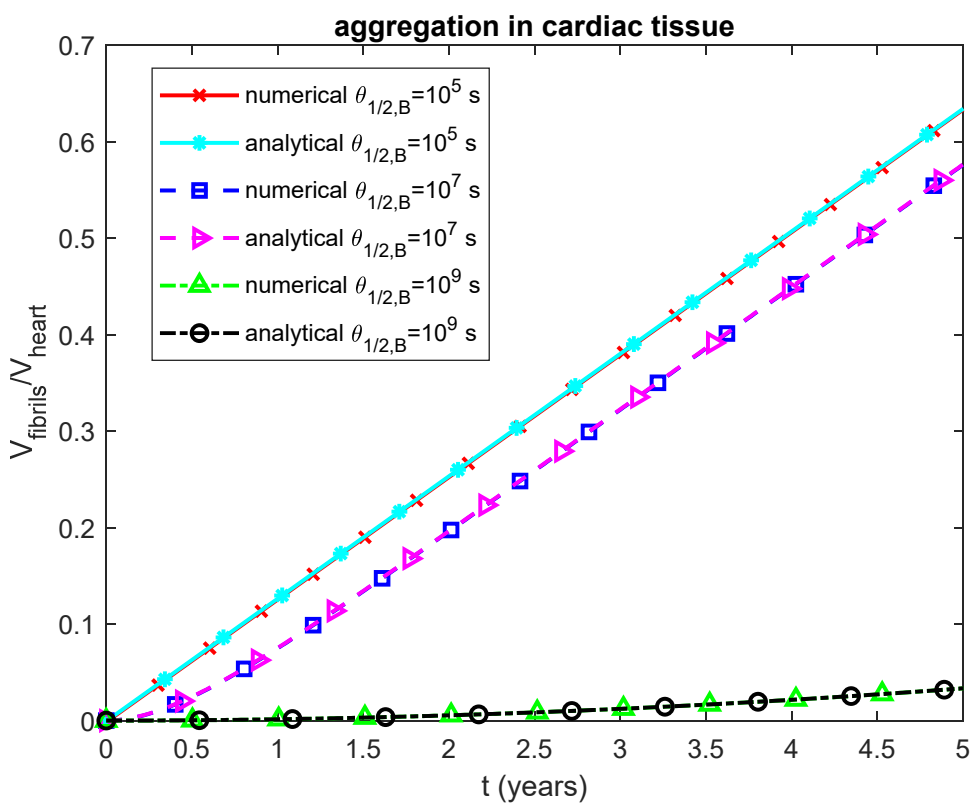
aggregation in cardiac tissue
numerical $\theta_{1/2,B}=10^5$ s
analytical $\theta_{1/2,B}=10^5$ s
numerical $\theta_{1/2,B}=10^7$ s
analytical $\theta_{1/2,B}=10^7$ s
numerical $\theta_{1/2,B}=10^9$ s
analytical $\theta_{1/2,B}=10^9$ s
$V_{fibrils}/V_{heart}$
t (years)
0
0.1
0.2
0.3
0.4
0.5
0.6
0.7
0.5
1
1.5
2
2.5
3
3.5
4
4.5
5

Figure 8

(a)

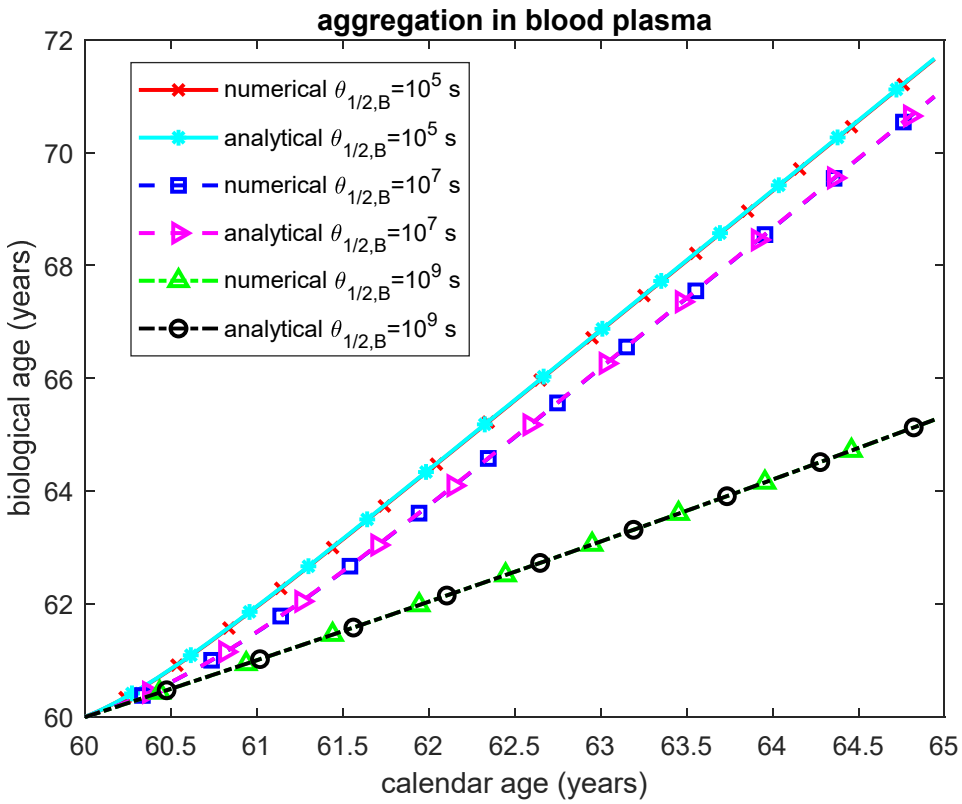
aggregation in blood plasma
numerical $\theta_{1/2,B}$=10^5 s
analytical $\theta_{1/2,B}$=10^5 s
numerical $\theta_{1/2,B}$=10^7 s
analytical $\theta_{1/2,B}$=10^7 s
numerical $\theta_{1/2,B}$=10^9 s
analytical $\theta_{1/2,B}$=10^9 s
biological age (years)
calendar age (years)
60
62
64
66
68
70
72
60
60.5
61
61.5
62
62.5
63
63.5
64
64.5
65

(b)

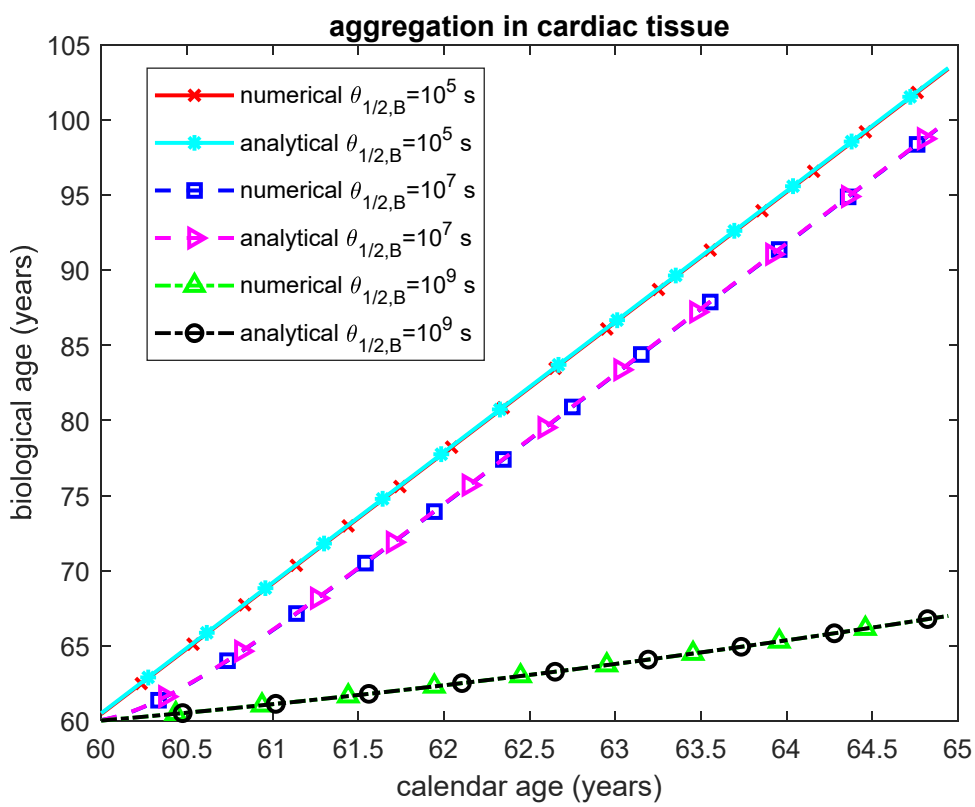
aggregation in cardiac tissue
numerical $\theta_{1/2,B}$=10^5 s
analytical $\theta_{1/2,B}$=10^5 s
numerical $\theta_{1/2,B}$=10^7 s
analytical $\theta_{1/2,B}$=10^7 s
numerical $\theta_{1/2,B}$=10^9 s
analytical $\theta_{1/2,B}$=10^9 s
biological age (years)
calendar age (years)
60
65
70
75
80
85
90
95
100
105
60
60.5
61
61.5
62
62.5
63
63.5
64
64.5
65

Figure 9

(a)

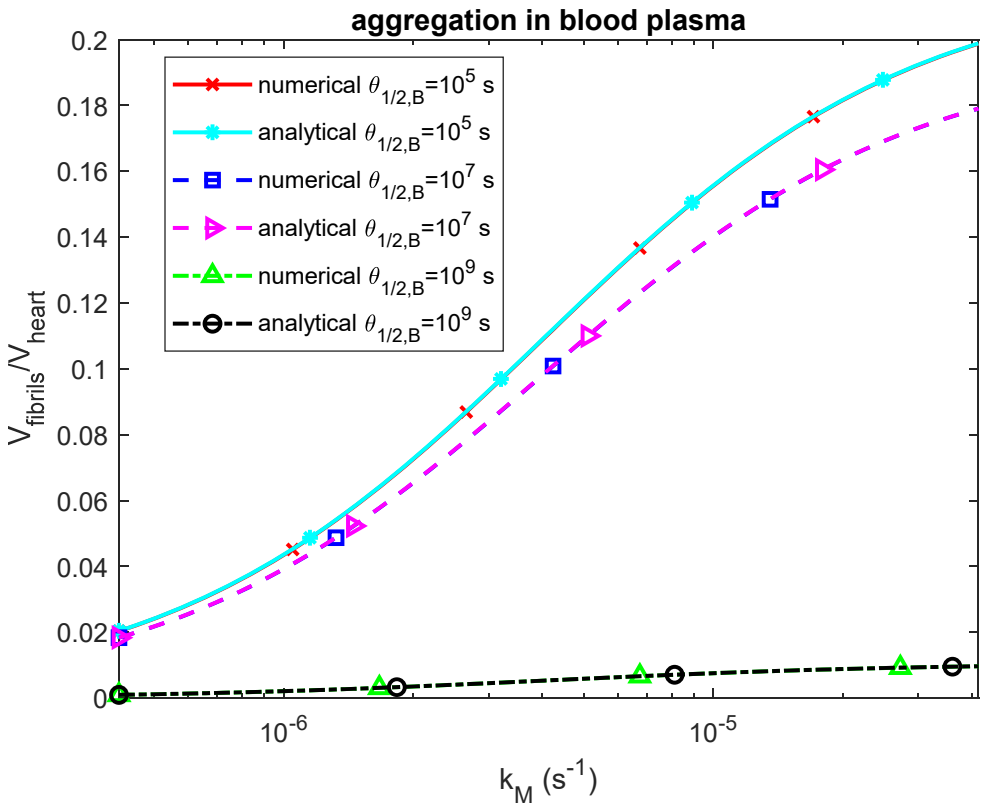
aggregation in blood plasma
numerical $\theta_{1/2,B}=10^5$ s
analytical $\theta_{1/2,B}=10^5$ s
numerical $\theta_{1/2,B}=10^7$ s
analytical $\theta_{1/2,B}=10^7$ s
numerical $\theta_{1/2,B}=10^9$ s
analytical $\theta_{1/2,B}=10^9$ s
$V_{fibrils}/V_{heart}$
0
0.02
0.04
0.06
0.08
0.1
0.12
0.14
0.16
0.18
0.2
10^{-6}
10^{-5}
k_M (s^{-1})

(b)

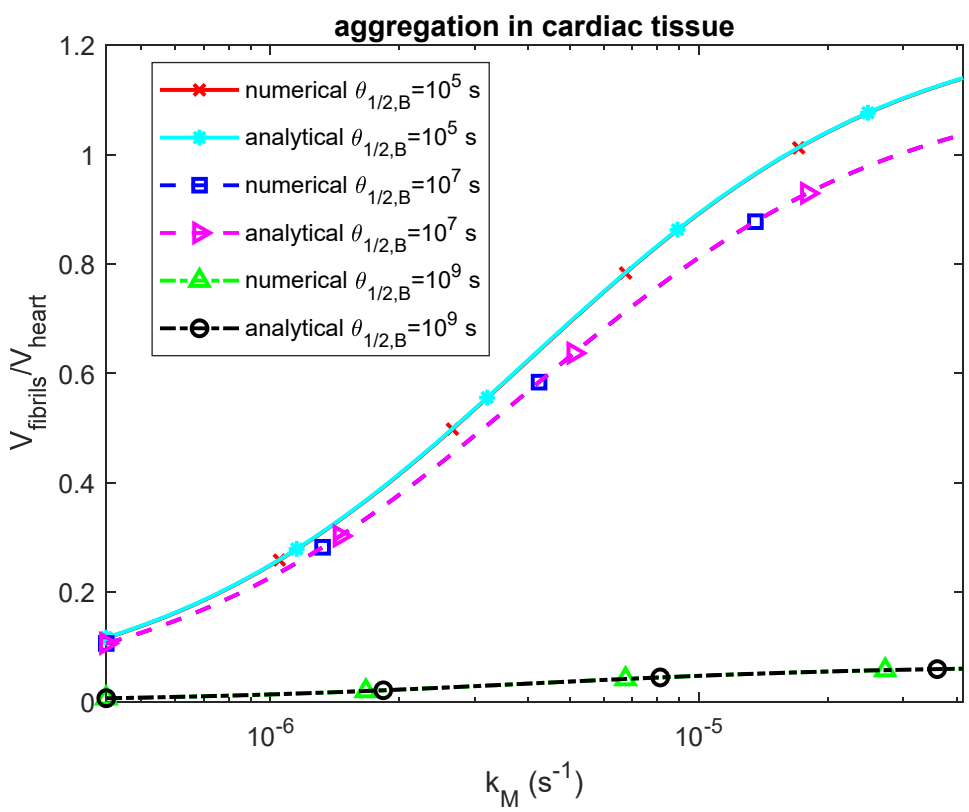
aggregation in cardiac tissue
numerical $\theta_{1/2,B}=10^5$ s
analytical $\theta_{1/2,B}=10^5$ s
numerical $\theta_{1/2,B}=10^7$ s
analytical $\theta_{1/2,B}=10^7$ s
numerical $\theta_{1/2,B}=10^9$ s
analytical $\theta_{1/2,B}=10^9$ s
$V_{fibrils}/V_{heart}$
0
0.2
0.4
0.6
0.8
1
1.2
10^{-6}
10^{-5}
k_M (s^{-1})

Figure 10

(a)

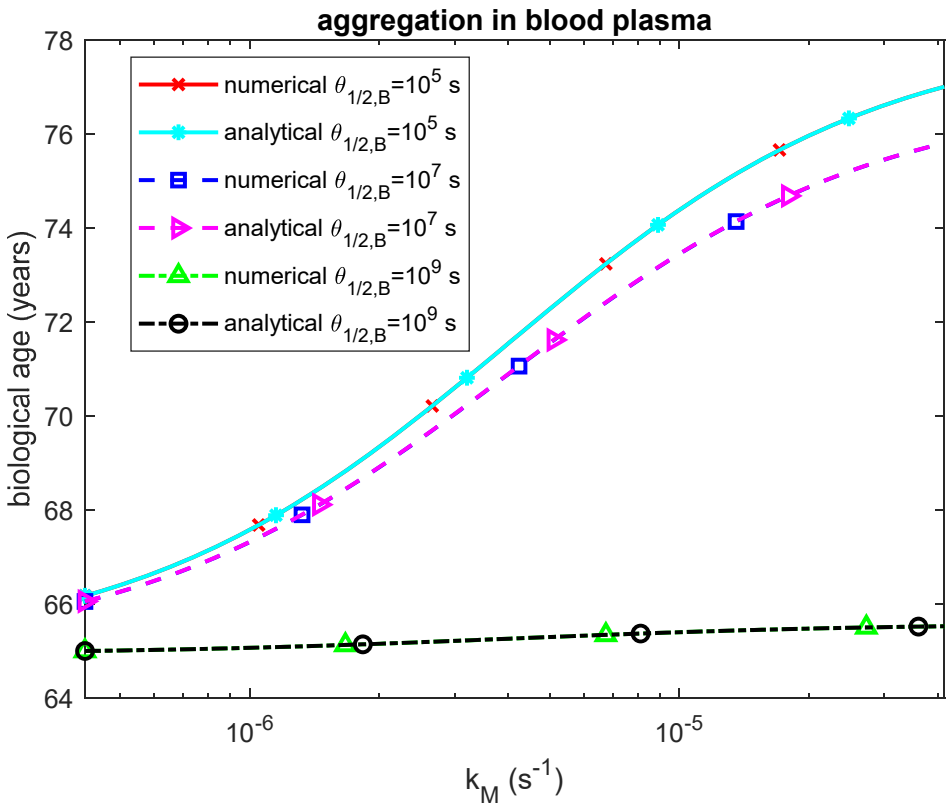
aggregation in blood plasma
numerical $\theta_{1/2,B}=10^5$ s
analytical $\theta_{1/2,B}=10^5$ s
numerical $\theta_{1/2,B}=10^7$ s
analytical $\theta_{1/2,B}=10^7$ s
numerical $\theta_{1/2,B}=10^9$ s
analytical $\theta_{1/2,B}=10^9$ s
biological age (years)
k_M (s^{-1})
78
76
74
72
70
68
66
64
10^{-6}
10^{-5}

(b)

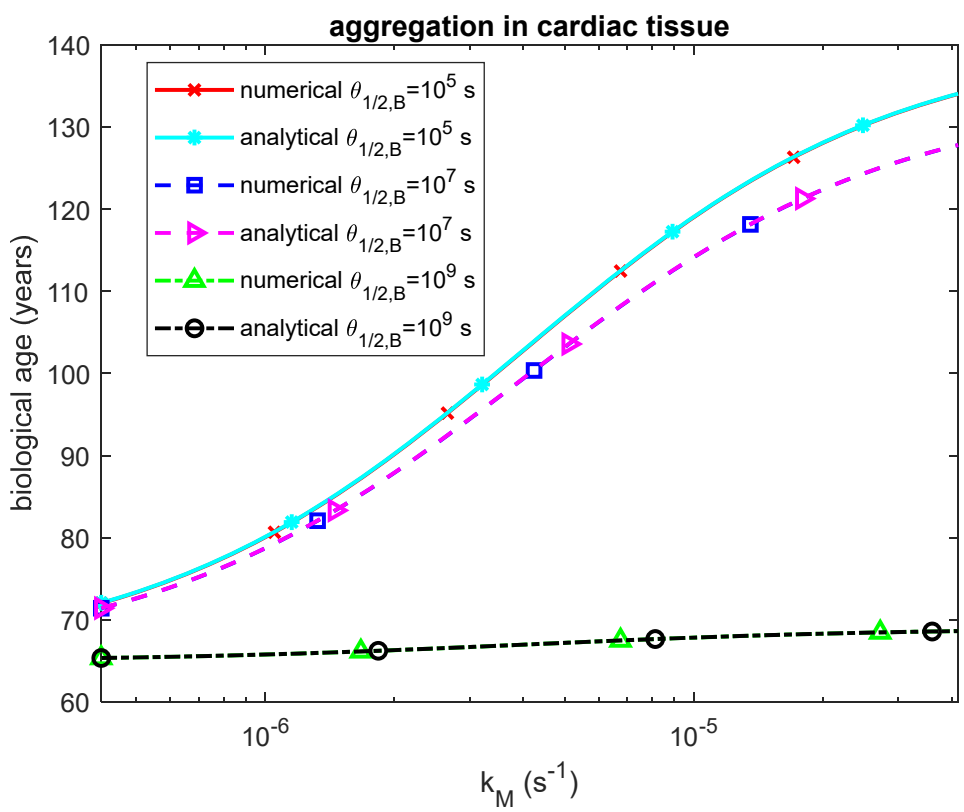
aggregation in cardiac tissue
numerical $\theta_{1/2,B}=10^5$ s
analytical $\theta_{1/2,B}=10^5$ s
numerical $\theta_{1/2,B}=10^7$ s
analytical $\theta_{1/2,B}=10^7$ s
numerical $\theta_{1/2,B}=10^9$ s
analytical $\theta_{1/2,B}=10^9$ s
biological age (years)
k_M (s^{-1})
140
130
120
110
100
90
80
70
60
10^{-6}
10^{-5}

Figure 11

(a)

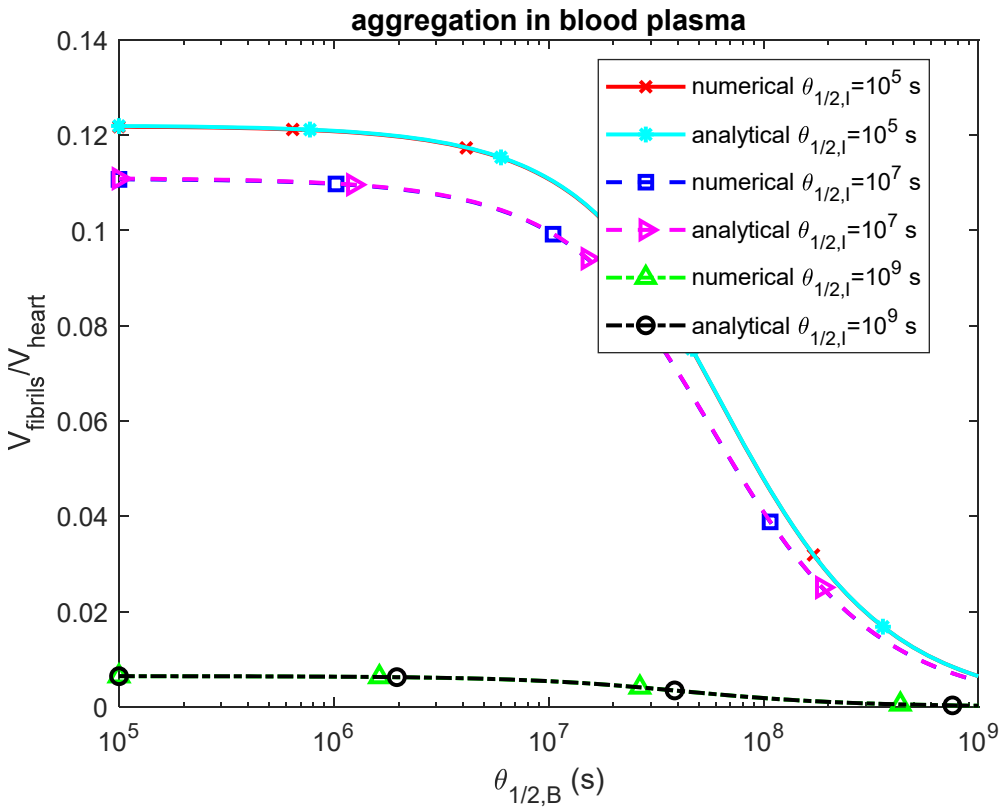
aggregation in blood plasma
numerical $\theta_{1/2,I}$=10^5 s
analytical $\theta_{1/2,I}$=10^5 s
numerical $\theta_{1/2,I}$=10^7 s
analytical $\theta_{1/2,I}$=10^7 s
numerical $\theta_{1/2,I}$=10^9 s
analytical $\theta_{1/2,I}$=10^9 s
$V_{fibrils}/V_{heart}$
$\theta_{1/2,B}$ (s)

(b)

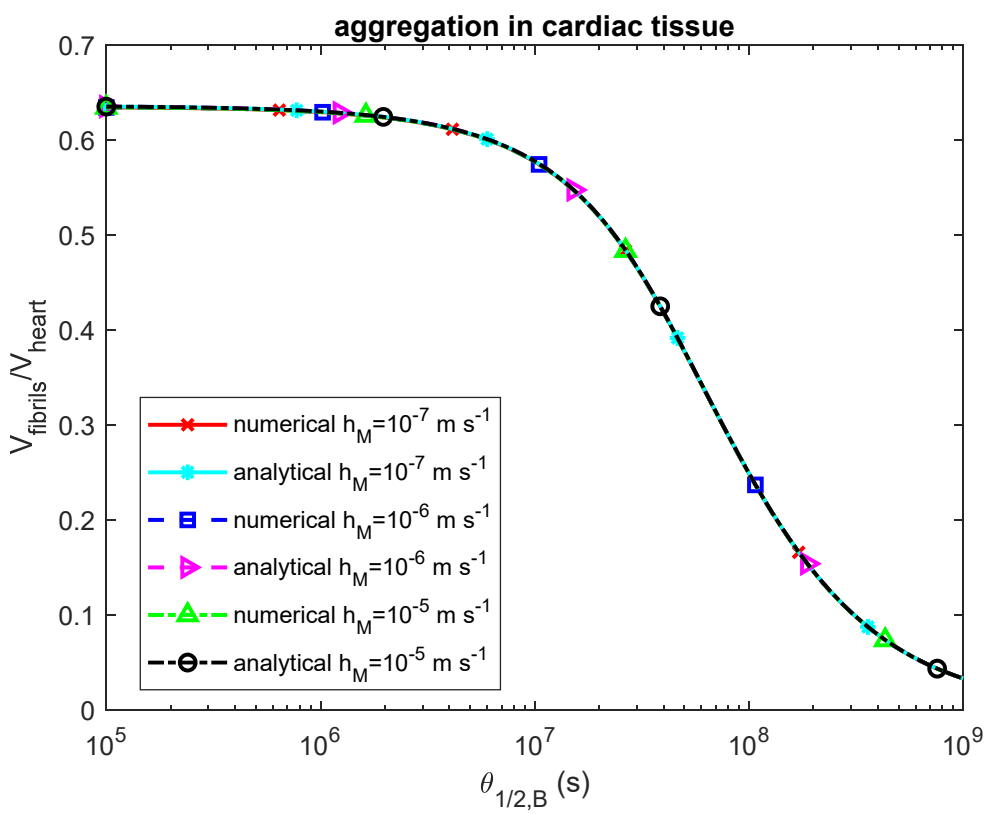
aggregation in cardiac tissue
numerical h_M=10^{-7} m s^{-1}
analytical h_M=10^{-7} m s^{-1}
numerical h_M=10^{-6} m s^{-1}
analytical h_M=10^{-6} m s^{-1}
numerical h_M=10^{-5} m s^{-1}
analytical h_M=10^{-5} m s^{-1}
$V_{fibrils}/V_{heart}$
$\theta_{1/2,B}$ (s)

Figure 12

(a)

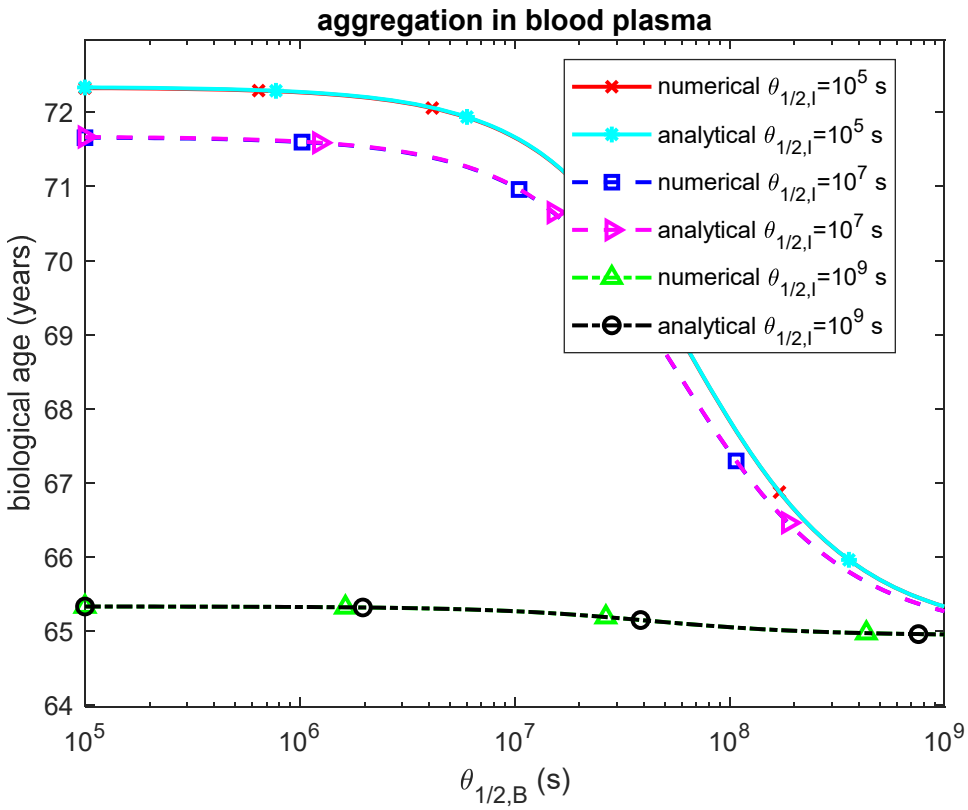
aggregation in blood plasma
numerical $\theta_{1/2,I}$=10^5 s
analytical $\theta_{1/2,I}$=10^5 s
numerical $\theta_{1/2,I}$=10^7 s
analytical $\theta_{1/2,I}$=10^7 s
numerical $\theta_{1/2,I}$=10^9 s
analytical $\theta_{1/2,I}$=10^9 s
biological age (years)
$\theta_{1/2,B}$ (s)

(b)

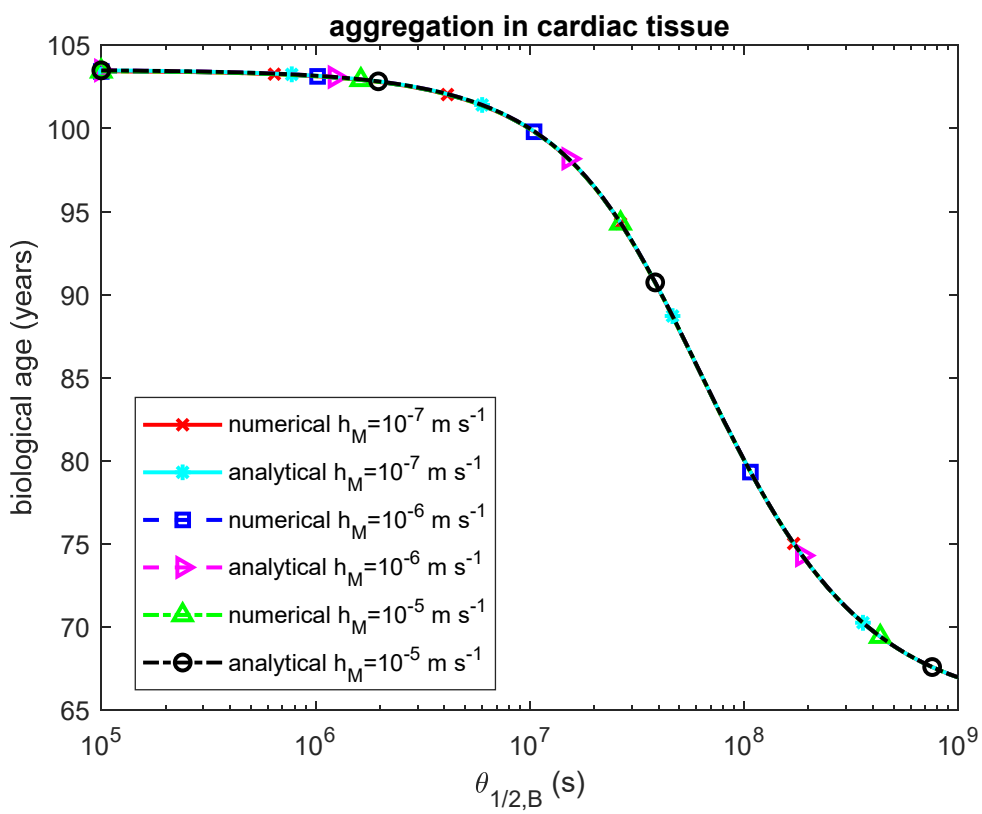
aggregation in cardiac tissue
numerical h_M=10^{-7} m s^{-1}
analytical h_M=10^{-7} m s^{-1}
numerical h_M=10^{-6} m s^{-1}
analytical h_M=10^{-6} m s^{-1}
numerical h_M=10^{-5} m s^{-1}
analytical h_M=10^{-5} m s^{-1}
biological age (years)
$\theta_{1/2,B}$ (s)

Figure 13

(a)

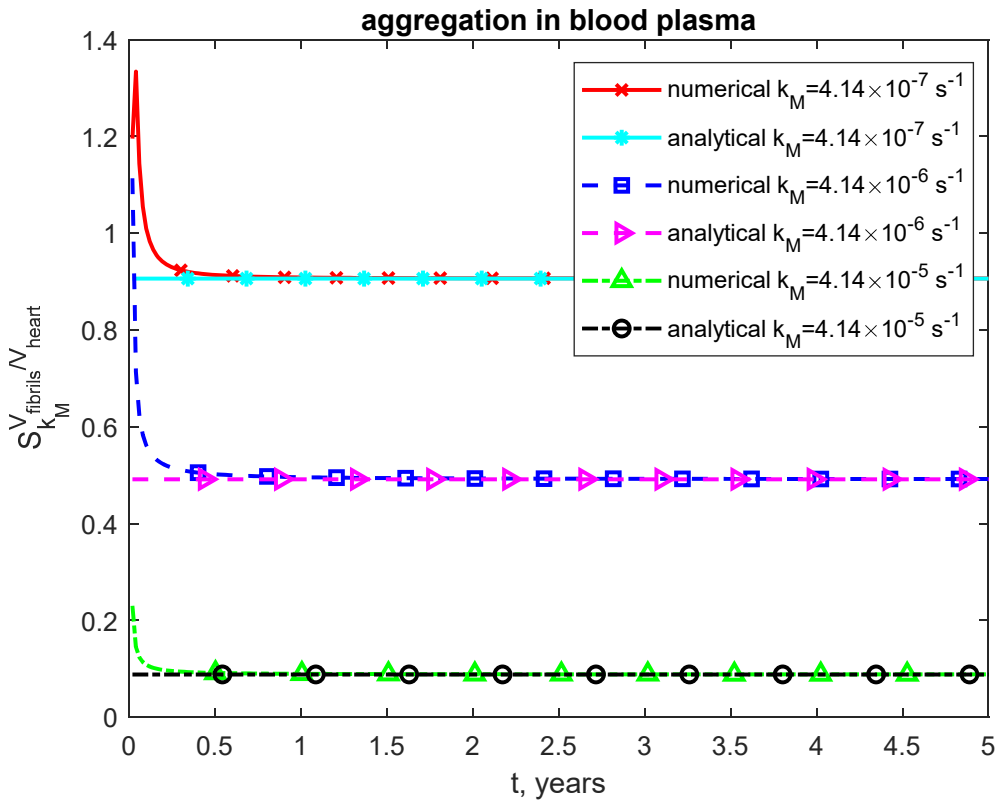
aggregation in blood plasma
numerical k_M=4.14×10^{-7} s^{-1}
analytical k_M=4.14×10^{-7} s^{-1}
numerical k_M=4.14×10^{-6} s^{-1}
analytical k_M=4.14×10^{-6} s^{-1}
numerical k_M=4.14×10^{-5} s^{-1}
analytical k_M=4.14×10^{-5} s^{-1}
$S^{V_{fibrils}/V_{heart}}_{k_M}$
t, years

(b)

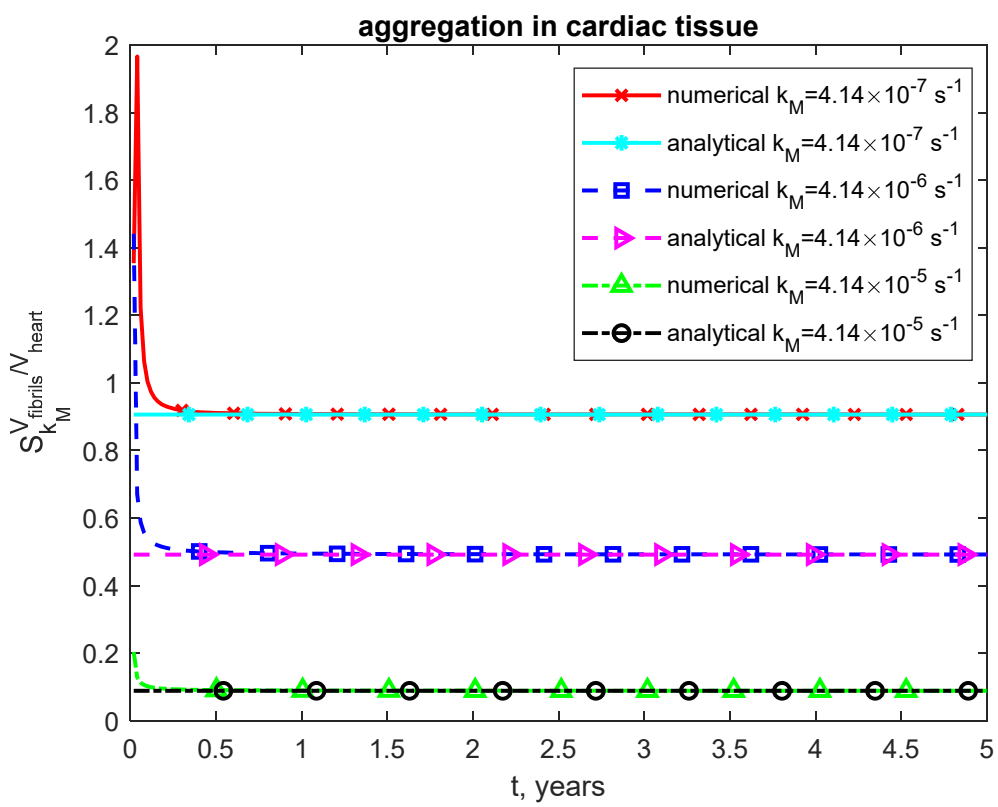
aggregation in cardiac tissue
numerical k_M=4.14×10^{-7} s^{-1}
analytical k_M=4.14×10^{-7} s^{-1}
numerical k_M=4.14×10^{-6} s^{-1}
analytical k_M=4.14×10^{-6} s^{-1}
numerical k_M=4.14×10^{-5} s^{-1}
analytical k_M=4.14×10^{-5} s^{-1}
$S^{V_{fibrils}/V_{heart}}_{k_M}$
t, years

Figure 14

(a)

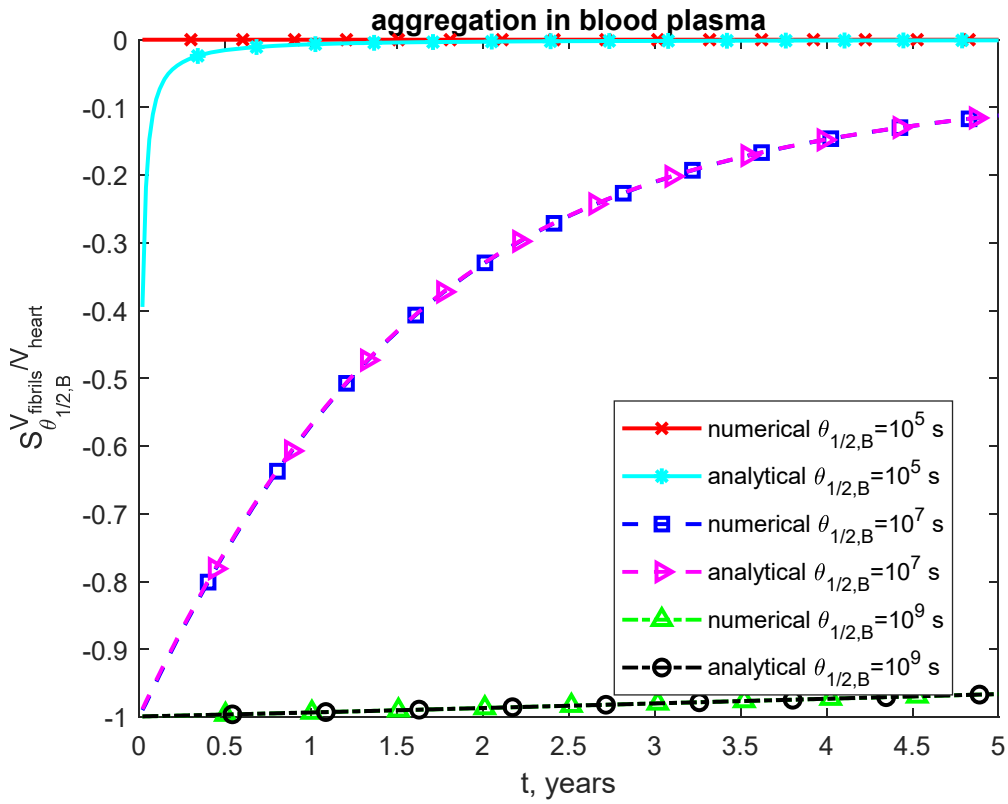
aggregation in blood plasma
$S^{V_{fibrils}/V_{heart}}_{\theta_{1/2,B}}$
t, years
numerical $\theta_{1/2,B}=10^5$ s
analytical $\theta_{1/2,B}=10^5$ s
numerical $\theta_{1/2,B}=10^7$ s
analytical $\theta_{1/2,B}=10^7$ s
numerical $\theta_{1/2,B}=10^9$ s
analytical $\theta_{1/2,B}=10^9$ s

(b)

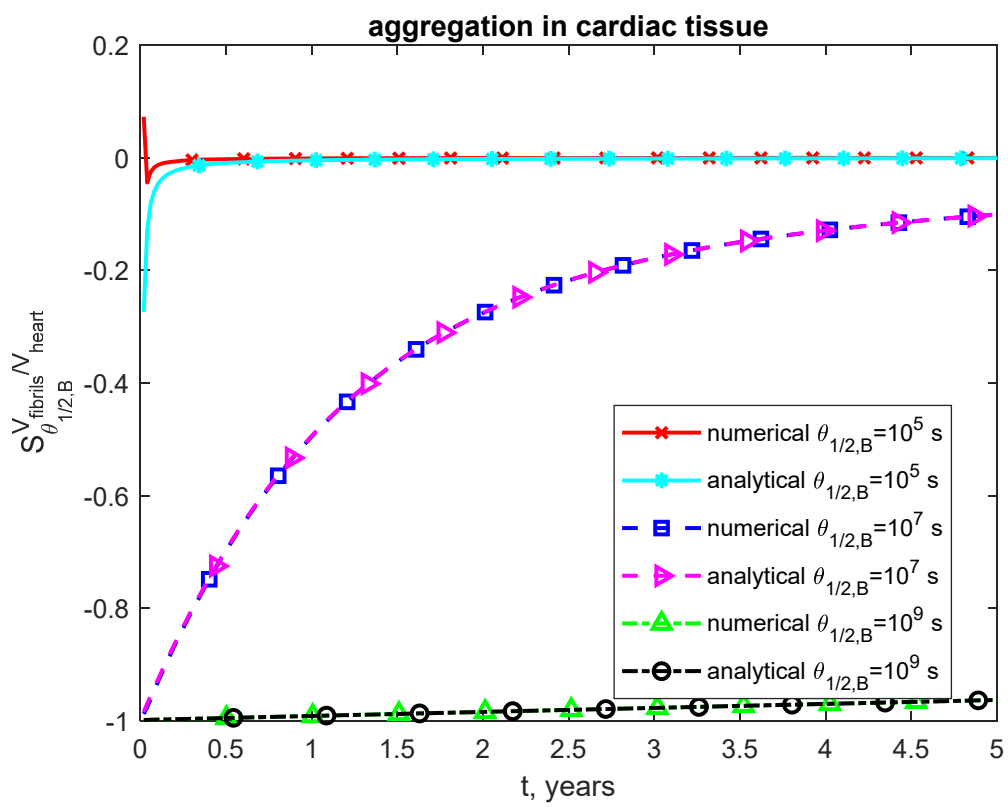
aggregation in cardiac tissue
$S^{V_{fibrils}/V_{heart}}_{\theta_{1/2,B}}$
t, years
numerical $\theta_{1/2,B}=10^5$ s
analytical $\theta_{1/2,B}=10^5$ s
numerical $\theta_{1/2,B}=10^7$ s
analytical $\theta_{1/2,B}=10^7$ s
numerical $\theta_{1/2,B}=10^9$ s
analytical $\theta_{1/2,B}=10^9$ s

Figure 15

Does Human Transthyretin Aggregate in Blood Plasma or in Cardiac Tissue? A Mathematical Modeling Study

Andrey V Kuznetsov

Department of Mechanical and Aerospace Engineering, North Carolina State University,

Raleigh, NC 27695-7910, USA; e-mail: avkuznet@ncsu.edu

Supplemental Materials

S1. Numerical solution

The systems of differential equations were solved numerically using MATLAB's ODE45 solver (R2024a, MathWorks, Natick, MA, USA). For scenario 1, Eqs. (2), (8)–(10), and (12) with initial conditions (3) and (13) were used, while scenario 2 employed Eqs. (2), (29), and (31)–(33) with initial conditions (3) and (34). ODE45 solver, which uses an adaptive step-size Runge-Kutta method, was selected for its balance of accuracy and computational efficiency. To achieve high numerical precision, both the relative and absolute tolerances were set to 1e-10.

S2. Supplementary figures

(a)

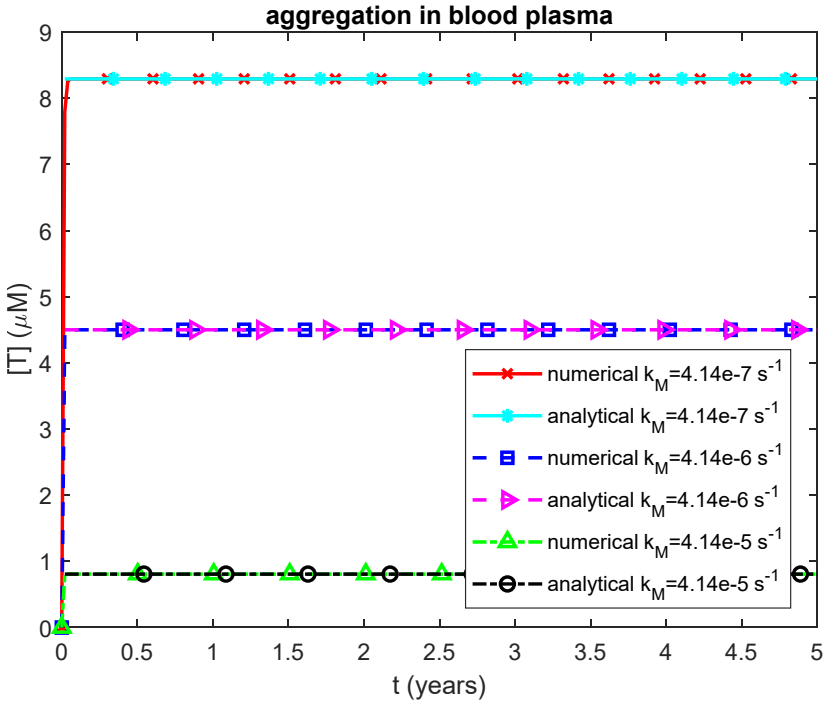

(b)

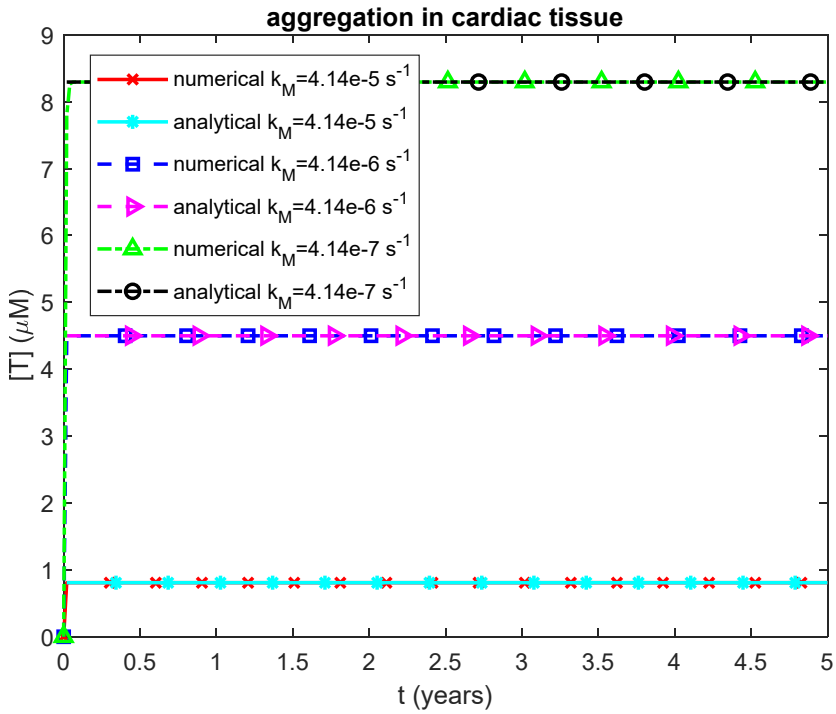

Fig. S1. Molar concentration of TTR tetramers, representing the native form of TTR, in the blood plasma vs time for various values of k_M . (a) Scenario when TTR monomers misfold and assemble into protofibrillar formations within the bloodstream before depositing in the heart. (b) Scenario when TTR

monomers remain in circulation until they directly attach to sites within the heart, where they form amyloid deposits *in situ*.

(a)

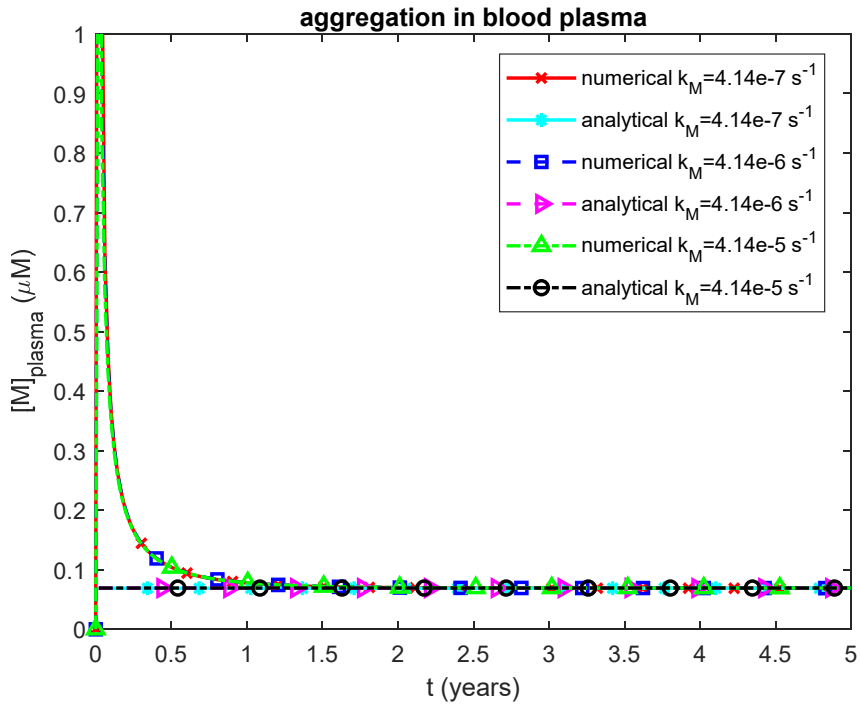

(b)

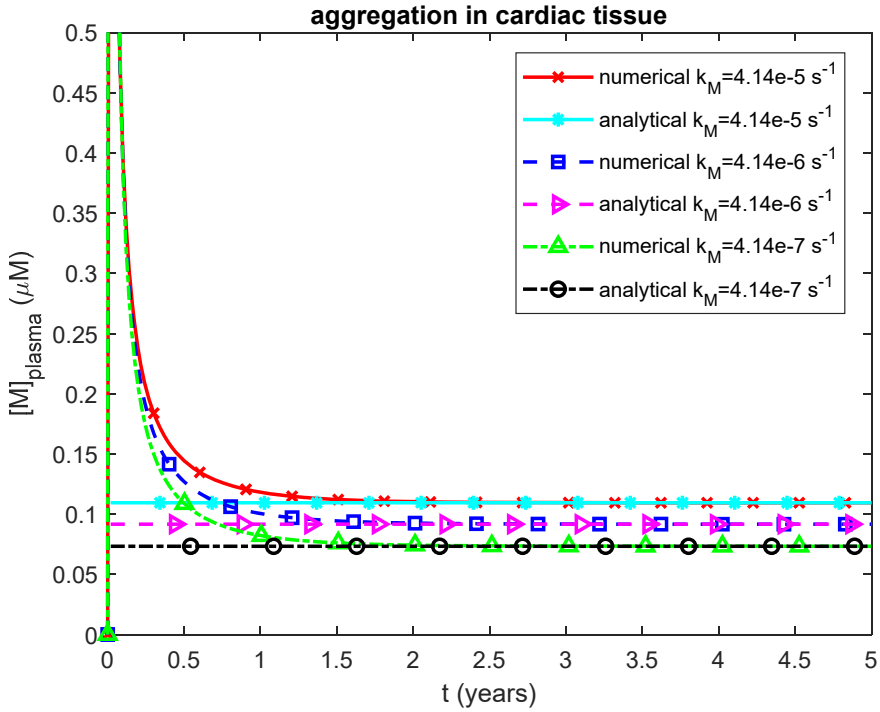

Fig. S2. Molar concentration of TTR monomers in the blood plasma vs time for various values of k_M . (a) Scenario when TTR monomers misfold and assemble into protofibrillar formations within the bloodstream before depositing in the heart; (b) Scenario when TTR monomers remain in circulation until they directly attach to sites within the heart, where they form amyloid deposits *in situ*.

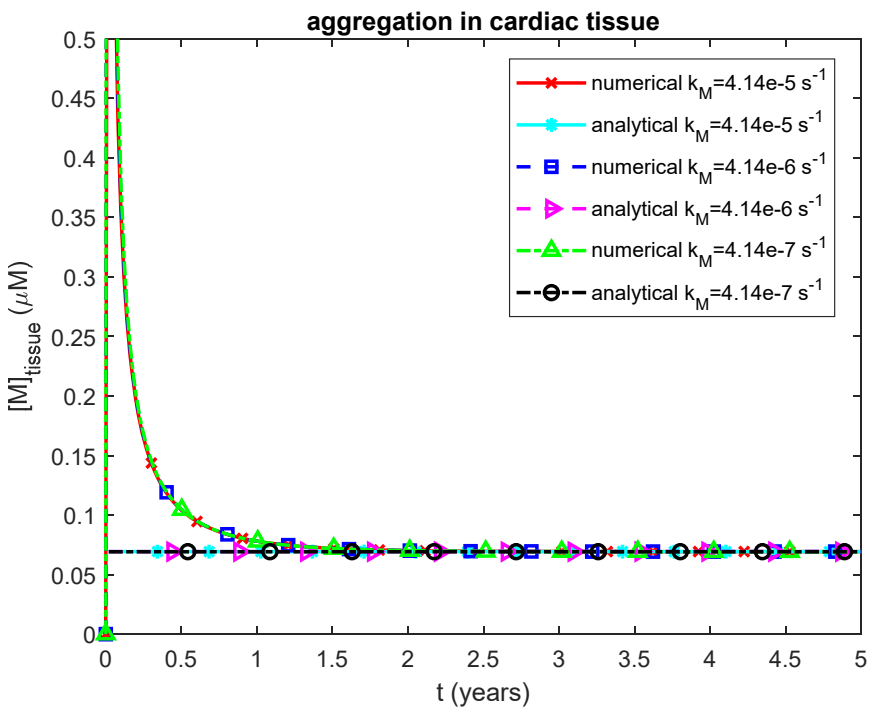

Fig. S3. Molar concentration of TTR monomers in the cardiac tissue vs time for various values of k_M . Scenario when TTR monomers remain in circulation until they directly attach to sites within the heart, where they form amyloid deposits *in situ*.

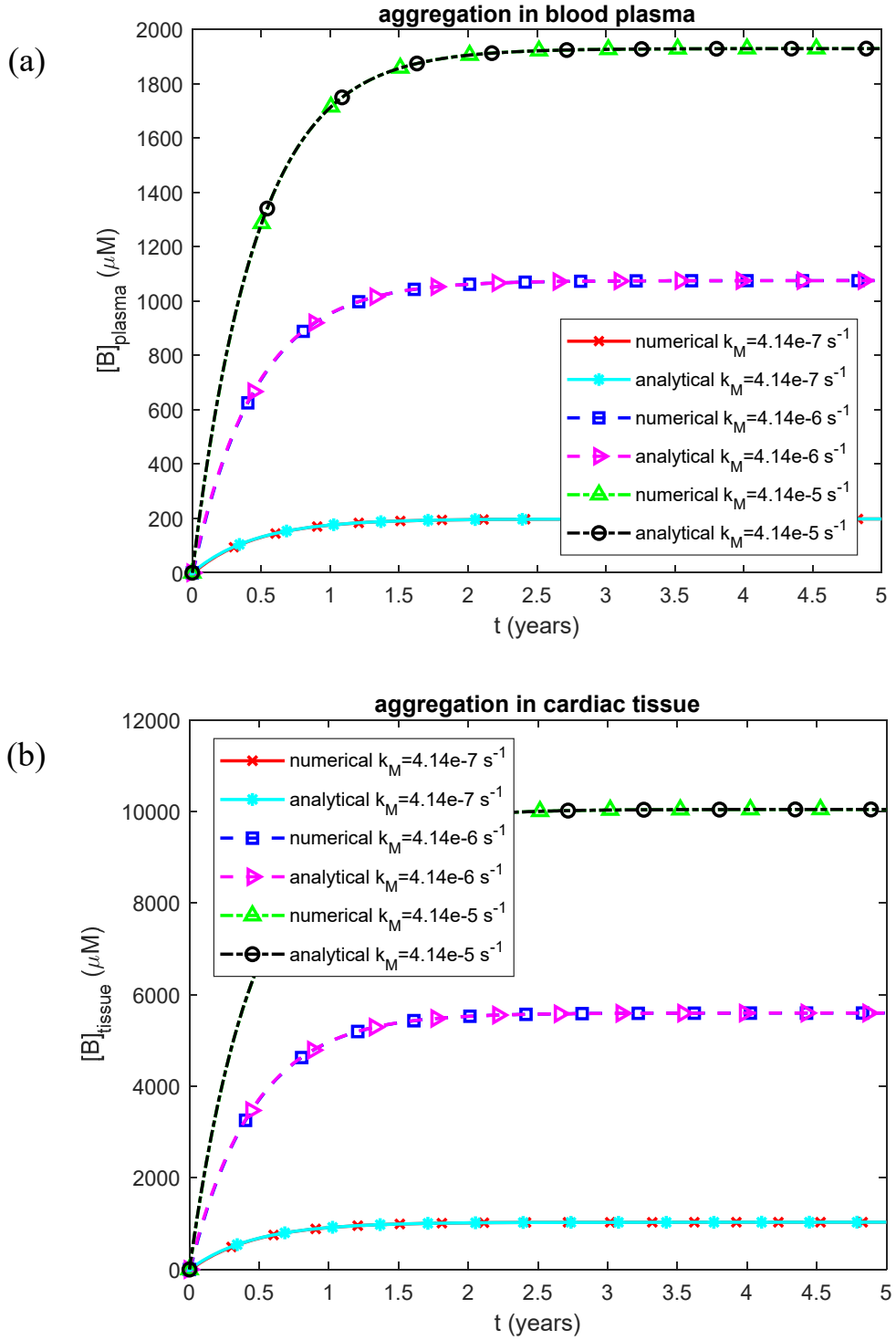

Fig. S4. (a) Molar concentration of free TTR oligomers in the blood plasma vs time for various values of k_M . Scenario when TTR accumulates in blood plasma. (b) Molar concentration of free TTR oligomers in the cardiac tissue vs time for various values of k_M . Scenario when TTR accumulates in cardiac tissue.

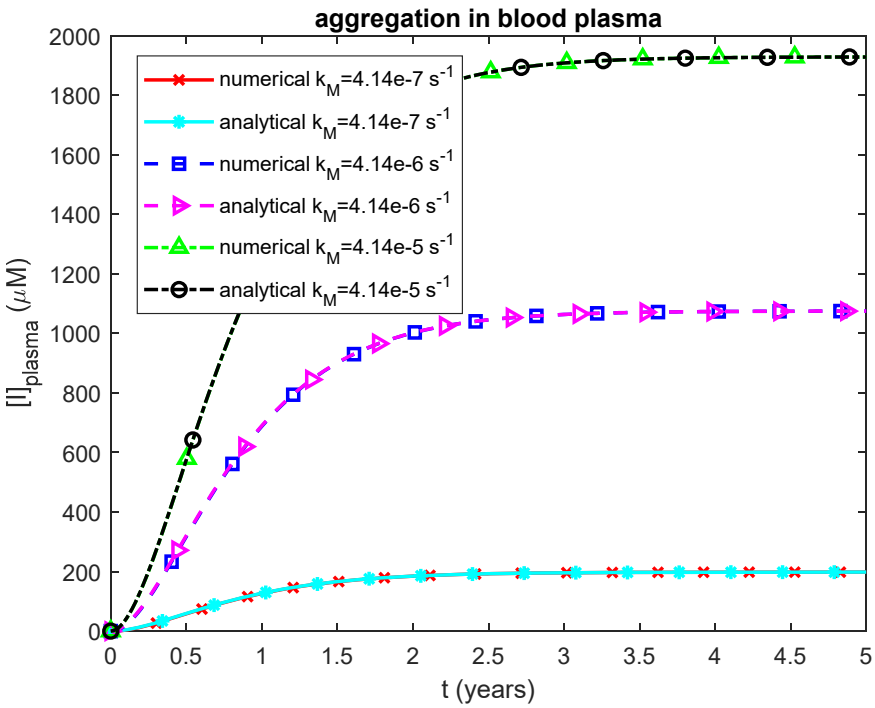

Fig. S5. Molar concentration of TTR oligomers deposited into amyloid protofibrils circulating in the blood plasma vs time for various values of k_M . Scenario when TTR monomers misfold and assemble into protofibrillar formations within the bloodstream before depositing in the heart.

(a)

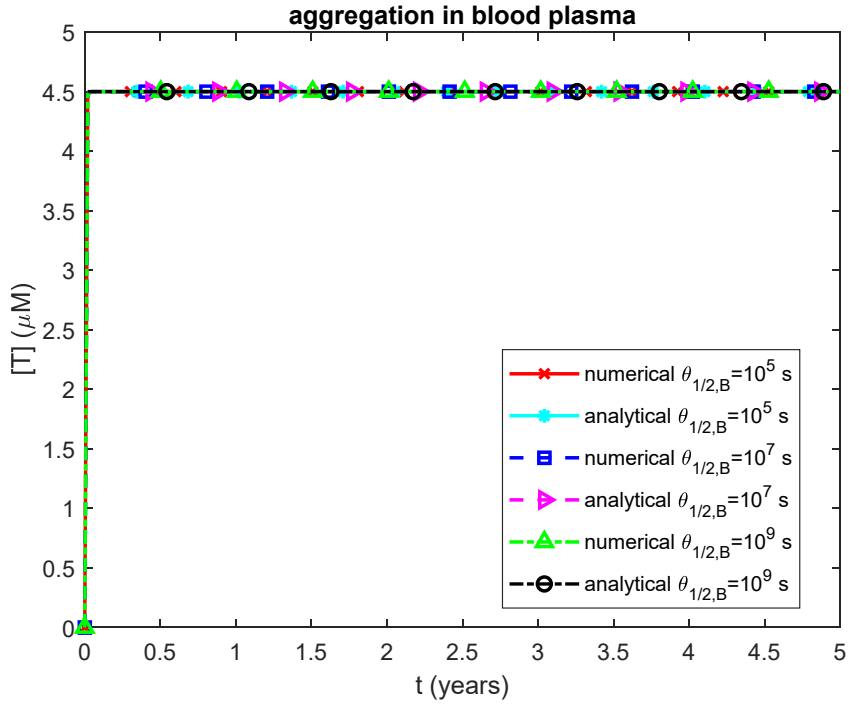

(b)

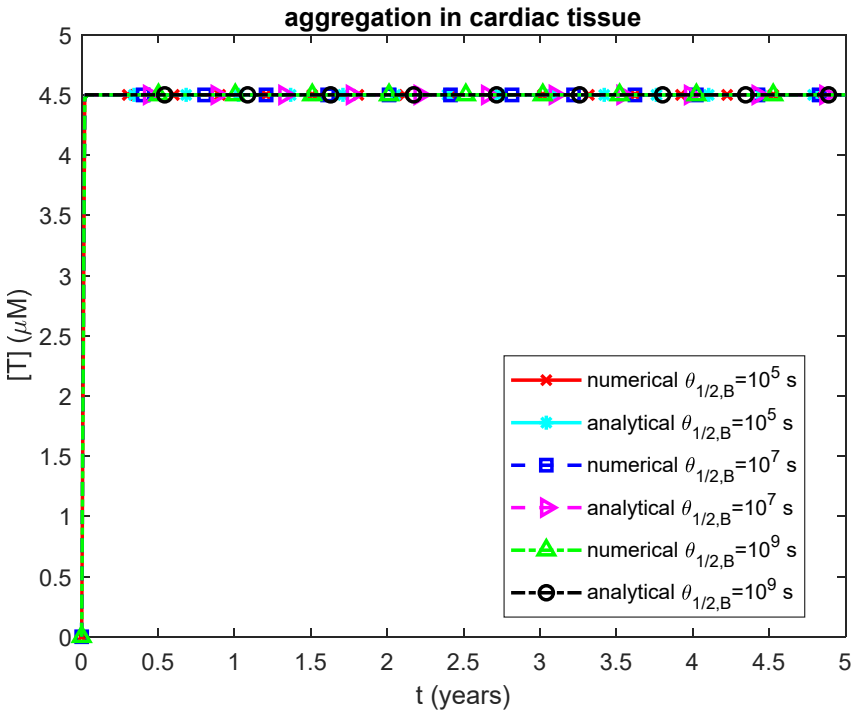

Fig. S6. Molar concentration of TTR tetramers, representing the native form of TTR, in the blood plasma vs time for various values of $\theta_{1/2,B}$. (a) Scenario when TTR monomers misfold and assemble into protofibrillar formations within the bloodstream before depositing in the heart. (b) Scenario when TTR

monomers remain in circulation until they directly attach to sites within the heart, where they form amyloid deposits *in situ*.

(a)

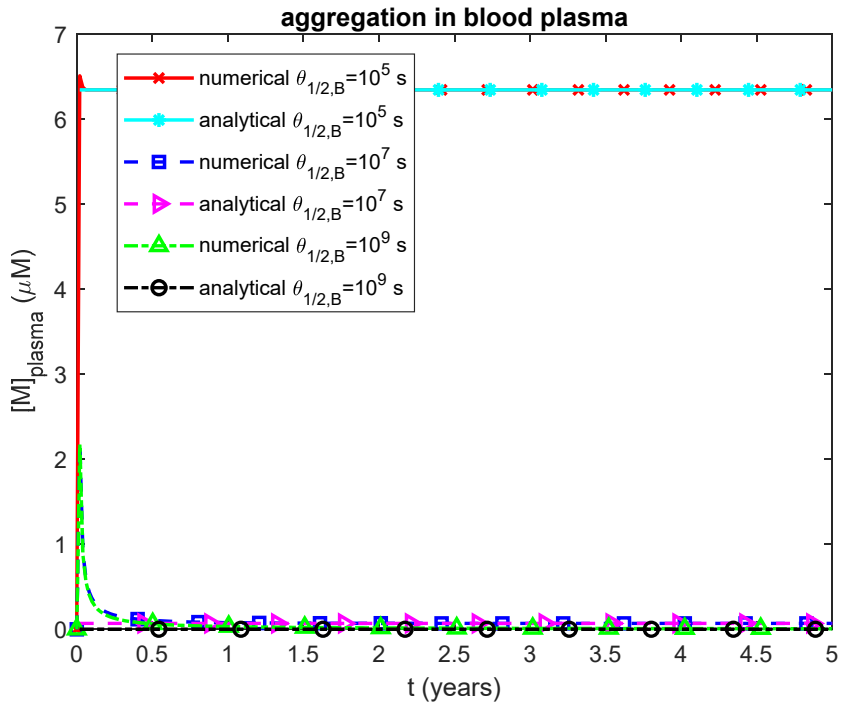

(b)

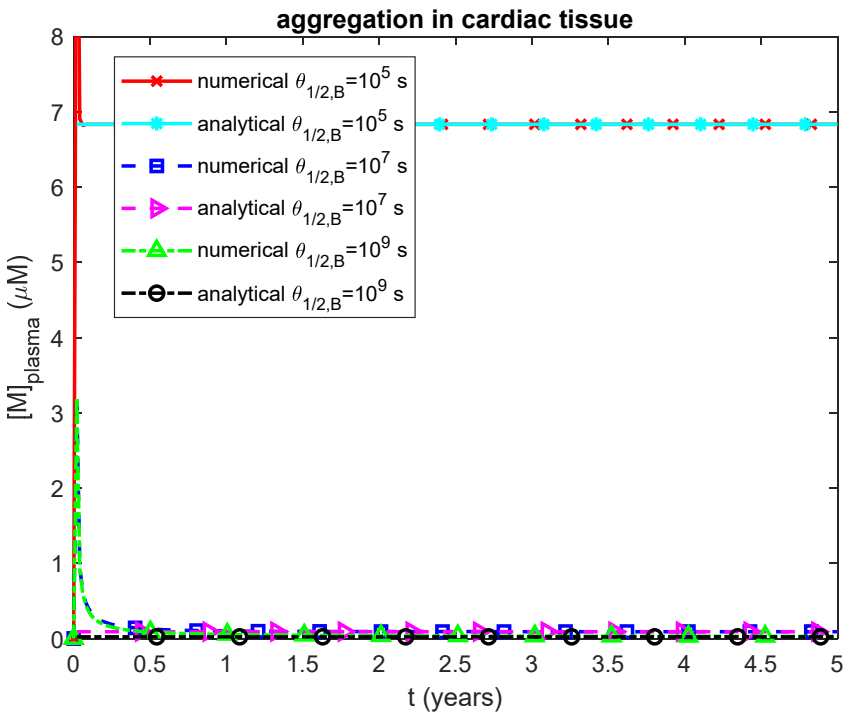

Fig. S7. Molar concentration of TTR monomers in the blood plasma vs time for various values of $\theta_{1/2,B}$. (a) Scenario when TTR monomers misfold and assemble into protofibrillar formations within the bloodstream before depositing in the heart. (b) Scenario when TTR monomers remain in circulation until they directly attach to sites within the heart, where they form amyloid deposits *in situ*.

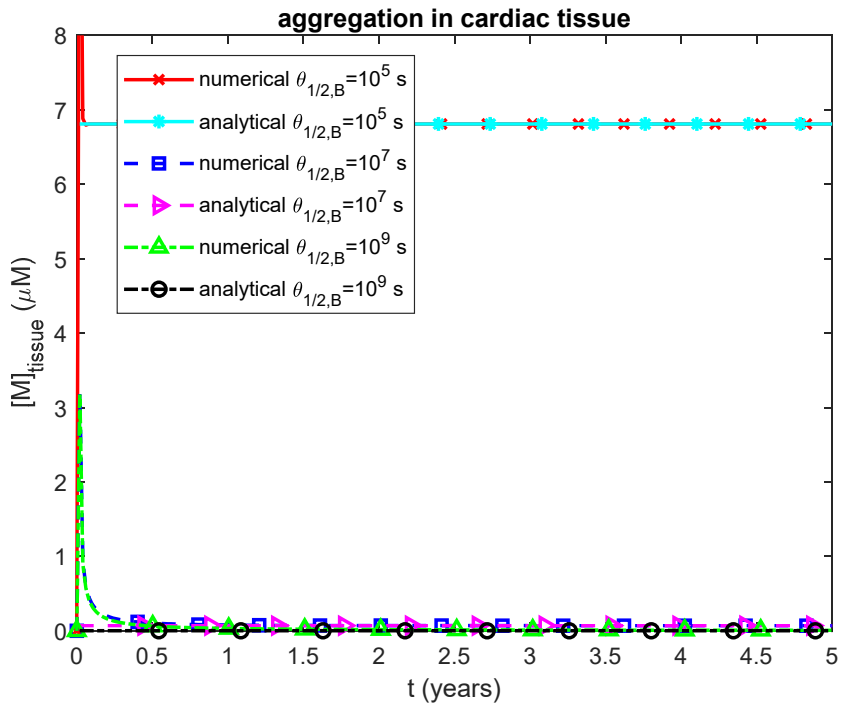

Fig. S8. Molar concentration of TTR monomers in the cardiac tissue vs time for various values of $\theta_{1/2,B}$. Scenario when TTR monomers remain in circulation until they directly attach to sites within the heart, where they form amyloid deposits *in situ*.

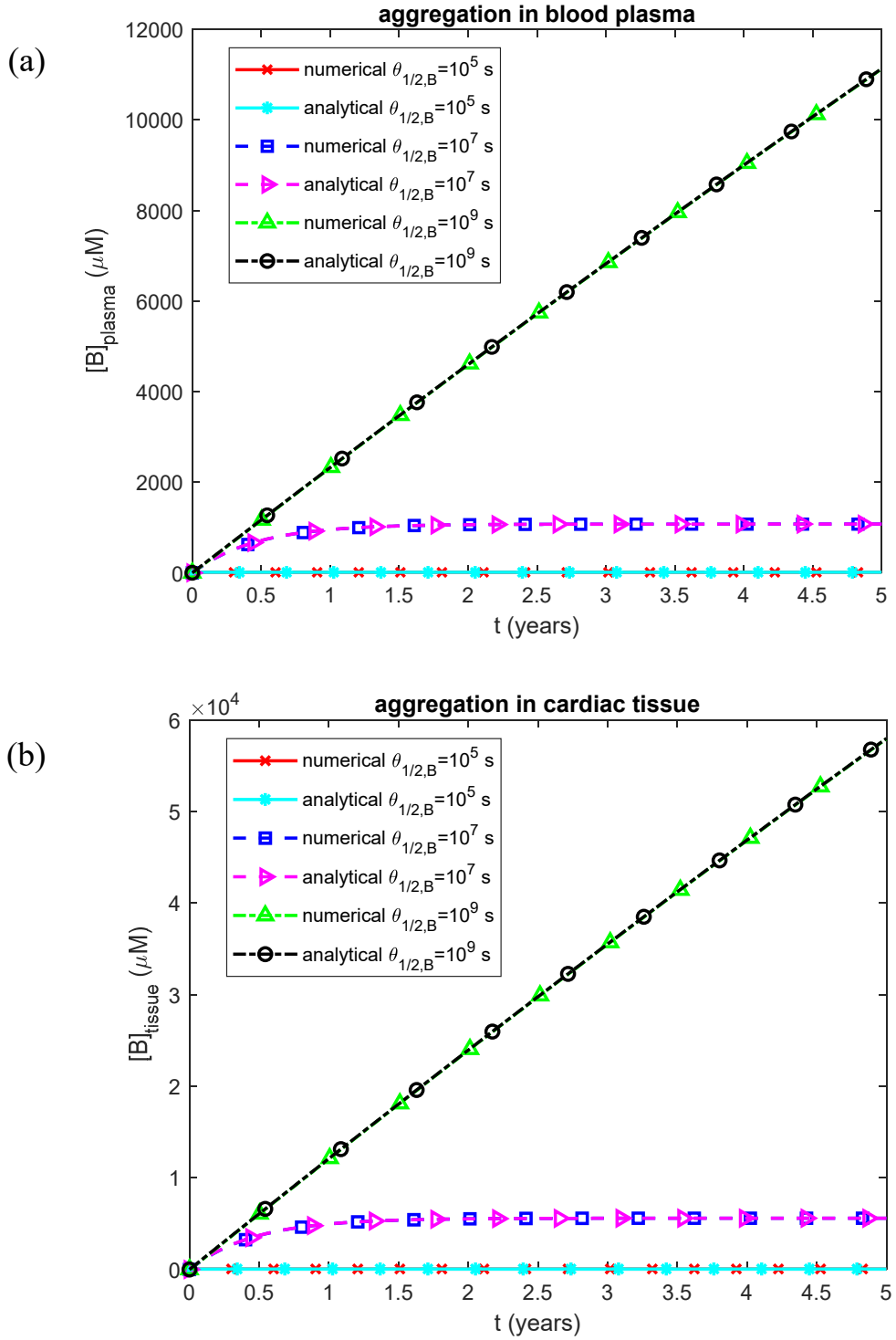

Fig. S9. (a) Molar concentration of free TTR oligomers in the blood plasma vs time for various values of $\theta_{1/2,B}$. Scenario when TTR accumulates in blood plasma. (b) Molar concentration of free TTR oligomers in cardiac tissue. Scenario when TTR accumulates in cardiac tissue.

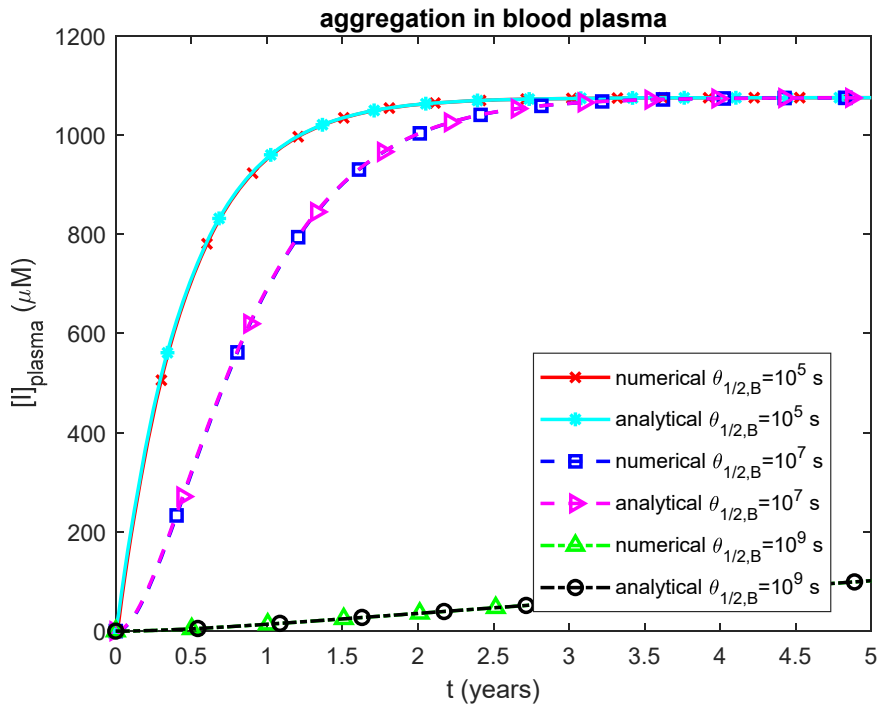

Fig. S10. Molar concentration of TTR oligomers deposited into amyloid protofibrils circulating in the blood plasma vs time for various values of $\theta_{1/2,B}$. Scenario when TTR monomers misfold and assemble into protofibrillar formations within the bloodstream before depositing in the heart.

(a)

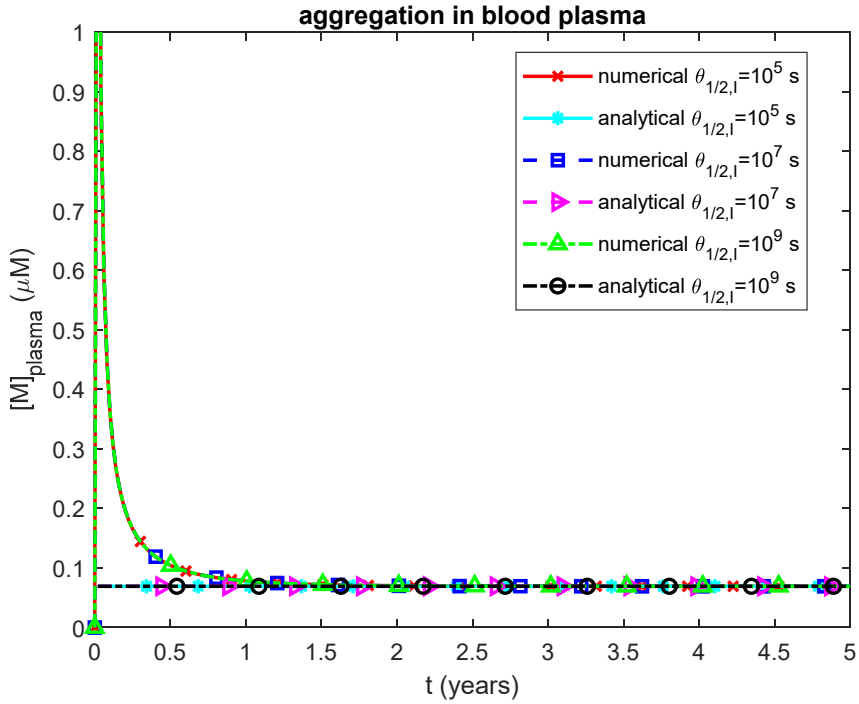

(b)

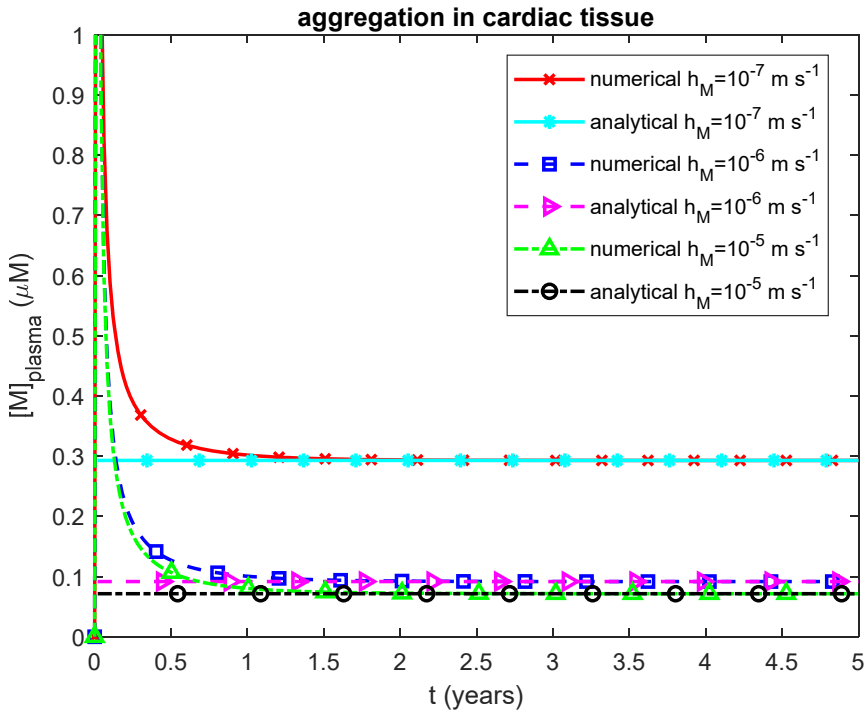

Fig. S11. Molar concentration of TTR monomers in the blood plasma vs time. (a) Scenario when TTR monomers misfold and assemble into protofibrillar formations within the bloodstream before depositing

in the heart for various values of $\theta_{1/2,I}$. (b) Scenario when TTR monomers remain in circulation until they directly attach to sites within the heart, where they form amyloid deposits *in situ* for various values of h_M.

(a)

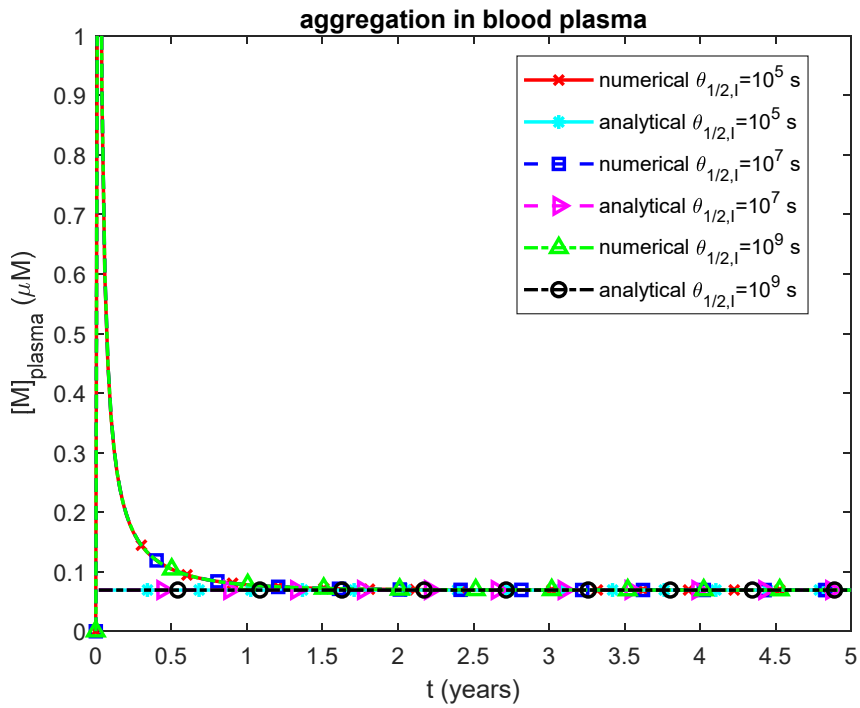

(b)

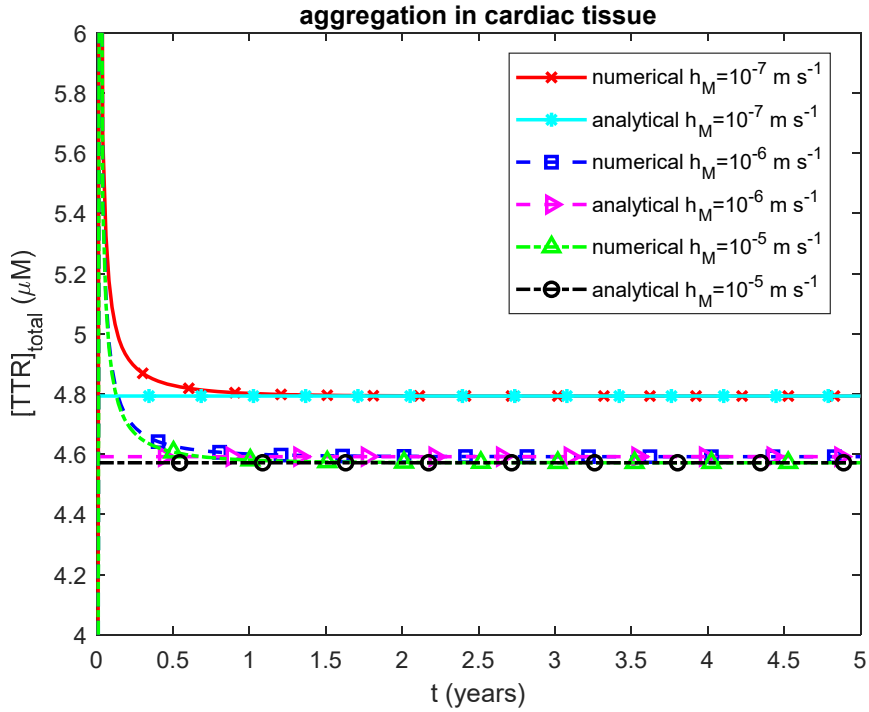

Fig. S12. Total concentration of TTR (in any state) in the blood plasma vs time. (a) Scenario when TTR monomers misfold and assemble into protofibrillar formations within the bloodstream before depositing in the heart for various values of $\theta_{1/2,I}$. (b) Scenario when TTR monomers remain in circulation until they directly attach to sites within the heart, where they form amyloid deposits *in situ* for various values of h_M.

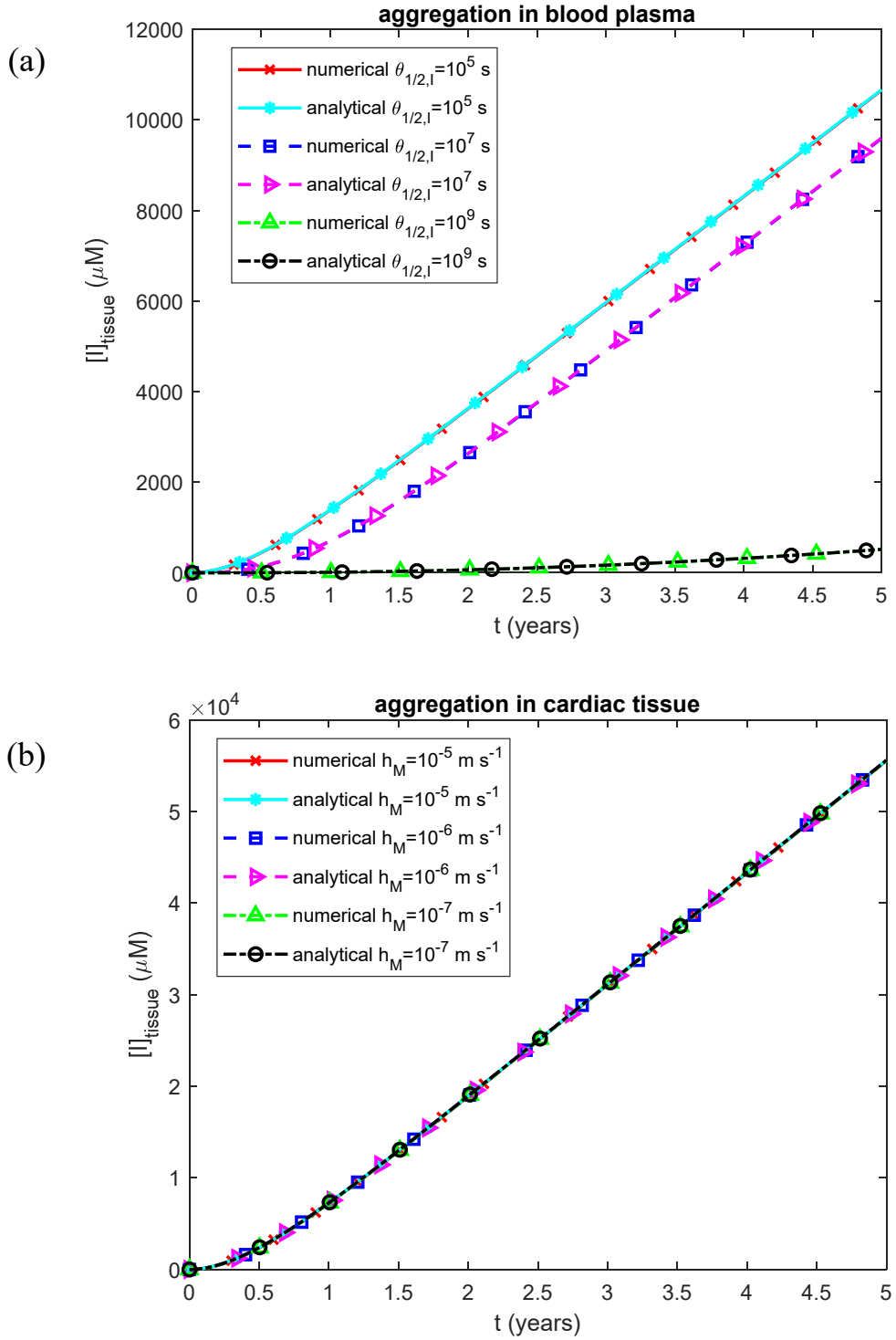

Fig. S13. Molar concentration of TTR oligomers deposited into amyloid fibrils that infiltrated the cardiac tissue vs time. (a) Scenario when TTR monomers misfold and assemble into protofibrillar formations within the bloodstream before depositing in the heart for various values of $\theta_{1/2,I}$. (b) Scenario when TTR

monomers remain in circulation until they directly attach to sites within the heart, where they form amyloid deposits *in situ* for various values of h_M .

(a)

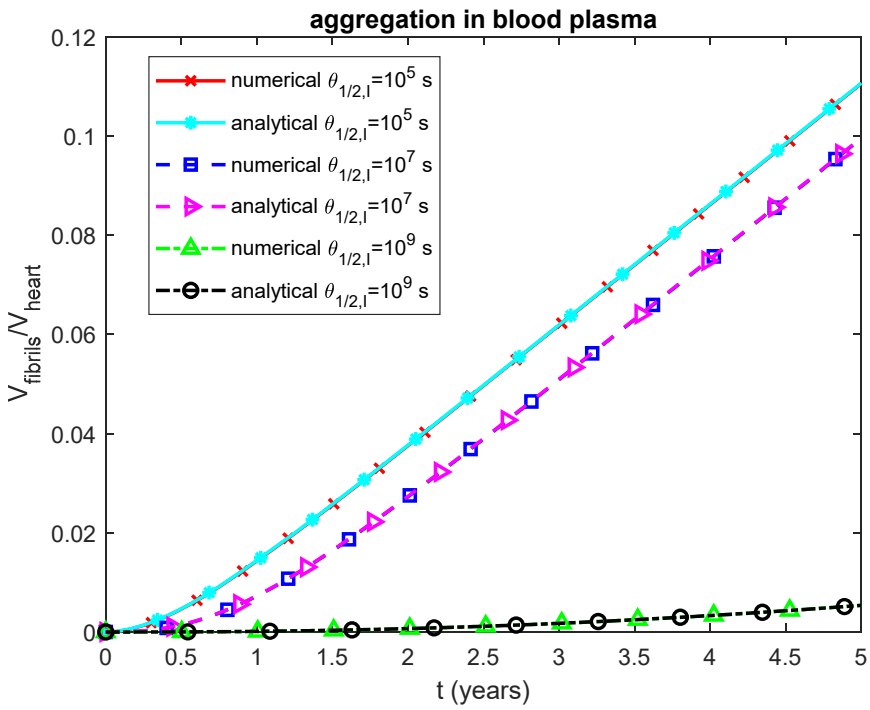

(b)

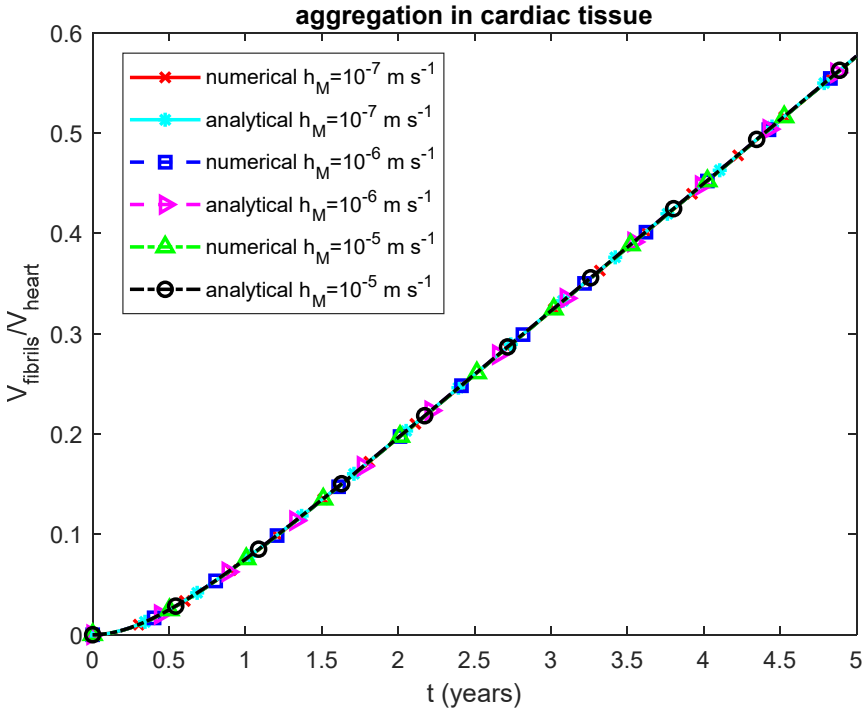

Fig. S14. Fraction of heart volume occupied by TTR amyloid fibrils vs time. (a) Scenario when TTR monomers misfold and assemble into protofibrillar formations within the bloodstream before depositing in the heart for various values of $\theta_{1/2,I}$. (b) Scenario when TTR monomers remain in circulation until they directly attach to sites within the heart, where they form amyloid deposits *in situ* for various values of h_M.

(a)

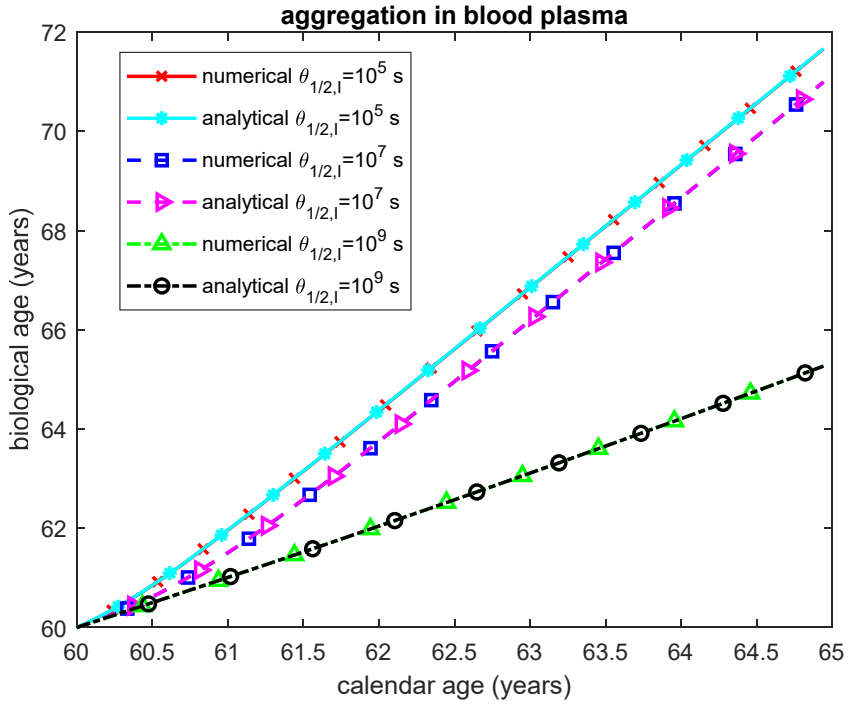

(b)

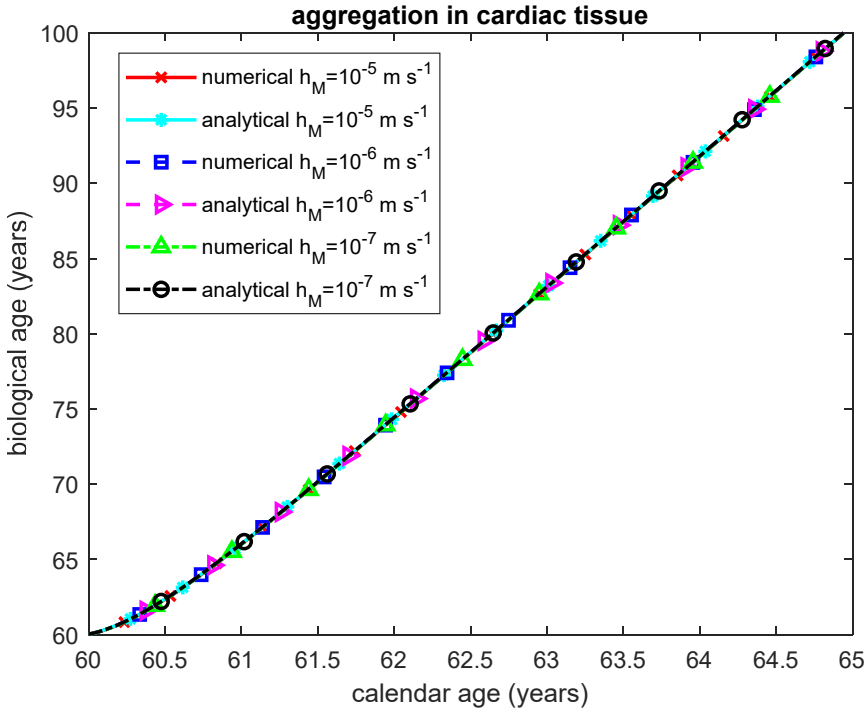

Fig. S15. Biological age vs calendar age. (a) Scenario when TTR monomers misfold and assemble into protofibrillar formations within the bloodstream before depositing in the heart for various values of $\theta_{1/2,I}$.

(b) Scenario when TTR monomers remain in circulation until they directly attach to sites within the heart, where they form amyloid deposits *in situ* for various values of h_M.

(a)

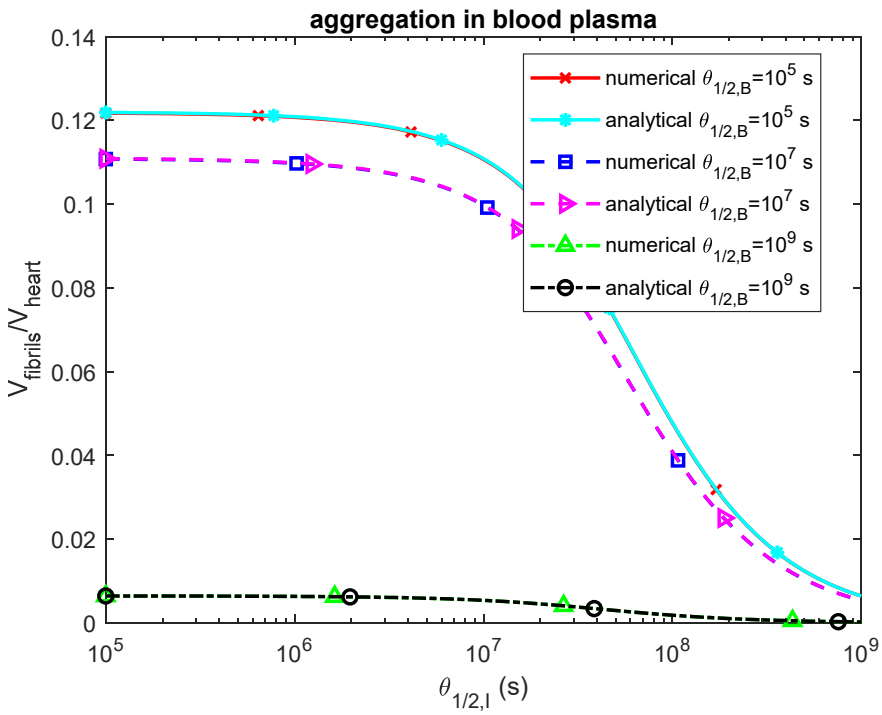

(b)

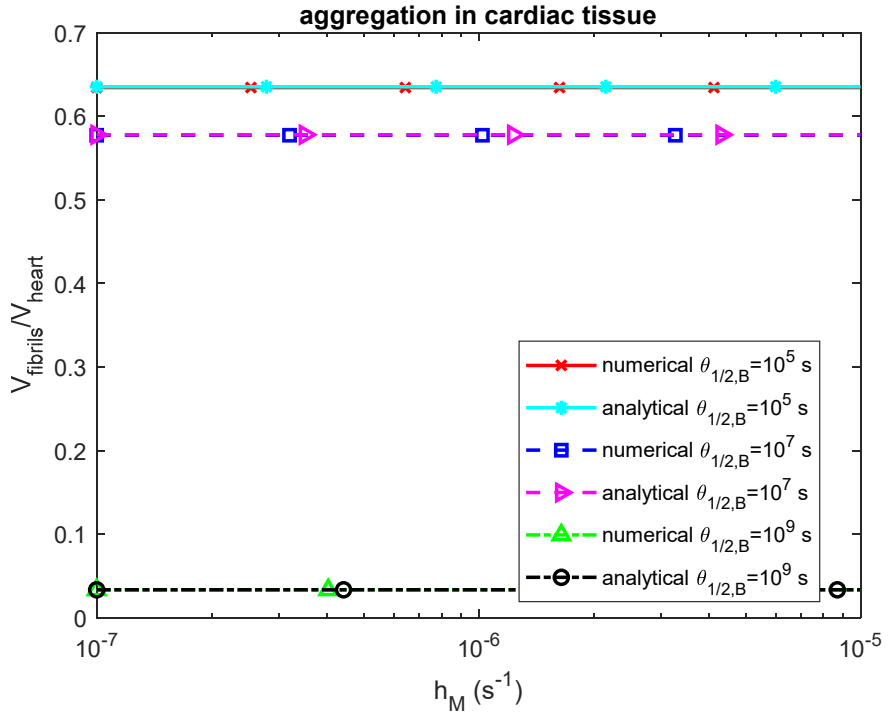

Fig. S16. Fraction of heart volume occupied by TTR amyloid fibrils. (a) As a function of the half-deposition time for TTR-derived fibrils circulating in the blood plasma to deposit into cardiac tissue. This corresponds to the scenario in which TTR monomers misfold and assemble into protofibrils within the bloodstream before depositing in the heart, shown for various values of $\theta_{1/2,B}$. (b) As a function of the mass transfer coefficient characterizing the rate at which circulating TTR monomers deposit into the endocardium. This represents the scenario in which TTR monomers remain in circulation until they bind directly to cardiac sites and form amyloid deposits *in situ*, shown for various values of $\theta_{1/2,B}$.

(a)

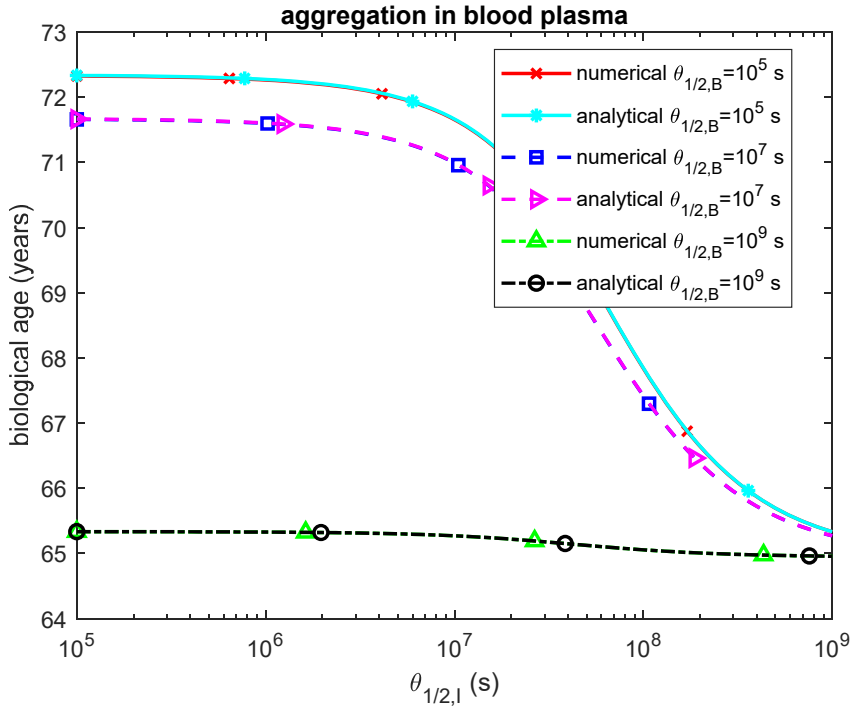

(b)

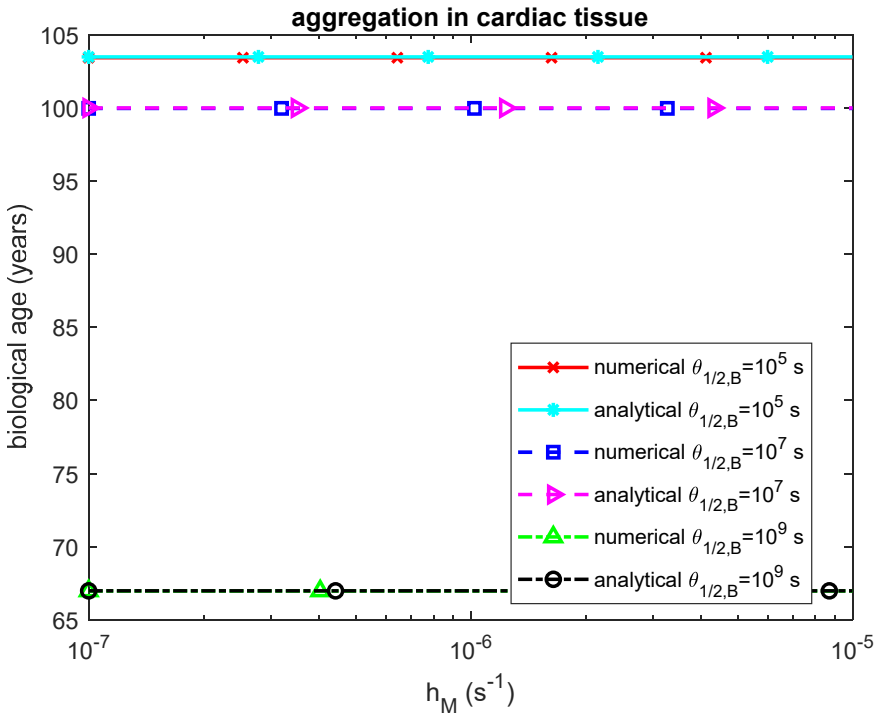

Fig. S17. Biological age. (a) As a function of the half-deposition time for TTR-derived fibrils circulating in the blood plasma to deposit into cardiac tissue. This corresponds to the scenario in which TTR monomers misfold and assemble into protofibrils within the bloodstream before depositing in the heart,

shown for various values of $\theta_{1/2,B}$. (b) As a function of the mass transfer coefficient characterizing the rate at which circulating TTR monomers deposit into the endocardium. This represents the scenario in which TTR monomers remain in circulation until they bind directly to cardiac sites and form amyloid deposits *in situ*, shown for various values of $\theta_{1/2,B}$.

(a)

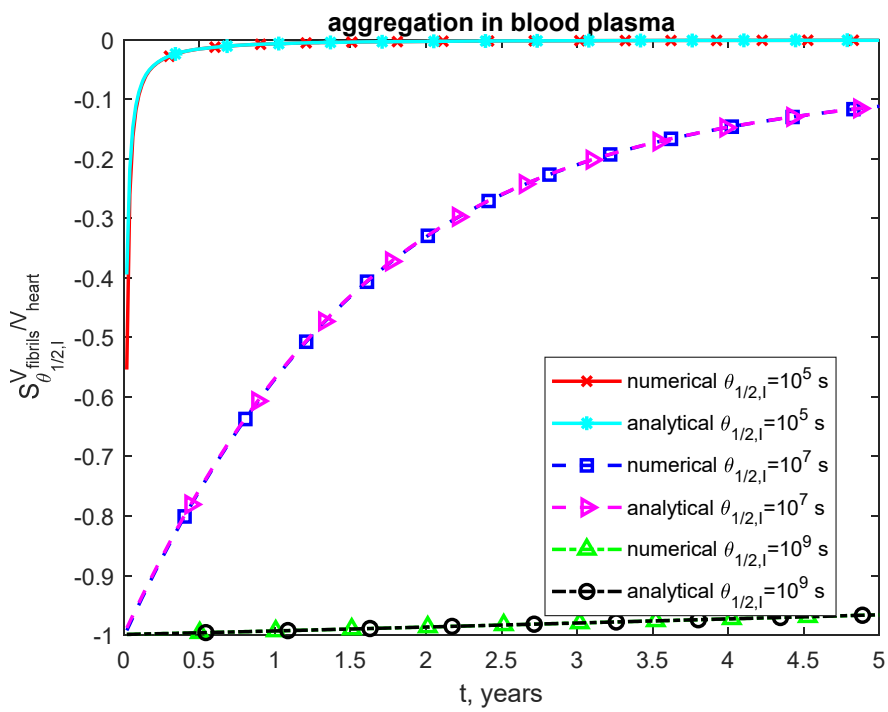

(b)

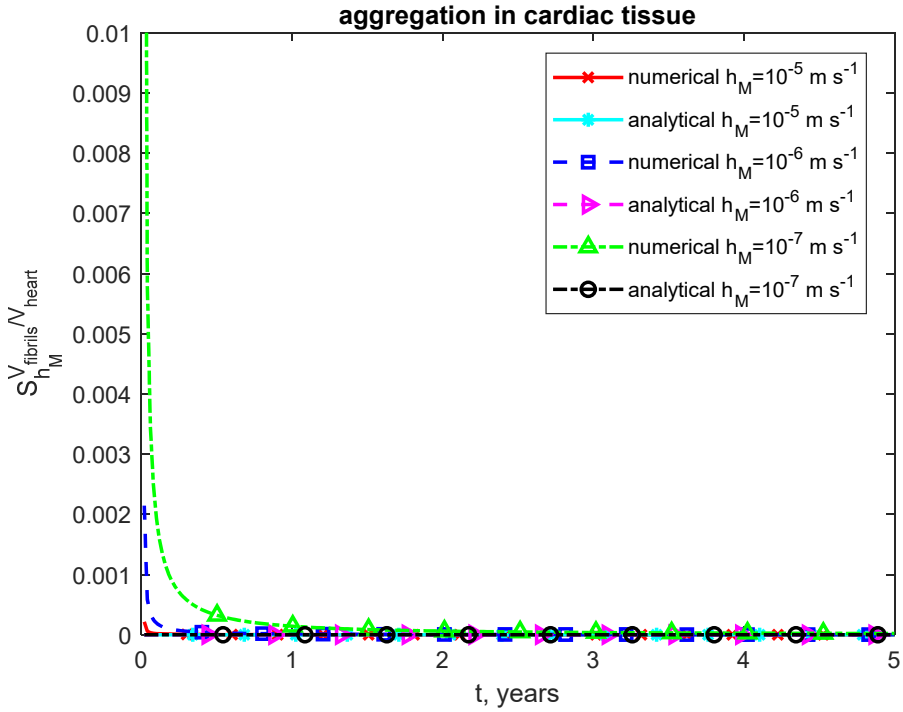

Fig. S18. (a) Dimensionless sensitivity of the fraction of heart volume occupied by TTR amyloid fibrils to the half-deposition time for TTR-derived fibrils circulating in the blood plasma to deposit into cardiac tissue, $\theta_{1/2,I}$, shown as a function of time. This corresponds to the scenario in which TTR monomers misfold and assemble into protofibrillar structures within the bloodstream before depositing in the heart. (b) Dimensionless sensitivity of the fraction of heart volume occupied by TTR amyloid fibrils to the mass transfer coefficient characterizing the rate of deposition of TTR monomers into endocardium, h_M, also shown as a function of time. This corresponds to the scenario in which TTR monomers remain in circulation until they directly bind to sites within the heart, forming amyloid deposits *in situ*.